UNIVERSITY OF CALIFORNIA
RIVERSIDE

Looking Backward and Forward – Comprehensive Investigation of Particle Dynamics Within Multiple Generations of UCR/CE-CERT Environmental Chambers

A Dissertation submitted in partial satisfaction
of the requirements for the degree of

Doctor of Philosophy

in

Chemical and Environmental Engineering

by

Chen Le

March 2023

Dissertation Committee:
Dr. David R. Cocker III, Chairperson
Dr. Donald R. Collins
Dr. Roya Bahreini

The Dissertation of Chen Le is approved:

_____

_____

_____

Committee Chairperson

University of California, Riverside

Acknowledgements

I would like to express my gratitude to everyone who has supported me throughout my PhD journey, which started in the fall of 2016. I am deeply thankful to my family – my parents and grandparents, for their unconditional love and support throughout my life. They have sacrificed a lot to educate me and guide me to become the person I am today, and I am forever grateful for everything they have done for me. I would also like to thank my classmates and friends from around the world for their emotional support and the fun times we have shared.

I am grateful for my decision to pursue environmental engineering as my undergraduate major, which led me to CE-CERT at UCR for my PhD studies. During my time at HUST, China, Professor Jiakuan Yang and Academician Jiming Hao had a significant impact on my decision to focus on air quality studies. Although these experiences were not directly related to my PhD career, they ignited my passion for teaching and inspired me to be responsible for my learning and development.

I owe a debt of gratitude to my advisor, Dr. David Cocker, for his exceptional mentorship and friendship. His ENVE133 class initially sparked my interest in air quality studies, and he provided me with the self-motivating opportunity to fulfill my dream at CE-CERT. Dr. Cocker is a patient, experienced, and dedicated mentor who always puts his students' personal development and success first. I am fortunate to have had the opportunity to learn from him, both academically and personally, and I will always cherish the memories we shared together.

I would like to thank my dissertation committee, Dr. Don Collins and Dr. Roya Bahreini, for their invaluable help and guidance on my projects. They provided me with insightful feedback and suggestions that greatly contributed to my dissertation. I am also grateful to Professor Kelley Barsanti, Haofei Zhang, Ying-Hsuan Lin, Wayne Miller, Cesunica Ivey, David Jassby, Juchen Guo, and Yanran Li, for their support, insights, and/or collaboration throughout my PhD studies.

I would also like to acknowledge the impact that the COVID-19 pandemic had on my PhD journey. When I was stuck in China due to lockdown, I was forced to reflect on the purpose of my life. I am grateful that I made it through the toughest time with my dearest grandparents. Although I struggled to be productive during that time, it helped me refocus and prioritize my academic work upon my return to the United States. I am grateful for the opportunity to have gone through this experience, as it has helped me grow both personally and academically.

Finally, huge shout-outs to Xinyu Zhang, my beloved girlfriend, with my cute cats, Melon and Pear, for their accompany and love; huge shout-outs to my current and former colleagues: Mary, Sara, Paul, Patrick, Xinze, Weihan, Ayla, Yuehua, Jinwei, Qi, Sahar, Tom, Ryan, Danny, Huawei, Yanyu, Kyah, Hanwei, Tianbo, Jerry, Ningjin, Zihan, etc., as well as my former undergrad volunteers: Kharla, Jose, Christian, Josiah, Amy, Nathan and more. I am lucky to have all of them around and I have learnt a lot from every single one of them; huge shout-outs to Carolyn Ray and Valerie Thomas from CE-CERT, Adrienne Thomas, Kate Seo and Crystal Schenkel from the department, and Kelly Eldridge Hinosawa and Heidi Nam from International Student Affairs office, for all the help on my paperwork, preparations and plannings; huge shout-outs to all my funding supports, including Esther F. Hays scholarship, National Science Foundation, Directorate for Geosciences, Division of Atmospheric and Geospace Sciences, Atmospheric Chemistry Program and the California Air Resources Board. Without these supports I couldn't have made progresses on all the things I am passionate about and enjoy exploring.

To conclude, I am deeply grateful for being fortunate enough to have had all these fantastic relationships, exciting encounters, and precious memories. I sincerely appreciate whatever has made my experiences unique and has helped me be myself. I am proud to have graduated from the APL group, CE-CERT, UCR.

ABSTRACT OF THE DISSERTATION

Looking Backward and Forward – Comprehensive Investigation of Particle Dynamics Within Multiple Generations of UCR/CE-CERT Environmental Chambers

by

Chen Le

Doctor of Philosophy, Graduate Program in Chemical and Environmental Engineering
University of California, Riverside, March 2023
Dr. David R. Cocker III, Chairperson

Indoor environmental chambers have been widely used to simulate the Secondary Organic Aerosol (SOA) generation processes in the atmosphere. Experimental data is used to optimize atmospheric models, contribute to scientific predictions, and policy making. However, the measured data, such as the quantified aerosol yield, can be biased due to the interactions between the gas-particle system and chamber walls. Minimizing uncertainties of particle- and vapor-wall deposition corrections thus become critical. This dissertation crystalizes the journey to review and explore the particle-wall interactions and to make responsible corrections in multi-generations of environmental chambers at UCR.

Size-dependency of particle wall-loss varies between Teflon environmental chamber designs. The measured particle wall-loss rates in UCR previous-generation dual 90-m^3 collapsible chambers were relatively insensitive to particle size with the rates exceeding those reported for some smaller volume chambers. Coagulation-free monodisperse seed injection experiments were performed and the particle wall-loss behaviors were experimentally observed to be dominated by

electrostatic effect via charged chamber walls. Particles in the chamber were found to approach chamber-specific charge steady-state, driven by size-dependent preferential loss of charged particles and bidirectional diffusion charging.

The traditional particle wall-loss correction model has been modified into a new system to investigate the significance of particle-particle coagulation and dynamic change of particle wall-loss rates within experiments for previous-generation collapsible chambers. The modified model re-visited particle wall-loss corrections for thousands of historical runs over the past two decades, creating a massive data pool with increased correction accuracy. Dynamic change of particle wall-loss rate was observed within individual experiments. Final particle mass can be over-corrected due to coagulation, dependent on the particle number loadings present in the chamber.

Mitigation strategies to minimize the electrostatic impact have been applied on UCR new-generation 120-m^3 fixed-volume chamber. Size-dependent particle wall-loss patterns were characterized with monodisperse seed injection experiments with negligible coagulation. The observed trend was found to be more sensitive to particle size and much lower than previous-generation chambers. A three-component particle loss correction model has been developed to account for chamber dilution, particle coagulation and wall-loss. Performance evaluation shows good agreement between the new correction method with the modified traditional method.

Table of Contents

List of Figures

List of Tables

Chapter 1: Introduction

Air pollution is one of the major global environmental problems that deeply affects human health and well-being around the world (Pickering and Owen 1997). Air pollution can be caused by a variety of human activities and/or natural events, including fossil fuel burning, industrial processes, biogenic emissions, volcano eruption, etc. It can have a wide range of negative impacts on the ecosystem as well as human health, including but not limited to the respiratory system, the cardiovascular system, and the brain (Bakolis et al. 2021; Brunekreef and Holgate 2002). Air pollution was estimated to have caused 6.7 million premature deaths annually by the World Health Organization (WHO 2022). The United States Environmental Protection Agency (USEPA) lists six criteria air pollutants: carbon monoxide, ground-level ozone, lead, nitrogen dioxide, sulfur dioxide and particulate matter.

Particulate matter, also known as PM or aerosol, refers to a liquid/solid suspension in the atmosphere varying in size and composition. Aerosol can be formed from both biogenic and anthropogenic sources. Organic aerosol (OA) accounts for up to 90% of the submicron particle burden globally (Jimenez et al. 2009; Zhang et al. 2007). Under this category, secondary organic aerosol (SOA), forms via atmospheric oxidation of volatile organic or intermediate volatile compounds (VOCs or IVOCs) followed by gas-particle partitioning. SOA contributes to the majority of OA mass (Hallquist et al. 2009). SOA is typically small enough to be inhaled deep into human lungs causing adverse health impacts (De Gouw and Jimenez 2009) and can potentially impact climate forcing by influencing cloud formation (Haywood and Boucher 2000).

Laboratory simulations, field measurements and modeling works have been widely conducted to understand the atmospheric processes that potentially form SOA. Experiments in laboratory environmental chambers simulate the SOA generation processes in a controlled environment in absence of atmospheric transport processes (e.g., Carter et al. 2005; Cocker et al. 2001). One of the critical missions of conducting SOA chamber experiments is to quantify the SOA yield, a measure of the SOA generation potential from a target precursor under controlled atmospheric conditions. The SOA yield is widely used in gas-particle partitioning models and is calculated as the ratio of ΔM_o, the SOA mass concentration formed in a chamber experiment, to ΔHC, the hydrocarbon mass concentration consumed (Donahue et al. 2006; Odum et al. 1996, 1997). Accurate quantification of the ΔM_o values from measured properties in a chamber experiment is challenged by the fact that the generated particles can deposit on wall surfaces of the environmental chamber where the deposited portion cannot be measured. Therefore, significant error in estimating particle mass formation occurs when one does not account properly for the cumulative loss of generated particles, leading to biased modeling predictions using chamber-based SOA yield. Particle wall deposition (particle wall-loss) theories have been described in a wide variety of studies (Charan et al. 2018; Cocker et al. 2001; McMurry and Rader 1985; Crump and Seinfeld 1981). However, particle wall-loss patterns vary among different chamber facilities due to their unique chamber designs and experimental conditions. Therefore, each chamber facility must perform case-specific characterizations and develop their own methodologies to correct for the particle wall-loss (e.g., Nah et al. 2017).

This thesis expands the understanding of particle wall-loss behaviors within multiple generations of environmental chambers in UCR/CE-CERT and summarizes the efforts of particle wall-loss correction optimizations and chamber design evolution. Chapter 2 discusses the current interpretation of particle wall-loss behaviors in the previous-generation UCR/CE-CERT dual 90-

m^3 collapsible chambers, a design used to study SOA formation for almost two decades. The observations suggest that the particle wall-loss behavior in this chamber was dominated by the electrostatic effect, which enhanced the particle wall-loss rates as a function of particle size and experimental time. The observations also suggest the impact of particle-particle coagulation on the traditional particle wall-loss correction method that we used. Chapter 3 presents the development of a model applying modified particle wall-loss correction methods based on Chapter 2 observations for UCR/CE-CERT dual 90-m^3 collapsible chambers, as well as the model application for a retrospective on thousands of the experiments historically conducted in this facility over the past two decades. Coagulation and dynamic change of particle wall-loss rates within the experiment were tracked and accounted for, which improved the accuracy of the calculated particle volume/mass. The model provides a platform to efficiently assess experimental repeatability over the last two decades as well as to re-evaluate large historical experimental sets. Chapter 4 focuses on the efforts to minimize the actual chamber electrostatic charge effect and further mitigate impacts of particle wall-loss. This led to the design and construction of the next-generation 120-m^3 fixed-volume environmental chamber. Size-dependent particle wall-loss pattern for this new chamber was derived from a series of monodisperse, coagulation-free characterization experiments. The pattern was then applied to develop a verified new particle wall-loss correction model where the correction of particle wall-loss can be evaluated without empirically fitting wall loss from the individual experiment and is also independent from the coagulation calculation of the individual experiment.

Manuscripts presented in this dissertation:

The contents of Chapter 2 are ready to submit with Aerosol Science and Technology:

- Le C., Xu N., Li Q., Collins D. R. and Cocker D. R.: Experimental Characterization of Particle Wall-loss Behaviors in UCR Dual-90m^3 Teflon Chambers (Ready to submit, expected to be published in 2023)

The contents of Chapter 3 and Chapter 4 will be converted into two separate papers, respectively:

- Le C. and Cocker D. R.: A Retrospective of Re-modelled Particle Wall-loss Correction for Historical Experiments in UCR 90-m^3 Collapsible Chambers (in preparation, expected to be published in 2023)
- Le C., Eckel T., Xu N., Li Q., Collins D. R. and Cocker D. R.: Next-generation UCR 120-m^3 Fixed-volume Chamber – Experimental Characterization of Particle Wall-loss Using Monodisperse Seed Injections (in preparation, expected to be published in 2023)

Other publications/manuscripts not presented in this dissertation:

I participated heavily in the ICARUS project: Index of Chamber Atmospheric Research in the United States, representing UCR as the data manager in curating environmental chamber dataset standards and contributing to the database. This led to a co-author paper:

- Nguyen T. B., Bates K. H., Buenconsejo R., Charan S., Cavanna E. E., Cocker D. R., Day D., DeVault M., Donahue N. H., Finewax Z., Habib L., Handschy A., Hildebrandt Ruiz L., Hou C., Jimenez J., Joo T., Klodt A., Kong W., Le C., Masoud G. G., Mayernik M., Ng N. L., Nienhouse E., Nizkorodov S. A., Orlando J. J., Post J. J., Sturm, O., Thrasher B., Tyndall G. S., Seinfeld J. H., Worley S., Zhang X. and Ziemann P.: Overview of ICARUS – A Curated, Open Access, Online Repository for Atmospheric Simulation Chamber Data (In review process with ACS Earth and Space Chemistry, expected to be published in 2023)

I led a project collaborating with Dr. Haofei Zhang and Dr. Ying-Hsuan Lin's research groups studying SOA formation and evolution from *a*-pinene dark ozonolysis in absence of OH radicals under temperature and humidity cycles. This led to the co-author paper:

- Zhao Z., Le C., Xu Q., Peng W., Jiang H., Lin Y., Cocker D. R. and Zhang H., Compositional Evolution of Secondary Organic Aerosol as Temperature and Relative Humidity Cycle in Atmospherically Relevant Ranges, ACS Earth Space Chem, 2019

I significantly contributed to the project studying SOA formation from *m*-xylene oxidation at very low NOx conditions, leading to a co-author paper:

- Peng W., Le C., Porter W. C. and Cocker D. R., Variability in Aromatic Aerosol Yields under Very Low NO_x Conditions at Different HO_2/RO_2 Regimes, Environ., Sci. Technol., 2022

I contributed to the study of SOA formation from *a*-pinene oxidation under various branching ratios using continuous NO_x injection method by providing interpretations on particle wall-loss correction with the new environmental chamber, leading to a co-author paper:

- Ghadimi S., Li H., Le C., Porter W. C. and Cocker D. R., Influence of Continuous NOx Injection on SOA Yield from Biogenic Precursors: A Comprehensive Branching Ratio Study (in preparation, expected to be published in 2023)

I participated in the study of SOA formation through aqueous-phase reactions of water insoluble VOCs processed using a newly-developed oxidation flow reactor by managing the experimental coordination and contributing to mass spectrometer data, leading to co-author papers:

- Xu N., Le C., Cocker D. R., and Collins D. R., An Oxidation Flow Reactor for Simulating and Accelerating Secondary Aerosol Formation in Aerosol Liquid Water and Cloud Droplets, Atmos. Meas. Tech., 2022
- Insights Into Secondary Organic Aerosol Formed via Aqueous-phase Reactions of

Water Insoluble VOCs (in preparation, expected to be published in 2023)

I led an interdisciplinary application project numerically exploring significant environmental parameters for *m*-xylene SOA formation in UCR chambers using machine learning, which will lead to a co-author paper:

- Zhang Y., Wallis J., Le C. and Cocker D. R., Numerically Exploring Significant Experimental Parameters for Secondary Organic Aerosol from *m*-Xylene Oxidation in UCR Chambers Using Machine Learning (in preparation, expected to be published in 2024)

Chapter 2: Experimental Characterization of Particle Wall-loss Behaviors in UCR Dual-90m^3 Teflon Chambers

2.1 Introduction

Chamber/flow tube simulations, field measurements and modeling works provide different but unique perspectives to understand the atmospheric processes during which secondary organic aerosol (SOA) can be generated. Experiments in environmental chambers simulate the SOA generation processes in a controlled environment in absence of atmospheric transport processes (e.g., Carter et al. 2005; Cocker et al. 2001). One goal of environmental chamber studies is to quantify the SOA generation potential from target precursor(s) given a limited but specific set of atmospheric conditions. Environmental chambers have surfaces that can interact directly with particulate matter produced within them. However, the atmosphere does not have the same boundaries that environmental chambers do. Once generated particles are lost to the chamber wall during the course of an experiment, they can no longer be detected and particle wall-loss correction must be accounted for to accurately report aerosol yield. It is still under discussion whether or not particles on the wall are able to continue growing during experiments (Trump et al. 2016; Hildebrandt et al. 2009), but even with simple assumptions of no growth after deposition, particle wall-loss leads to significant underestimation on measured aerosol yields unless accounted for appropriately. Thus, understanding particle wall-loss

mechanisms and conducting reasonable correction are critical to minimize these uncertainties (McMurry and Grosjean 1985).

Previous studies have concluded that convection, Brownian diffusion, gravitational sedimentation and electrostatic effect are the major driving forces of the particle wall-loss processes. Their theoretical estimation and early chamber verifications have shown that convection is a function of chamber design; Brownian diffusion can be significant on sub-100 nm particle sizes; gravitational sedimentation can be significant on > 500 nm particles and the electrostatic charges on chamber surfaces and particles have case-specific enhancements on all particle sizes (Van Dingenen et al. 1989; McMurry and Rader 1985; Crump et al. 1982; Crump and Seinfeld 1981). The total measurable number particle loss (referred to in this work as measured number particle loss) is the sum of particle wall-loss and particle coagulation (loss of number but not suspended mass), which simultaneously occurs during chamber experiments (Cocker et al. 2001). Similar to the theoretical estimation, many laboratory studies have recently reported chamber-specific size-dependent particle wall-loss patterns with or without theory-based evaluations on coagulation, noting that the scale of the decay rate difference between two measurable sizes could reach one order of magnitude or more (Shao et al. 2022; Vansevenant et al. 2021; Charan et al. 2018; Sunol et al. 2018; Wang et al. 2018; Nah et al. 2017; Leskinen et al. 2015; Loza et al. 2012; Pierce et al. 2008).

The concept of the electrostatic effect on particle wall-loss processes was first reported in 1980s and has recently regained attention due to the development of modeling and detection techniques (Charan et al. 2018, 2019; Pierce et al. 2008; Van Dingenen et al. 1989; McMurry and Rader 1985; Crump and Seinfeld 1981). When particles are charged, their wall-loss rates become higher, but the enhancement is still a function of particle size (Charan et al. 2019; McMurry and Rader 1985; Saucy et al. 1983). Exposure of suspended particles to a charged medium (such as

suspended ions charged by cosmic radiation) is inevitable. When particles and the charged medium collide, charge transfer may occur (Mahfouz and Donahue 2020; Wagner et al. 2017; Kirkby et al. 2016; Franchin et al. 2015). Theoretical calculation has indicated that larger particles have much higher charging probabilities than do smaller particles assuming that particles are spherical and under a constant ion field, but the actual charge rate is still affected by the particle concentration (Marlow and Brock 1975). The particle-charge interaction asymmetry between positive- and negative-polarity due to their different mobilities has been reported for different types of particles (Simones et al. 2011; Hoppel and Frick 1986; Marlow and Brock 1975), but such asymmetry was neglected in particle wall-loss charge study for simplicity (McMurry and Rader 1985).

Recent discussions have shown that the electrostatic effect could be either significant or negligible depending on the specific situation of each chamber. The reported averaged particle decay rate in UCR 90-m^3 collapsible chambers, 7 day^{-1} (Carter et al. 2005), exceeded the reported values from other smaller chambers, e.g., Caltech 28-m^3 dual chambers in early 2000s, 2~4 day^{-1} (Cocker et al. 2001); Caltech new 19-m^3 chamber, 0.5~2 day^{-1} (Charan et al. 2018). This suggests that particle wall-loss behaviors in UCR collapsible chambers were somehow enhanced by charged chamber walls. On the other hand, it was reported that such an effect could be ignored in the new 19-m^3 Caltech chamber under an uninterrupted condition (Charan et al. 2018). In situations where the electrostatic played a role, the significance of its effect was found to fluctuate as the experiment proceeded since the particle charge distribution in the chamber also evolved with experimental time. Although charge-shifted particle wall-loss curves were theoretically calculated and experimentally evaluated in previous works (Mahfouz and Donahue 2020; Wang et al. 2018; Pierce et al. 2008; McMurry and Rader 1985), a direct observation of how decay of charged particles behave among the total particles was still needed to further understand the

particle size dependence of electrostatics effect on a charged chamber and to constrain the uncertainties for future particle wall-loss corrections. Overall, the wall-loss behaviors are not only affected by the charge distribution tendencies of particles themselves, but also by such tendencies from the air surrounding the particles and the chamber walls (McMurry and Rader 1985; Cooper et al. 1979).

It has been generally acknowledged that other than electrostatic charge, factors such as chamber geometry, turbulence, reaction speed and other potential ones can also affect particle loss behaviors in each chamber, thus case-specific particle loss characterizations must be developed for each environmental chamber (Wang et al. 2018; Nah et al. 2017; Pierce et al. 2008). It has been reported that the particle-wall deposition rates in Caltech chamber did not vary significantly as a function of chamber volume change during experiments (Loza et al. 2012) and such rates were not affected by humidity when the electrostatic effect was insignificant (Charan et al. 2018). Particle coagulation, which could deeply affect the wall-loss correction based on particle number concentration (Cocker et al. 2001), especially for the small particle size range (<150 nm), has been recently simulated using a dynamic model, which accounted for coagulation as a function of experimental time (Nah et al. 2017). The calculation of particle coagulation in chamber experiments have also been discussed (Charan et al. 2019; Pierce et al. 2008). At the same time, more characterization is needed as a function of temperature, chamber relative volume (the chamber surface-area-to-volume ratio, A/V) and other potential candidates, in order to provide a more comprehensive understanding regarding the particle wall-loss.

In this study, a monodisperse particle injection approach was used to characterize the size-dependent particle wall-loss patterns under the electrostatic effect in the absence of coagulation within the UCR dual 90-m^3 collapsible chambers. Such experimental methods provided controlled size of particles while limiting the particle number concentration under 500

cm^{-3}, which was sufficiently low to be assumed "coagulation-free" for the measurement time-scale. Particle wall loss experiments with different coagulation intensities using higher number concentration polydisperse particle number loadings were also conducted. The current experimental dataset follows the same trend shown for coagulation effects observed by Nah et al. (2017) and Wang et al. (2018). Additionally, the unique design of a modified dual-SMPS system helped characterize the fate and transport of the charged particles within our chamber.

2.2 Experimental

2.2.1 Environmental chambers

The previous-generation dual 90-m^3 collapsible chambers at CE-CERT, UC Riverside were characterized in this study. Their collapsible design and the other characteristics have been discussed elsewhere (Carter et al. 2005). Experiments (Table 2-1) were conducted at room temperature (~ 21°C) and ultra-low relative humidity (< 0.1%) unless otherwise specified. Ammonium Sulfate (Sigma-Aldrich, 99%) was nebulized to generate mono- and poly-dispersed seed particles.

Table 2-1. List of experiments used in this study.

Run Number	Time (min)	Particle Composition	Particle Size	Specific Notes
2429A	339	Ammonium Sulfate	Polydisperse	Varied initial particle number loadings
2429B	339	Ammonium Sulfate	Polydisperse	
2430A	300	Ammonium Sulfate	Polydisperse	
2430B	300	Ammonium Sulfate	Polydisperse	
2431A	405	Ammonium Sulfate	Polydisperse	
2432A	493	Ammonium Sulfate	Polydisperse	
2479B	480	Ammonium Sulfate	50 & 200 nm	
2482B	360	Ammonium Sulfate	50 & 300 nm	
2483B	360	Ammonium Sulfate	50 & 400 nm	
2487B	427	Ammonium Sulfate	50 & 200 nm	
2489B	360	Ammonium Sulfate	50 nm	
2492B	385	Ammonium Sulfate	100 nm	
2497B	544	Ammonium Sulfate	50 & 200 nm	Positively charged particles only, dual-SMPS system
2498B	586	Ammonium Sulfate	50 & 200 nm	Dual-SMPS system
2530B	575	Ammonium Sulfate	50 & 200 nm	Negatively charged particles only, dual-SMPS system
2532B	554	Ammonium Sulfate	50 & 200 nm	Neutral particles only, dual-SMPS system
Mez091020	415	Ammonium Sulfate	Polydisperse	Varied initial particle number loadings
Mez091220	459	Ammonium Sulfate	Polydisperse	
Mez091420	486	Ammonium Sulfate	Polydisperse	
Mez091620	362	Ammonium Sulfate	Polydisperse	

2.2.2 Experimental design

2.2.2.1 Particle atomization and polydisperse particle wall-loss experiments

Dry ammonium sulfate seed aerosol was generated from a 0.1 M solution using a constant-rate atomizer (Liu and Lee, 1975), followed by a heating tunnel, a drying column and a ^{210}Po neutralizer (10.0 mCi). For polydisperse particle wall-loss experiments, atomized ammonium sulfate particles were then injected directly into the chambers. Particles after going through the ^{210}Po neutralizer were assumed to be at Fuchs' charge equilibrium regardless of their charge status prior to the entrance of the neutralizer. Previous studies have shown that pre-existing charges from particle generation processes do not affect their final charge distribution after going through the neutralizer, thus the output particle charge distribution was reasonably assumed to be at equilibrium (He and Dhaniyala 2014; Biskos et al. 2005; Adachi et al. 1985).

2.2.2.2 Monodisperse experiments

A portable high-flow differential mobility analyzer (DMA) system, described by Xu and Collins (2021), was used to classify nebulized ammonium sulfate polydisperse particles (Section 2.2.2.1) prior to injection into the environmental chambers. The dry ammonium sulfate particles were neutralized by a soft x-ray neutralizer before entering the high-flow DMA column. The monodisperse particles were classified and further dried through a Nafion tubing (Perma Pure). The sheath flow rate was set to 36 Lpm. Since the DMA column only transmits a very narrow particle size range, most of the particles produced from the atomizer were removed resulting in low number concentration of the monodisperse particles (up to 500 cm^{-3}) suspended in the

chamber. The effect of coagulation on particle decay in monodisperse experiments is assumed to be negligible at these low number concentrations.

Different experimental settings (Figure 2-1) were applied in order to inject particles under different charging status: a) positively charged particles were injected to the chamber by applying a negative high-voltage (HV) (CPS 2591N-24V-10KV REV-A) to the high-flow DMA column; b) negatively charged particles were injected to the chamber by applying a positive HV supply (BERTAN 602C-150P) to the high-flow DMA column; c) neutralized particles were generated by applying a secondary ^{210}Po neutralizer before the particles were injected to the chamber; d) neutral particles were selected by applying a custom electrostatic precipitator (5000V) right after the secondary neutralizer.

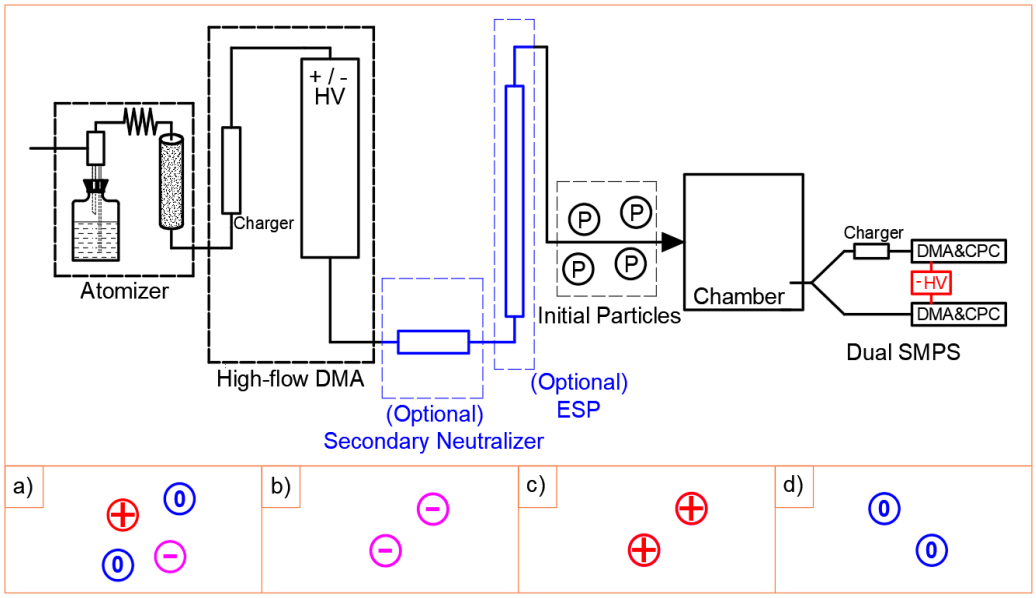

Figure 2-1. Schematic diagrams of the experimental set-up options. Initial particles could be prepared as: **a)** at charge equilibrium (neutralized), **b)** all negatively charged, **c)** all positively charged, **d)** no particle charges (neutral).

2.2.3 Particle measurement and SMPS data collection

Similar set-up studying ambient particle charge distribution (Buckley et al. 2008) has been applied in UCR collapsible chambers. Particle samples were collected from the environmental chambers with a dual-SMPS system. Both of the DMA columns are equipped with a negative HV supply (BERTAN 602C-100N) and therefore only select positively charged particles. One of the SMPS was set up conventionally, equipped with an ^{85}Kr neutralizer before the entrance of the DMA column (referred to in this work as SMPS with charger) so that particle charge equilibrium was achieved prior to entering the DMA column. Therefore, the SMPS with charger measured total particle concentrations after applying the standard SMPS inversion algorithm (Collins et al. 2002). The other SMPS (referred to in this work as SMPS without charger) had no neutralizer equipped; particle samples entered the DMA column with the same charge distribution as present in the chamber. Therefore, the SMPS without charger only detected the positively-charged particles from the environmental chamber.

The data acquired from the SMPS without charger needs correction when quantitative comparison is needed. The built-in signal-to-data inversion program of such SMPS treats the incoming signal assuming that the particles were at Fuchs' particle charge equilibrium regardless of the actual (non-equilibrium) fraction of positively-charged particles present. It is assumed in this work that the sample particle stream reaches the Fuchs' particle charging equilibrium with Wiedensohler approximation after passing through the ^{85}Kr neutralizer and before entering the DMA column for the SMPS with charger system (Wiedensohler 1988; Fuchs 1963). Table 2-2 shows the simplified Fuchs' particle charging distribution for two particle sizes of interest. Regardless of the complicated inversion calculations during the SMPS signal-to-data processes, the "+1-to-total" ratio that the calculation applied over a specific size is constant. For the scope of

this study, those ratios were directly applied as a simple but sufficient correction to the data output of the SMPS without charger when a rough number concentration of positively-charged particles is needed.

Table 2-2. Single-size particle charge distribution at Fuchs' charge equilibrium.

Diameter	-3	-2	-1	0	+1	+2	+3
50 nm	--	0.89%	22.29%	59.05%	17.25%	0.52%	--
200 nm	3.54%	12.53%	25.37%	29.36%	19.42%	7.35%	1.59%

2.3 Result and Discussion

2.3.1 Experimental indication of electrostatic effect in UCR collapsible chambers

Measurements of particle wall-loss behaviors of select particle sizes (50, 100, 200, 300 and 400 nm electrical mobility diameter) were obtained from monodisperse particle experiments. As mentioned in Section 2.2.2.2, wall-loss rates are not impacted by particle coagulation for these experiments (referred to in this work as coagulation-free wall-loss). The general trend of coagulation-free particle wall-loss rates for select particle sizes is shown (Figure 2-2). Each dot (Figure 2-2a) represents the average decay rate for the select particle size during the course of an experiment. Variation in particle decay rate for similar sized particles was small between repeat experiments conducted on different days. Crump and Seinfeld (1981) explored the basic size-dependent particle wall-loss patterns in chambers assumed to be affected by only Brownian motion and gravitational settling and observed that the decay rate decreases with particle size until the size reaches 300~400 nm at which point the decay increases as particle size further

increases. McMurry and Rader (1985) subsequently suggested that the observed trend would be altered with increased electrostatic effect. The current size-dependent coagulation-free wall-loss rates observed (Figure 2-2a), when compared to the previous cited work, suggest that electrostatic effects may be much more important than Brownian motion and Gravitational forces within our environmental chamber. Additionally, it was observed that size dependent particle wall loss rates in the UCR collapsible chamber follows a similar trend to the particle size dependent total Fuchs' charging probability (Figure 2-2b). Both observations suggest that the electrostatic effect in the UCR collapsible chamber might overpower the other two main driving forces for particle wall deposition. However, since the decay rates at different sizes only varied by two-fold (3~6 day^{-1}), further experimental work was performed to elucidate the extent of electrostatic effect on particle wall loss in the UCR collapsible chamber.

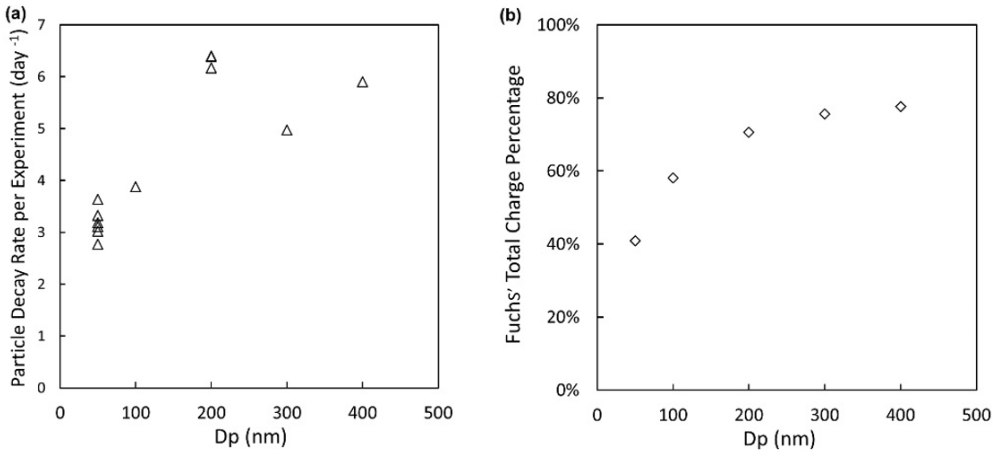

Figure 2-2. (a) Averaged monodisperse particle wall-loss rates as a function of particle size in UCR collapsible chambers and **(b)** Fuchs' total charge percentage as a function of particle size.

Particle wall-loss behavior in the UCR collapsible chamber was further observed directly using our dual-SMPS measurement technique. The dual-SMPS set-up (Figure 2-3) was applied to a bimodal particle wall-loss experiment where low concentrations (up to 500 cm^{-3}) of two narrowly selected sizes (50 and 200 nm) of particles co-existed. The blue curves represent normalized total number concentrations versus time while the red curves represent normalized only positively charged particles present in the chamber. Enhanced electrostatic particle wall-loss was directly observed as the positively charged 50 nm and 200 nm particles decayed faster than total particles. Further, even though a larger decay rate due to Brownian motion is expected for 50 nm particles than 200 nm particles, the observed total number decay rate of the 200 nm particles exceeds that of the 50 nm particles. This suggests a higher enhancement of the decay rate of 200 nm particles than 50 nm particles due to electrostatic effects. The decay rate difference between charged and total particles is more significant for 50 nm particles than for 200 nm particles due to the higher electrical mobility of the former; however, total 200 nm particles still have the higher decay rate than total 50 nm particles (Figure 2-3, blue curves) due to the kinetic charging limitation for 50 nm particles. The fraction of charged particles seemed to approach to a steady-state between being replenished and being preferentially lost to the wall later in the experiment, thus it is probably the limited replenishing rate of charged 50 nm particles that constrains their overall decay enhancement by the electrostatic effect (also see Section 2.3.2).

The significance of the electrostatic effect on total particle decay rate was further illustrated by corresponding the charged particle decay behavior with the total particle decay behavior as a function of time (Figure 2-3c). Wall-loss experimental time was divided into four quartiles with first-order decay rates calculated for each time period. The decay rates for 50 nm particles during the first quartile of the experiments clearly exceeded the decay rates during the later quartiles, consistent with the preferential loss of charged particles in early periods.

Additionally, although the observation that the particle wall-loss rate decreases with time is in agreement with the prediction of McMurry and Rader (1985) under electrostatic-driven conditions, it is also noted that the decay rates increase during the fourth periods from our observation. We attribute this increase to changes in surface-area-to-volume ratio during collapse of the chamber, which is an additional effect unique to the UCR large collapsible chambers.

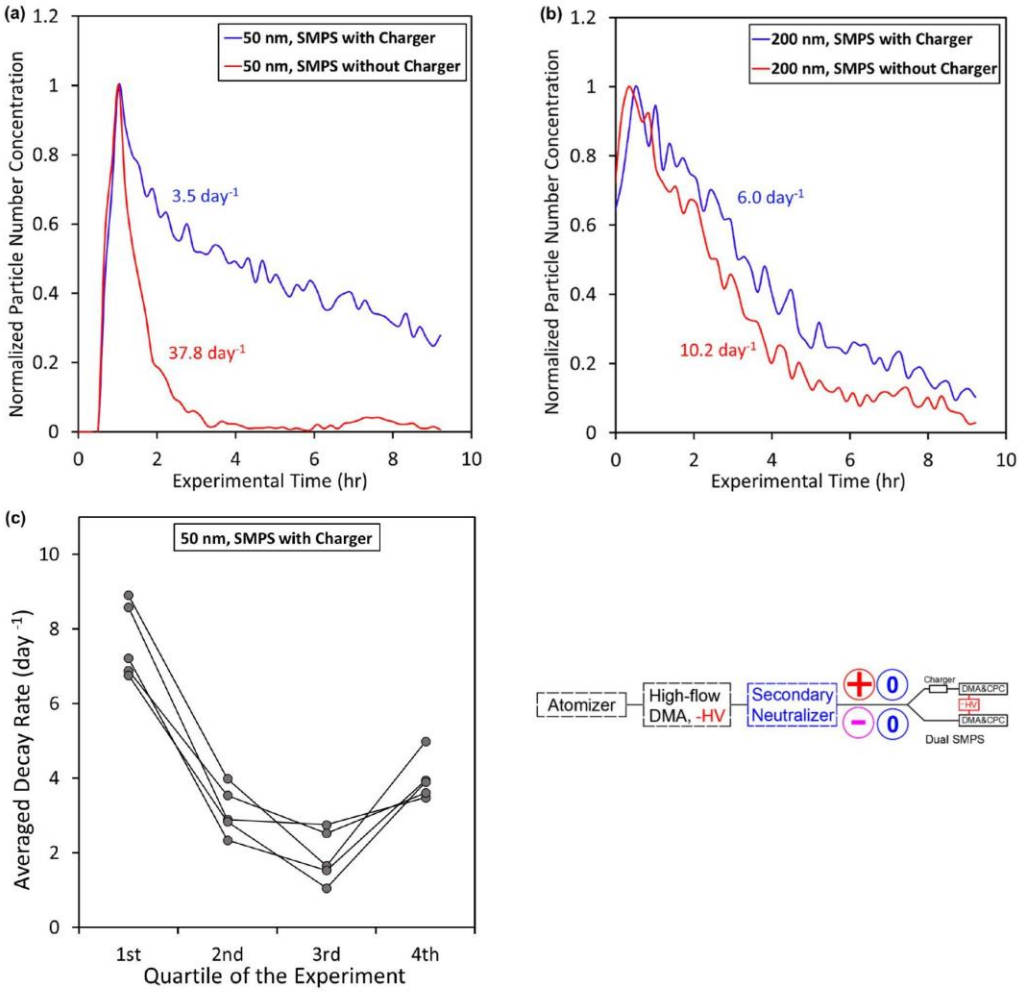

Figure 2-3. Dual-SMPS measurements on monodisperse particle wall-loss at two typical sizes, **(a)** 50 nm and **(b)** 200 nm during a characterization experiment. The blue curves represent normalized total particle number concentrations, measured by SMPS with charger; The red curves represent normalized positively-charged particle number concentrations, measured by SMPS without charger; **(c)** 50 nm total particle decay rates in four quartiles from the five selected characterization experiments.

2.3.2 Direct measurement of dis-/re-charging behaviors

Mahfouz and Donahue (2020) demonstrated that particles within a chamber during an experiment are dynamically reaching a chamber-specific charge steady-state, driven by both preferential loss of charged particles and bidirectional diffusion charging. It is also experimentally observed in this work by another three particle loss experiments where 50 nm and 200 nm size selected particles were introduced into the chamber as either all positively charged, all negatively charged, or all neutral particles. Since particles are selected based on their electrical mobility, 50 nm selected particles may include multiple charged larger diameter particles with a mobility equivalent to a single charged 50 nm particle. Therefore, for this section, the use of the term "50 nm particles" refers to the amount of single charged 50 nm particles plus a lesser number of larger multiple charged particles that were injected with equivalent mobility to the 50 nm single charged particle (same for the term "200 nm particles"). Particles from the three experiments were observed to undergo bidirectional diffusion charging along with different observed wall loss behaviors using the dual SMPS (Figure 2-4). The SMPS without charger (red/pink curves) only detects positively charged particles that were suspended in the chamber while measurements using the SMPS with charger (blue/teal curves) include particles that were positively, negatively, or neutrally charged when suspended in the chamber. Therefore, the difference between the blue/teal curve and the red/pink curve at any given time represents the sum of neutral and negatively charged particles suspended in the environmental chamber.

Neutral particle injection experiment: The observed data from the neutral particle injection experiment (Figure 2-4-a1 and Figure 2-4-a2) indicates particle diffusion charging process, possibly driven by the collision of initially neutral particles with surrounding charged gases induced by cosmic radiation (Wagner et al. 2017; Kirkby et al. 2016; Franchin et al. 2015).

Originally neutral particles became charged and the positively charged particles were then detected (SMPS without charger, red/pink curve). Positively charged 50 nm particles are barely present (red curve, Figure 2-4-a1), caused by both the much-faster decay rate of presented charged particles and their lower theoretical charging probabilities (Marlow and Brock 1975).

Positive particle injection experiment: The particle discharge behavior was directly observed (Figure 2-4-b1 and Figure 2-4-b2) in addition to the preferential loss of charged particles, because particles other than positively charged were detected (indicated by the difference between blue/teal curve and red/pink curve), while all the injected particles were initially positively charged. This is possibly driven by the collision of initially-charged particles with surrounding neutral or oppositely-charged gases. The observed discharge rate of initially positively charged 200 nm particles is much faster than the discharge rate of initially positively charged 50 nm particles as the pink curve (200 nm particles, Figure 2-4-b2) diverges from the teal curve even before the completion of particle injection into the chamber, while the red curve (50 nm particles, Figure 2-4-b1) remains entangled with the blue curve for about 1 hour after the injection.

Negative particle injection experiment: Similar discharge behavior was observed when only negatively charged particles were injected (Figure 2-4-c1 and Figure 2-4-c2). The measurement result suggests that a portion of initially negatively charged particles were dis-charged to neutral and then re-charged to positive as the SMPS without the charger can only detect particles that were positively charged in the chamber. The measurement of a greater fraction of 200 nm positively charged particles (Figure 2-4-c2) than for 50 nm particles (Figure 2-4-c1) is consistent with smaller 50 nm initially negatively charged particles both decaying to the walls faster and charge equilibrating slower than the 200 nm initially negatively charged particles.

Coupled with observations from Section 2.3.1, the particle wall loss trend in Figure 2-3-c is reasonably explained: in early periods of the experiments, the total particle wall-loss rates are driven by the preferential loss of initially charged particles. Next, in the later time periods, the total decay rates are kinetically limited by the rate of particle charging. Finally, the uptick in wall loss is due to the collapsing of volume of the UCR system increasing surface area to volume ratio.

To summarize: 1) the electrostatic effect dominates losses of particles due to Brownian motion (even at the smallest measured sizes) in the UCR collapsible chamber; 2) 50 nm charged particles decay much faster than 200 nm charged particles; 3) the overall decay enhancement by the electrostatic effect on 50 nm particles is smaller than on 200 nm particles, due to the kinetic particle charging limitation at the former size; and 4) particles in the chamber tend toward chamber-specific charge steady-state by preferential loss of charged particles and bidirectional diffusion charging, where the former dominates the smaller (50 nm) particles and the latter dominates larger (200 nm) particles.

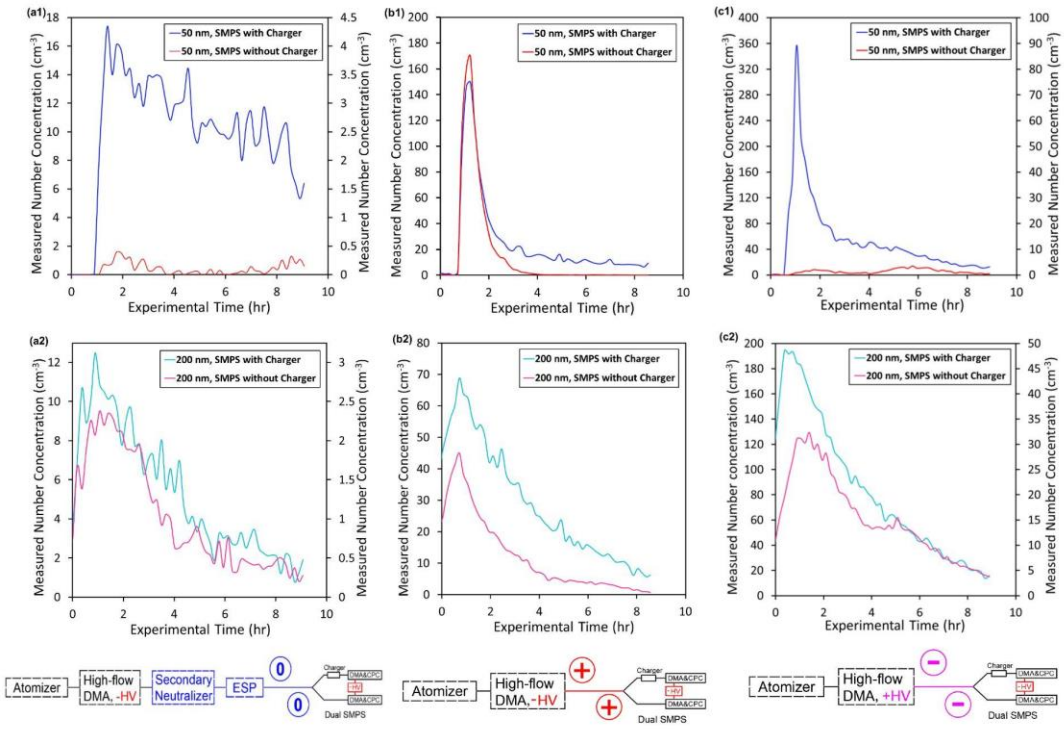

Figure 2-4. Dual-SMPS measurements on monodisperse particle wall-loss at two typical mobility sizes, 50 and 200 nm, during three typical types of characterization experiments. **(a)** Neutral-only, **(b)** positively-charged only and **(c)** negatively charged only particles were injected to the chamber, respectively. The blue/teal curves were measured by SMPS with charger while the red/pink curves were measured by SMPS without charger, detecting only the positively charged particles suspended in the chamber. The red/pink curves in **(a1)**, **(a2)**, **(c1)** and **(c2)** are scaled up by 4 times and referred to the secondary y-axis.

2.3.3 Coagulation effect

Nah et al. (2017) provided model simulations of experiments with particle coagulation processes leading to particle number loss, thus here we introduce the term "measured particle loss" as the combination of particle wall-loss and coagulation loss. Their simulations show that smaller particles collide to form larger particles during coagulation resulting in particle losses of smaller particles that are somewhat compensated by the formation of larger particles. The effect of coagulation on experimentally determined size dependent particle wall-loss is observed (Figure 2-5) when polydisperse aerosol is injected into the chamber. A clear increase in measured size dependent particle wall-loss for higher concentration polydisperse aerosol injection experiments versus much lower concentration monodisperse particles is observed for diameters less than 200 nm due to coagulation loss of the smallest diameter particles in our dual 90-m^3 chambers. An additional series of increasing number concentration polydisperse particle wall-loss experiments were conducted in the UCR 37.5-m^3 MEZ chamber (Figure 2-6), where the chamber setup has been described in detail in (Nakao et al. 2011). As expected, the measured size-dependent particle decay rates for particles under 200 nm increased with particle number concentration. As coagulation rate increased with particle number loading, the measured particle loss rates for smaller particles increased while the measured particle loss rates lowered for larger particles. The intensity of coagulation could be sufficient to overpower the wall deposition of the larger particles, suggested by the negative measured particle loss rates for diameters greater than ~ 320 nm (solid blue curve, Figure 2-6). In short, coagulation in polydisperse seed wall-loss experiments, especially at higher concentrations, can significantly impact the measured particle loss rates, thus the low-loading monodisperse characterization experiments are recommended to reduce coagulation impacts. Alternatively, computational corrections accounting for coagulation

are encouraged when conducting particle loss corrections in environmental chambers using polydisperse aerosols (Charan et al. 2019; Sunol et al. 2018; Wang et al. 2018; Nah et al. 2017).

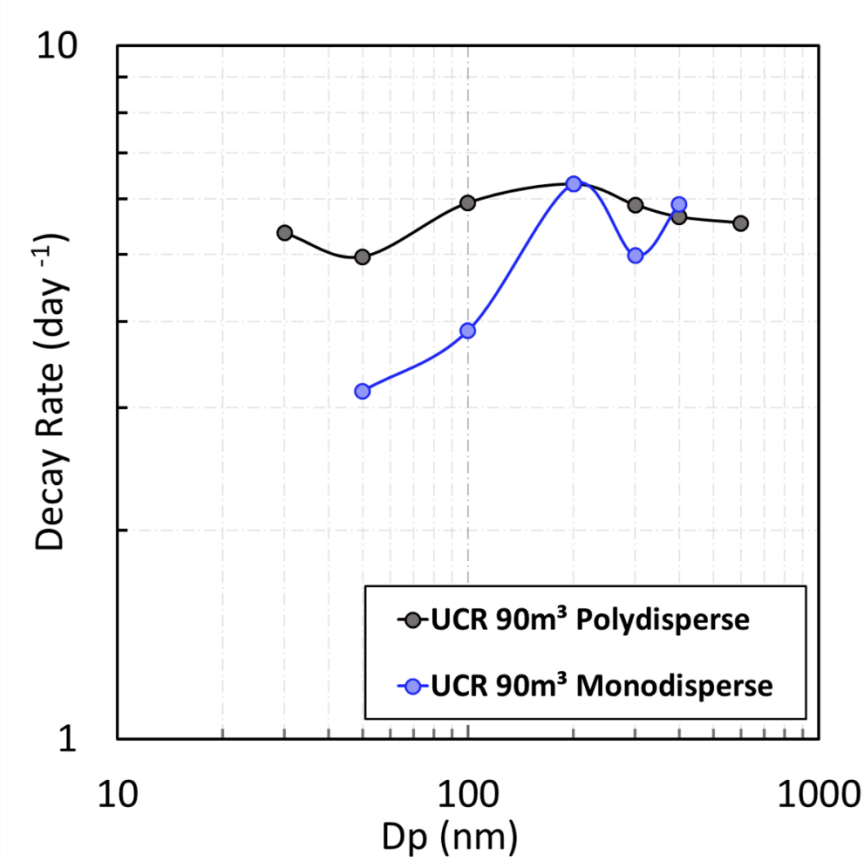

Figure 2-5. Comparison of the averaged size-dependent measured particle loss pattern obtained from polydisperse experiments (black curve) and the averaged size-dependent coagulation-free particle wall-loss pattern obtained from monodisperse experiments (blue curve) in UCR 90-m³ collapsible chambers.

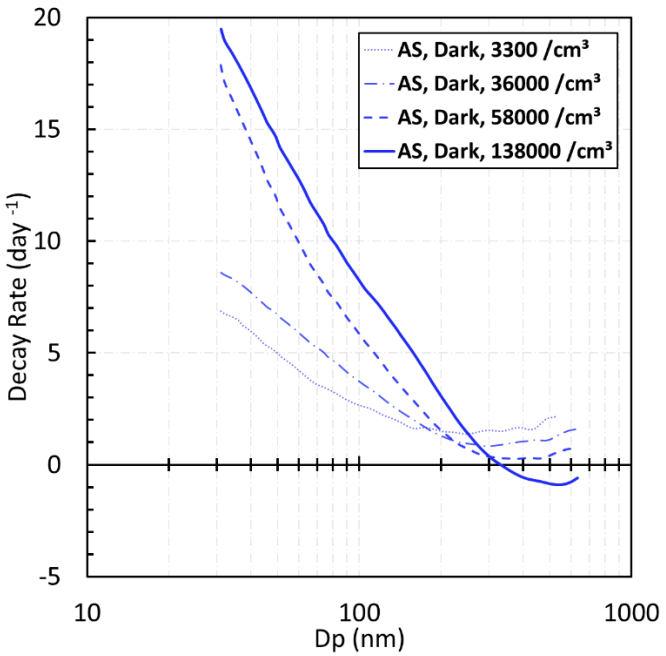

Figure 2-6. Averaged size-dependent measured particle loss patterns from experiments designed with increased particle number loadings (in units of cm^{-3}) in UCR 37.5-m^3 chamber.

2.3.4 Inter-comparison within the chamber community and implication

An inter-comparison of size-dependent particle wall-loss patterns was performed using both recent literatures and/or personal communications (Figure 2-7). The size-dependent particle wall-loss rates are distributed across two orders of magnitude between different environmental chambers, implying that particle wall-loss patterns vary widely between chamber designs. These variations include differences in design/environment parameters such as physical shape, surface area/volume ratio (in static or dynamic), surface charging sources, etc., as well as their own operational schemes such as convection conditions, RH surrounding the chamber, electrostatic disruption during chamber operation (e.g., walking near chamber), rubbing between multiple

reactors and/or between the surface of the reactor and its enclosure, etc. The effect of different chamber sizes was previously claimed to be insignificant (McMurry and Rader 1985) since their curves originated from a 250-Liter Teflon chamber and were then validated by their 60-m^3 chamber. However, understanding that particle wall-loss pattern is affected by a combination of factors, sometimes a single factor is less significant for one experimental chamber but not in another. McMurry and Rader (1985) also determined that the size-dependent wall-loss rate should intuitively look like a "spoon" (the solid red curve, Figure 2-7) if not affected by electrostatics, and this rule can be applied to roughly estimate the importance of electrostatic particle loss in a chamber, thus providing guidance for future chamber design modifications. Most of the size dependent wall-loss curves from other chamber facilities listed in Figure 2-7 have the "spoon" indicator, suggesting that electrostatics are not dominating their particle wall losses. Charan et al. (2018) specifically concluded that the electrostatic effect in the Caltech new 19-m^3 chamber could be neglected. Curves for UCR collapsible chambers seem to be remarkably elevated from a "spoon" baseline, indicating the existence of electrostatic loss in the UCR collapsible 90-m^3 chambers despite its large size. The UCR collapsible chambers have the following designs that may enhance the role of electrostatic wall-loss: 1) the chamber enclosure air surrounding the chambers was constantly purged and extremely dry (RH<0.1%), 2) the chamber was collapsible leading to rubbing of the wall material; 3) the chamber walls were constantly rubbing against each other in the dual-chamber design due to the external mixing system (air handlers) during experiments, and 4) the chamber walls were in direct contact with the reflective (and conductive) aluminum enclosure that it resides in. The UCR 37.5-m^3 MEZ chamber is a single chamber, with little contact with grounded conducting surfaces and without dry-air external purge – observations for particle size-dependent wall-loss in the MEZ chamber are consistent with the "spoon" rule, suggesting that the electrostatic loss is not the preferential route in this chamber.

The measured particle loss pattern and the coagulation-free particle wall-loss pattern collected in this work have furthered our understanding of the particle decay behavior affected by electrostatics and coagulation in UCR dual collapsible chambers. It is noted that the measured particle loss rates in UCR collapsible chambers are not as sensitive to particle size as other chambers, consistent with the size independent wall-loss correction method that has been used for this chamber (Nah et al. 2017; Carter et al. 2005). Additionally, it is noted that the measured particle loss rates in UCR collapsible chambers can change during and between experiments, due to the unique particle coagulation and charging dynamics as a function of experimental conditions. Regardless, based on measurements in this work (Section 2.3.3) and modeling works from recent studies, coagulation still needs to be corrected when larger particle numbers are present, by either experimental or computational approaches. To further constrain such uncertainties and increase the particle wall-loss correction accuracy, a coagulation-corrected, time-resolved particle wall-loss correction method is warranted for chambers susceptible to surface charging and for collapsible chambers. It is further noted that Caltech's chamber reduces its potential electrostatics effect by not contacting conducting surfaces and during experimental operation by restricting access to the chamber enclosure (Charan et al. 2018). Similar and other mitigation strategies are needed in UCR collapsible chambers to lower the particle wall-loss due to electrostatics. A new-generation fixed-volume 120-m^3 chamber has been installed in UCR in replace of the dual collapsible chambers with regards to such mitigation, and the details and characterizations of particle wall-loss will be discussed in future works.

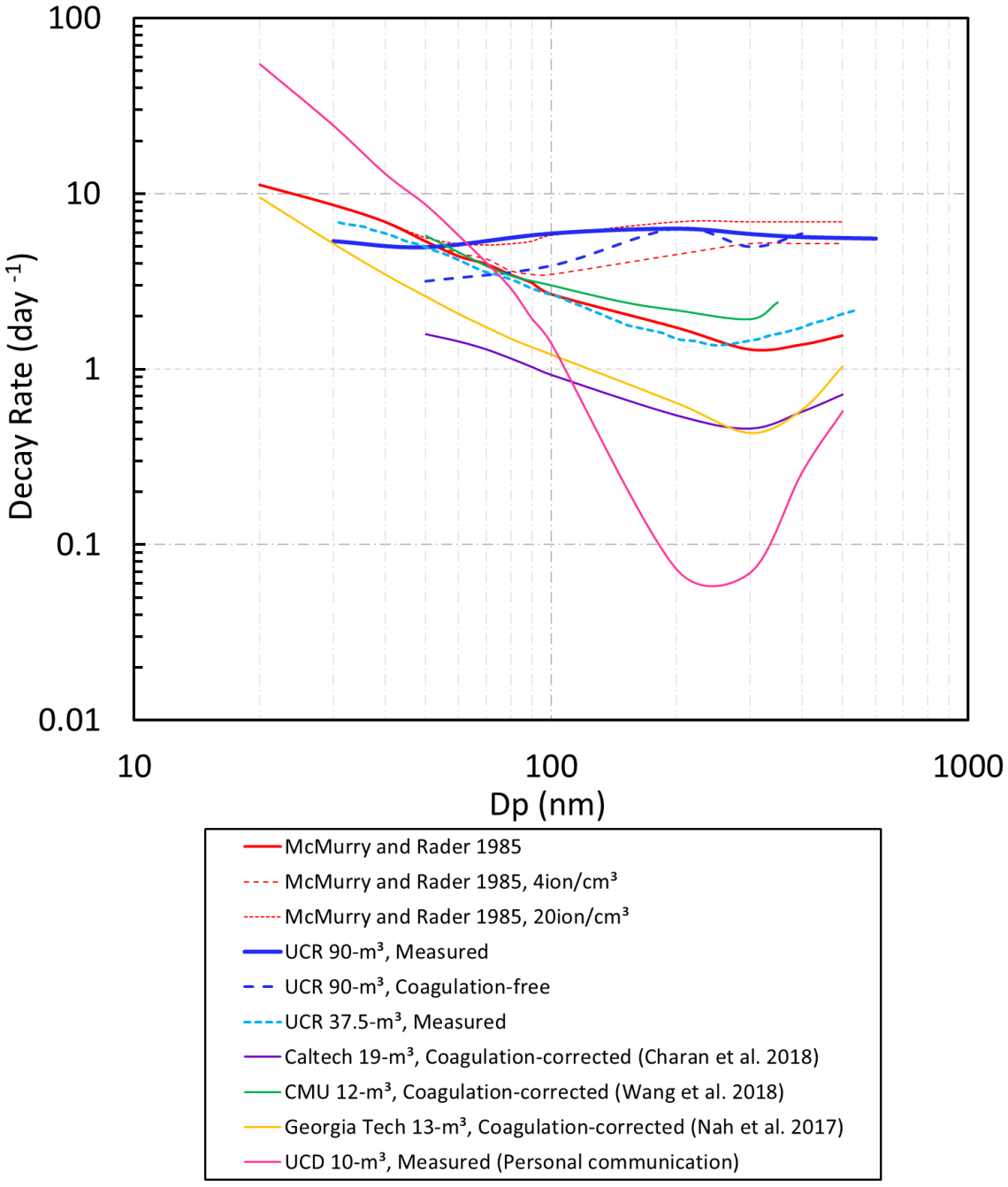

Figure 2-7. Inter-comparison of averaged size-dependent particle number loss patterns among different chamber facilities or calculations. "Measured" represents measured particle loss (including particle wall-loss and coagulation); "Coagulation-corrected" represents particle wall-loss rates computationally-corrected for coagulation and "Coagulation-free" represents particle wall-loss rates obtained from monodisperse particle injection experiments.

2.4 Conclusions

A monodisperse particle injection and a dual-SMPS measurement approach were used to characterize the size-dependent particle wall-loss patterns under the electrostatic effect in the absence of coagulation within the UCR dual 90-m^3 collapsible chambers. The collected data shows that the enhancement of particle wall-loss rate by electrostatic effect is the dominant loss mechanism and that larger particles (in a typical chamber experiment) are more influenced, resulting in particle decay rates in UCR collapsible chambers relatively insensitive to particle size. Smaller charged particles were found to have higher decay rates, but also have more significant kinetic charging limitations than larger charged particles. Particles in the chamber, regardless of initial charge distribution, tend to approach a specific charge steady-state during the course of an experiment. Smaller particles approach the charge steady-state via preferential loss of charged particles, while larger particles are driven by bidirectional diffusion charging rates. By inter-comparing the particle number loss patterns within the chamber community, we conclude here that the "spoon-shaped" size-dependent particle loss patterns can be used to roughly identify the significance of the electrostatic effect, and that such patterns are dependent on the chamber geometric designs and operating maneuver. Mitigation strategies are warranted for a chamber susceptible to surface charging in order to lower down the uncertainty in particle wall-loss correction and improve the accuracy of measured SOA yields. Additionally, the coagulation effect was observed to be significant enough to impact particle wall-loss in experiments that have increased particle number loadings, especially for < 200 nm particles. Therefore, efforts to account for coagulation loss is recommended, either by computationally/theoretically calculating or experimentally minimizing the coagulation.

Chapter 3: Retrospective Analysis of Two Decades of Particle Wall-loss Correction from the UCR Dual 90-m^3 Collapsible Chamber Using a New Dynamic Size-independent Coagulation-corrected Method

3.1 Introduction

Environmental chambers have been widely used to simulate the formation of atmospheric secondary organic aerosol (SOA) from the oxidation of volatile organic compounds (Hallquist et al. 2009; Odum et al. 1997). SOA yield (Y), defined as the ratio of the generated SOA mass concentration to the mass concentration of the consumed precursor hydrocarbons, are derived from chamber experiments as a measure of the SOA generation potential from the target precursor (Odum et al. 1996, 1997). Particles generated within the chamber can deposit onto chamber walls where they cannot be detected. Cumulative particle loss to the chamber walls must be accounted for to reasonably estimate the total generated particle mass. Therefore, minimizing uncertainty associated with particle wall-loss corrections are critical for accurately quantifying aerosol yield from environmental chambers.

Particle-wall deposition rate in an environmental chamber is proportional to particle concentration and is a function of particle size, which is represented by first-order particle kinetics:

$$\left(\frac{dN(Dp,t)}{dt}\right)_{particle\ wall-loss} = -\beta(Dp)N(Dp,t) \quad \text{(Equation 3-1)}$$

where Dp is the diameter of the particle, $\beta(Dp)$ is the chamber-specific particle wall-loss coefficient as a function of particle size, and $N(Dp,t)$ is the particle number distribution as a function of particle size and time (Cocker et al. 2001; Bowman et al. 1997). $N(Dp,t)$ is constrained by the SMPS measurements at each scan time. It was discussed previously (Chapter 2) that particle wall-loss behaviors in the UCR collapsible chambers are enhanced by the charged surfaces of chamber walls (Le et al. 2023; Carter et al. 2005). As the result, the measured electrostatic-enhanced particle wall-loss rates in UCR collapsible chambers vary day-to-day and are relatively insensitive to particle size (Figure 2-6; Carter et al. 2005, Figure 5) leading to Equation 3-1 reducing to Equation 3-2:

$$\left(\frac{dN(t)}{dt}\right)_{particle\ wall-loss} = -\beta N(t) \quad \text{(Equation 3-2)}$$

where β is the wall-loss rate of total particles and $N(t)$ is the total number concentration as a function of time. Typically, the experiment-specific, size-independent β value is derived by fitting the SMPS-measured total particle number decay during the final three hours of the experiment. This first-order decay rate is then applied to the SMPS-measured particle number and volume concentrations (Equations 3-3 and 3-4) to correct for particle wall-loss:

$$\Delta N_i = \frac{N_{(i-1)} + N_i}{2}\left(1 - exp\left(-\beta\left(t_i - t_{(i-1)}\right)\right)\right), i \geq 2 \quad \text{(Equation 3-3)}$$

$$\Delta V_i = \frac{V_{(i-1)} + V_i}{2}\left(1 - exp\left(-\beta\left(t_i - t_{(i-1)}\right)\right)\right), i \geq 2 \quad \text{(Equation 3-4)}$$

where ΔN_i is particle wall-loss corrected total number concentration at step i, ΔV_i is particle wall-loss corrected total volume concentration at step i, N is measured number and V is measured volume. The derivation of β is based on measured particle number decay; therefore, particle number loss due to particle-particle coagulation will bias β, especially for increased particle number loadings in the chamber (Le et al. 2023; Nah et al. 2017). Further, it was observed (Chapter 2) for the UCR collapsible chamber experiments that: 1) particles in the chamber approach a charge steady-state, which leads to dynamic changes of particle charge distribution as well as dynamic changes of the electrostatic enhancement on particle-wall deposition; and 2) the reduced volume of the collapsed chambers in later periods of experiments increases the surface-area-to-volume ratio. These observations suggest that real-time particle wall-loss rates do not remain constant during a chamber experiment and therefore use of single β value may not accurately describe particle wall-loss over the duration of an experiment. Thus, a coagulation-corrected, time-resolved particle wall-loss correction method is needed to improve wall-loss correction estimates.

A particle coagulation dynamics model is developed in this study to update the particle wall-loss correction for experiments using the UCR collapsible chambers. The model is designed to calculate dynamic particle wall-loss rates after accounting for coagulation. The model was packaged into a MATLAB program to efficiently calculate the particle wall-loss corrections of over 1900 experimental datasets from UCR collapsible chamber experiments conducted during the past two decades.

3.2 The Particle Coagulation Dynamics Model

Table 3-1 summarizes different particle wall-loss correction methods that are included in the program, where the method named “Single Beta-Fit” (“SB-Fit”) refers to the traditional size-

independent number-averaged particle wall-loss correction, which assumes that the total particle number decay is size-independent and attributed to wall-loss only. The "Coagulation-corrected Dynamic Beta-Fit" ("CcDB-Fit") method assumes that both particle wall-loss and particle coagulation occur simultaneously, thus dynamic coagulation-corrected particle total number decay rates are calculated. Ten adjacent SMPS scans are used to reduce measurement noise and to fit the total number decay rate for each time step. The "Dynamic Beta-Fit" ("DB-Fit") is the intermediate method, where dynamic deposition rates are calculated but no correction is made for coagulation.

Table 3-1. Summary of different particle wall-loss correction methods evaluated in the model.

Method Name	Calculation Source	Time-resolved	Coagulation-corrected
Single Beta-Fit (SB-Fit)	Total number decay during the whole fitting time	No	No
Dynamic Beta-Fit (DB-Fit)	Local total number decay	Yes	No
Coagulation-corrected Dynamic Beta-Fit (CcDB-Fit)	Local total number decay	Yes	Yes

The overall logic diagram of the model is also visualized (Figure 3-1), where Num refers to the particle number concentration, Vol refers to the particle volume concentration, SizeD refers to particle size distribution, PWL refers to particle wall-loss and PeakDp refers to the peak particle diameter. The model evaluates either a single experiment with more user options or a batch of experiments with less user options. The model outputs include wall-loss corrected particle number (NUMCOR) and volume (VOLCOR) using the three previously-mentioned different particle wall-loss correction methods. The relationship between model outputs and different particle wall-loss correction methods are illustrated in Figure 3-2.

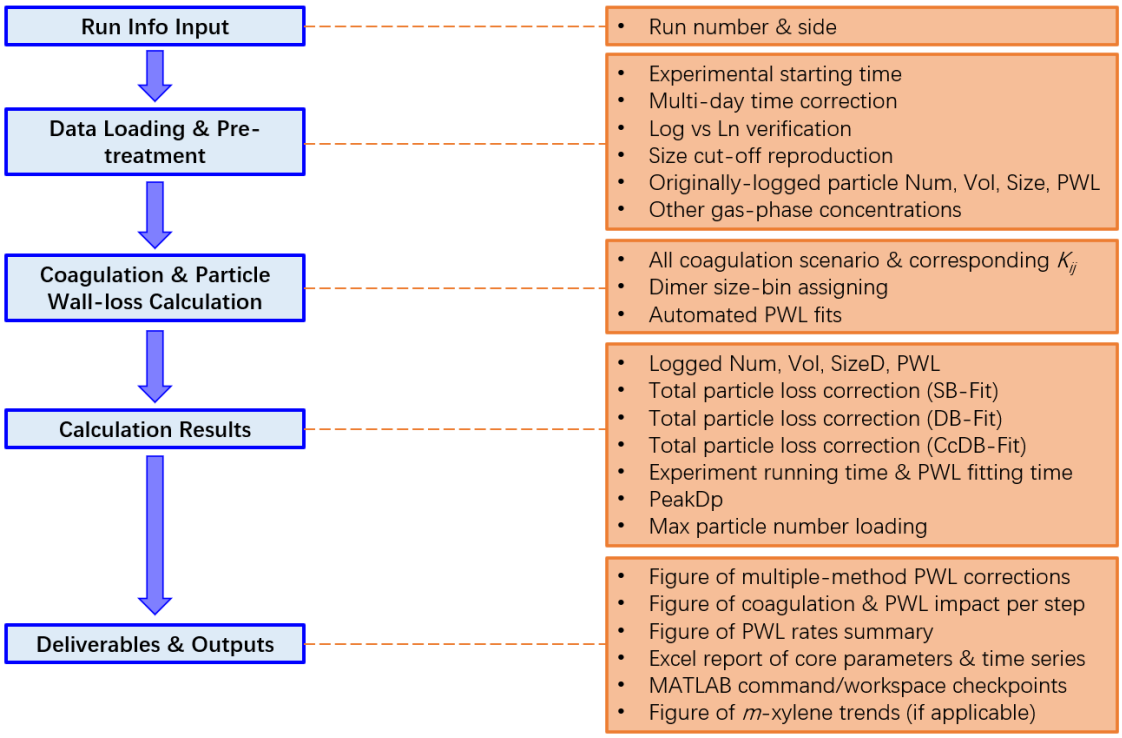

Figure 3-1. The overall logic diagram for the model.

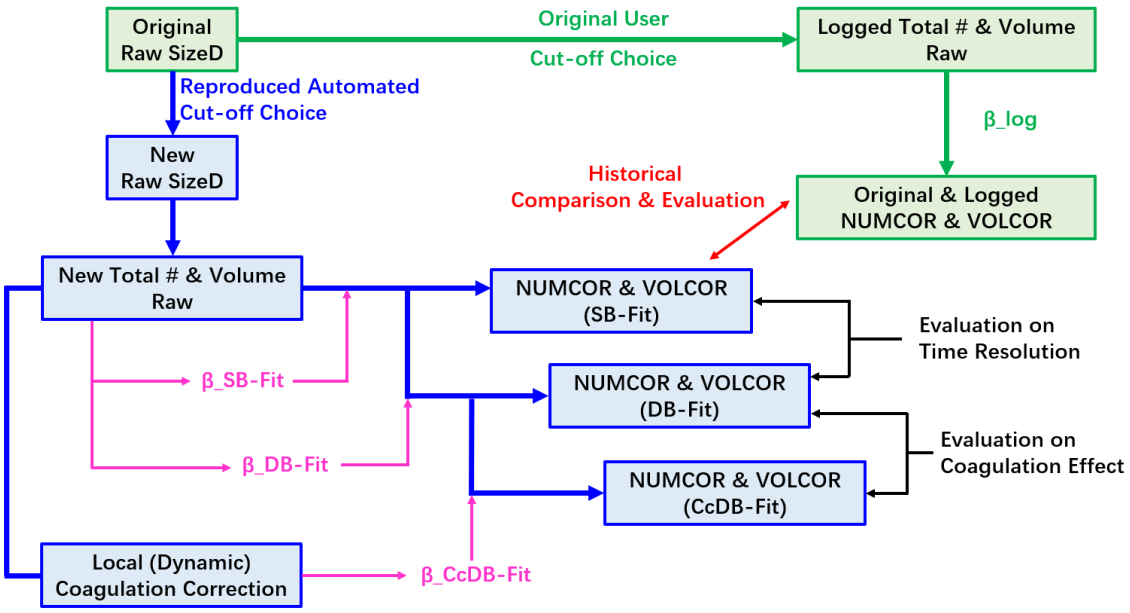

Figure 3-2. Relationship of model outputs using different particle wall-loss correction methods.

3.2.1 Run information input and data loading

Instrumental data from experiments conducted in UCR dual collapsible chambers, including physical/chemical properties of the measured gas-particle system, were historically treated separately and organized using a Macro-based Excel platform. The treated data from each experiment was input into separate worksheets and stored in one Excel file (referred to as the "runfile") per experiment. The new program locates the historical runfile (single mode) or scans through all eligible runfiles in the work folder (batch mode), loading the target data from designated paths for each eligible runfile. Table 3-2 summarizes the loaded data, corresponding instruments and data treatment processes that were re-visited and discussed within the scope of this study. Details of the instruments were discussed in the previous study (Carter et al. 2005).

Table 3-2. Loaded data, instruments and treatment processes within the scope of this study.

Loaded Data	Instrument	Treatment Type
Run Number	N/A	Log-only
Run Side	N/A	Log-only
Experiment Starting Time	N/A	Re-processed
Particle Number	Custom SMPS	Re-processed
Particle Volume	Custom SMPS	Re-processed
Particle Size Distribution	Custom SMPS	Re-processed
m-Xylene Concentration	Agilent 6890 GC-FID	Log-only (if applicable)
Ozone Concentration	Dasibi 1003-AH Ozone Analyzer	Log-only (if applicable)
NO_x Concentration	Thermal Environmental 42C NO_x Analyzer	Log-only (if applicable)
Light Intensity	N/A	Log-only (if applicable)

3.2.2 Data pre-treatment

The model extracts data from historical runfiles, which were generated and organized by varied generations of operators throughout the past two decades. The crude fact exists here that the formats of the available data can be varied, attributed to different operators' habits and/or the software/hardware developments. The data pretreatment section of the program unifies the format of the historical data to prepare for further analysis.

Relative experimental time: Relative experimental time is calculated from the instrumental time and the previous operator logged experimental starting time. Multi-day time correction is applied to eliminate any calculation incompatibilities for instrument outputs with limited precision timestamp formats. An averaged time gap (seconds) between SMPS measurements is also estimated by the ratio of the total experimental time and the total SMPS scans. This is calculated to avoid biased step-wise coagulation and particle wall-loss correction caused by the limited precision of recorded SMPS timestamps. For example, time between SMPS scans of ~ 85s were logged with a formatted time rounded to the nearest minute, resulting in an uneven time progression "08:10, 08:12, 08:13, 08:15" and causing bias when applying Equations 3-3 and 3-4.

Historical data-logging issues: A major update of the SMPS software program (LabVIEW 6 to LabVIEW 19) occurred on 10/01/2019 due to a required systemic upgrade from Windows XP to Win10. This update also resolved a historical log-ln conversion issue embedded in the old SMPS software output that required post-correction in runfiles. For experimental data prior to 10/01/2019 (corresponding to run number EPA2549), all recorded SMPS number concentrations, volume concentrations and size distributions are corrected in the new program by multiplying raw data by 2.3026 to account for an SMPS output error. This correction constant is numerically calculated from the ratio of ln(n) to log(n), where n is any logged value. The program identifies

the processed run number, compares the numerical value to the threshold (2549) and applies the raw data correction when needed. It is noted that historically published UCR data analysis corrected number and volume concentrations post-experiment within the runfile.

Varied SMPS settings: The SMPS settings have evolved several times during the past two decades. Three generations exist: the first generation used a default 70 effective size bins, from 28.2 nm to 725 nm, with an averaged total collection time of 230 seconds; the second generation used a default 70 bins, from 27.8 nm to 712 nm, with an averaged total collection time of 84 seconds and the most-recent generation (by the same LabVIEW/Windows update) used 60 size bins with a flexible size range and total collection time. The program locates where size bin data was stored and determines whether 60 or 70 values should be read and truncates any extra values in the runfile. The number of bins directly defines the size of the coagulation calculation matrix (discussed later).

SMPS size cut-off correction: A size cut-off is applied to SMPS size distributions to remove signal noises at diameters greater than the size peak since small measurement noises there can significantly affect the particle volume distribution. The magnitude of the size cut-off depends on the SMPS performance during the experiment. Figure 3-3 and Figure 3-4 show an example of applying size cut-off correction to one of the experiments (EPA758A) where size cut-off effect is clear. Figure 3-3 presents the cut-off logic and comparison to historical records from one of the SMPS scans. A straight line is linearly fitted through log10 ($dN/dlogD_p$) values versus diameter when the peak curve decreases and $dN/dlogD_p$ values for Dp greater than where the fitted line crosses $log10(dN/dlogD_p) = 1$ are considered noise. Figure 3-4 illustrates the overall cut-off correction result for the total raw particle number and volume. It is noted that the model does not retrieve the historical size cut-off scheme exactly the same way due to technical limitations. Therefore, for each experiment, particle total number and volume concentrations calculated from

historical size cut-off process and from reproduced cut-off process are organized and compared (Figure 3-2). The size-cutoff in the new program produces similar volumes to those historically used.

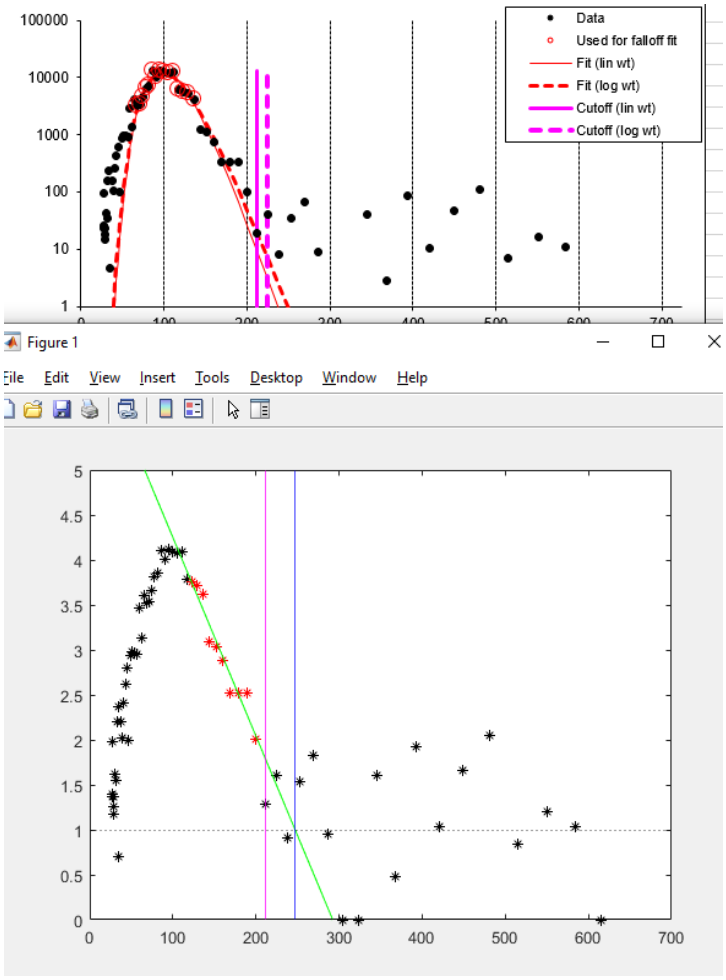

Figure 3-3. Sample calculation of SMPS size cut-off. The pink and blue straight lines are the historical cut-off size and the new cut-off size, respectively.

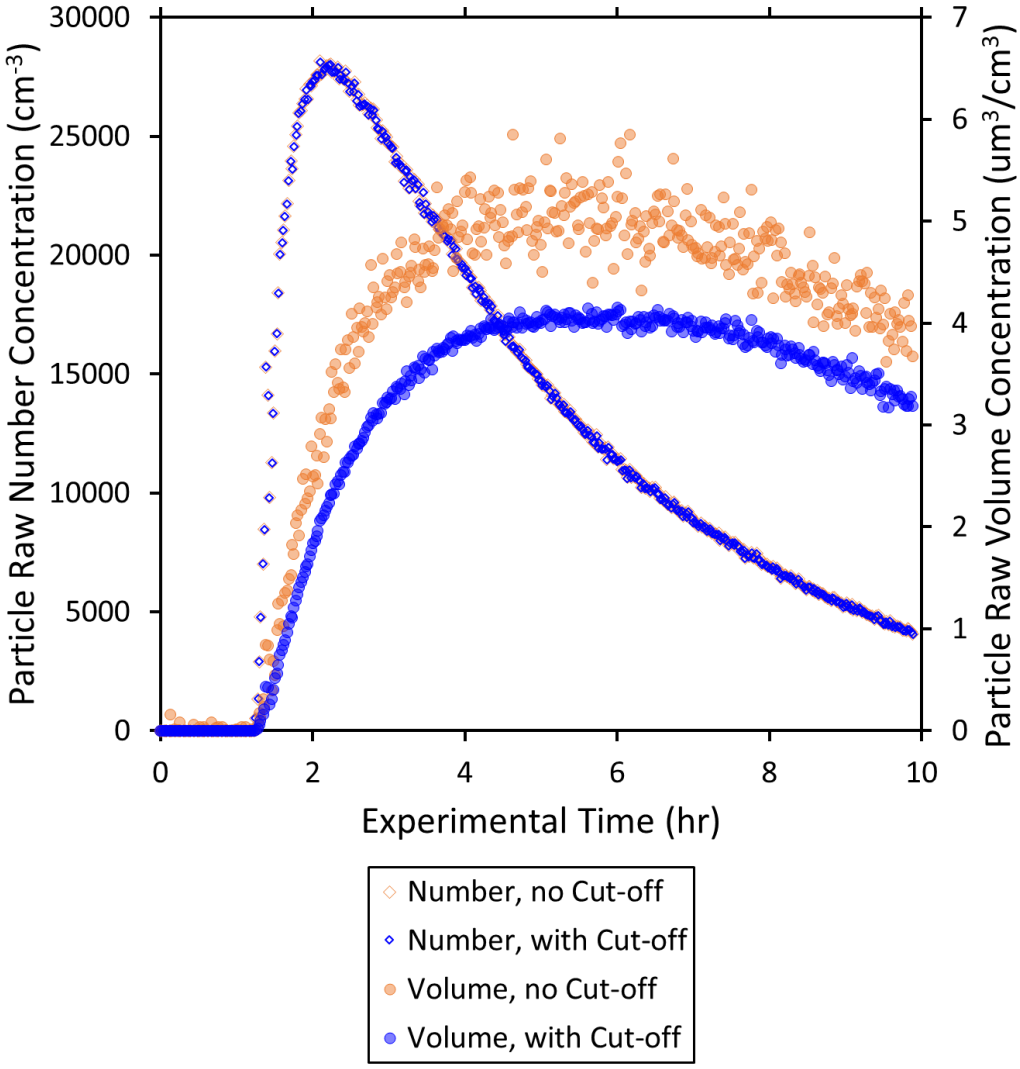

Figure 3-4. Number and volume impact due to application of an SMPS size cut-off for an experiment. Blue markers and orange markers are the SMPS-measured values with and without cut-off applied, respectively. Diamonds refer to particle number concentrations and circles refer to particle volume concentrations.

3.2.3 Coagulation calculation

3.2.3.1 Theories

Generally, for a typical on-going environmental chamber experiment where new-particle formation processes have ended, the aerosol dynamic can be represented as the following (Pierce et al. 2008):

$$\frac{\partial N(Dp,t)}{\partial t} = \left(\frac{\partial N(Dp,t)}{\partial t}\right)_{coagulation} + \left(\frac{\partial N(Dp,t)}{\partial t}\right)_{particle\ wall-loss} + \left(\frac{\partial N(Dp,t)}{\partial t}\right)_{condensation/evaporation} \quad \text{(Equation 3-5)}$$

The coagulation rate between two sizes of particles, J_{ij}, can be expressed as (Fuchs 1964):

$$J_{ij} = K_{ij} N_i N_j \quad \text{(Equation 3-6)}$$

where subscript i and j represent two particle size indices, N_i and N_j represent the number concentration of selected particle size i and j, respectively, and K_{ij} represents the coagulation coefficient between the two sizes of particles, calculated by:

$$K_{ij} = 2\pi(D_i + D_j)\left(D_{p,i} + D_{p,j}\right)\left[\frac{D_{p,i}+D_{p,j}}{D_{p,i}+D_{p,j}+2(g_i{}^2+g_j{}^2)^{1/2}} + \frac{8(D_i+D_j)}{\left(\bar{c}_i{}^2+\bar{c}_j{}^2\right)^{1/2}(D_{p,i}+D_{p,j})}\right]^{-1} \quad \text{(Equation 3-7)}$$

where

$$D_i = \frac{kT}{3\pi\mu D_{p,i}}\left(\frac{5+4Kn_i+6Kn_i{}^2+18Kn_i{}^3}{5-Kn_i+(8+\pi)Kn_i{}^2}\right) \quad \text{(Equation 3-8)}$$

$$g_i = \frac{1}{3D_{p,i}l_i}\left[\left(D_{p,i}+l_i\right)^3 - \left(D_{p,i}{}^2 + l_i{}^2\right)^{\frac{3}{2}}\right] - D_{p,i} \quad \text{(Equation 3-9)}$$

$$\bar{c}_i = \left(\frac{8kT}{\pi m_i}\right)^{1/2} \quad \text{(Equation 3-10)}$$

$$Kn_i = \frac{2\lambda_{air}}{D_{p,i}} \quad \text{(Equation 3-11)}$$

$$l_i = \frac{8D_i}{\pi \bar{c}_i} \quad \text{(Equation 3-12)}$$

where notations and their physical meaning are displayed in Table 3-3.

Table 3-3. Notations used in Equation 3-7 to 3-12.

$\boldsymbol{D_i}$	Diffusivity of particles with size i
$\boldsymbol{g_i}$	Mean distance from a size i particle sphere surface after moving one mean free path, accounting for relative motion
$\boldsymbol{\bar{c}_i}$	Mean velocity of particles with size i
$\boldsymbol{Kn_i}$	Knudsen number of particles with size i
$\boldsymbol{l_i}$	Fuchs' mean free path of particles with size i
$\boldsymbol{k}$	Boltzmann constant
$\boldsymbol{T}$	Absolute temperature
$\boldsymbol{\mu}$	Viscosity of air
$\boldsymbol{m_i}$	Mass of a particle with size i
$\boldsymbol{\lambda_{air}}$	Mean free path of air

Summarized by Charan et al. (2019), the particle size distribution dynamic due to coagulation is then theoretically given by:

$$\left(\frac{\partial N(Dp,t)}{\partial t}\right)_{coagulation} = \frac{1}{2}\int_0^{Dp} K\left(\left[{D_p}^3 - q^3\right]^{1/3}, q\right) N\left(\left[{D_p}^3 - q^3\right]^{1/3}, t\right) N(q,t)\, dq -$$

$$N(D_p,t) \int_0^{\infty} K(q,D_p)\, N(q,t)\, dq \quad \text{(Equation 3-13)}$$

where q is a dummy size, and $K(i,j)$ represents the coagulation coefficient between size i and j. The model makes the following assumptions regarding the coagulation calculation: particle sizes are assumed to be volume-equivalent spherical diameter and the volumes of coagulated particles are assumed to be conserved, regardless of their viscosities. Since $N(Dp,t)$ is constrained by the SMPS-measured format and the scan time is short (< 250 s), the coagulated particles from a

selected time step are not iterated to be coagulated again with the size distribution from the same time step. Additionally, because $N(Dp,t)$ is constrained in every time step, the percentage of particle wall-loss number to the total number during each step is usually < 2%, leading to the assumption that coagulation calculation does not need to be iterated with particle wall-loss simultaneously for each step.

3.2.3.2 Model performance

The collision rate for every single combination among the measured size bins is calculated using Equations (3-6) through (3-12). The accumulated loss and formation of particles from all collision scenarios are then counted. For example, a 60 size-bin system has a total of $(C_2^{60} + 60)$ = 1830 monomer collision scenarios to consider. K_{ij} is then calculated for each particle size combination assuming a temperature of 300 K, a pressure of 1 atm and a particle density of 1.4 g/cm^3 (Malloy et al. 2009; Yu et al. 1999). J_{ij} is then calculated to account for the accumulated loss and formation of particles for each SMPS size bin. Two monomers are lost and one dimer is generated for each coagulation event. It is noted that the calculated J_{ii} (same-size coagulation) by Equation 3-6 will be halved as the result of the indistinguishability of the same-sized monomers (Seinfeld and Pandis 2016). The generated dimers are assumed to have a volume-equivalent spherical diameter and are assigned to the closest size bin. Eventually, the changes on number concentrations in each particle size bin are accumulated for each of the 1830 collision cases. Therefore, the total coagulated particle numbers from each time step can be calculated and accumulated locally to calculate stepwise coagulation-corrected particle total number decays.

3.2.4 Particle wall-loss correction

The fitting start time in batch mode is defined as the timestamp 30 steps later than the timestamp when the maximum raw total particle number is achieved, to ensure the fitting quality from potential data fluctuations (for single mode the user has the option to manually define the fitting start time). Calculation of particle wall-loss rate for the SB-Fit method for a given experiment was discussed previously (Section 3.1). Locally, for a given time step, a matrix consisting of 11 adjacent raw total number concentrations is generated and a first-order decay fit is applied (DB-Fit). Coagulation can also be accounted for at each timestep (Section 3.2.3) to generate a coagulation-corrected number concentration. Thus, a matrix consisting of 11 adjacent coagulation-corrected total number concentrations is also generated by accumulating the coagulated particle numbers for each time step. The same calculation approach as the DB-Fit is then applied to the coagulation-corrected number concentrations decay rate to obtain the CcDB-Fit. Figure 3-5 illustrates how a fitting of 11 adjacent data points reduces the uncertainty of the calculated dynamic decay rates compared to using 2 adjacent data points only. A constant decay rate is applied for timesteps occurring before the fitting start time, averaged from the first half of the calculated dynamic decay rates. The volume correction for particle wall-loss at early experimental time is insensitive to small errors in particle decay rates before and during the nucleation event since no significant particle volumes are present at those times. A constant decay rate is extrapolated and applied for the last 10 timesteps of an experiment by averaging the last 20 dynamic decay rates. This is also a reasonable estimation because measured volumes in later periods of experiments using UCR collapsible chambers are usually low and the particle decay rates are unlikely to rapidly change over this timeframe. Therefore, to correct particle wall-loss using the DB-Fit and CcDB-Fit methods, Equations 3-3 and 3-4 become:

$$\Delta N_i = \frac{N_{(i-1)} + N_i}{2} \left(1 - exp\left(-\beta_{dynamic}\left(t_i - t_{(i-1)}\right)\right)\right) \ , i \geq 2 \qquad \text{(Equation 3-14)}$$

$$\Delta V_i = \frac{V_{(i-1)} + V_i}{2} \left(1 - exp\left(-\beta_{dynamic}\left(t_i - t_{(i-1)}\right)\right)\right) \ , i \geq 2 \qquad \text{(Equation 3-15)}$$

where $\beta_{dynamic}$ represents dynamic particle wall-loss rates from either DB-Fit method or CcDB-Fit method. The cumulative wall-deposited total particle number and volume concentrations are then calculated and added to the measured raw values to calculate the wall-loss corrected values. When calculating total corrected particle number concentrations using CcDB-Fit method, cumulative coagulated total particle numbers are also added to correct for coagulation loss. Volume change due to coagulation is neglected (see Section 3.2.3).

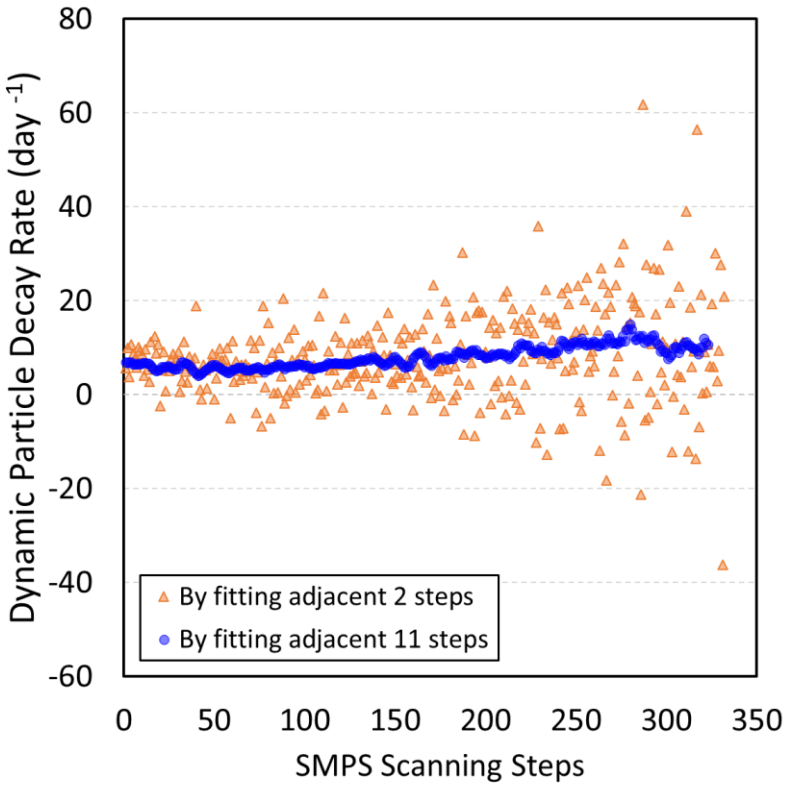

Figure 3-5. Dynamic particle decay rates when calculated using neighboring measurements (adjacent 2 steps) and using 11 adjacent data points. The reduced noise in dynamic particle decay rate is observed for the 11 adjacent data point fit.

3.2.5 Model outputs and deliverables

The program generates in batch mode a number of outputs to evaluate the SMPS results and corrections in experiments from multiple perspectives, including one clustered report summarizing all experiments as well as archived figures and excel documents unique to the specific experiment (Table 3-4). Detailed program output time series are recorded in the output Excel files and are summarized in Table 3-5 and Table 3-6. The parameters in Table 3-5 are used for the retrospective analysis of all available experiments and program output time series in Table 3-6 supports targeted future analysis. In Table 3-5, under the category "Particle decay rates", the item "Averaged early-period decay rate, CcDB-Fit (day^{-1})" is averaged from CcDB-Fit within the first hour after wall-loss fitting starts, indicating the average particle wall-loss pattern in early experimental periods. Under the category "Particle wall-loss corrected volume concentrations", all Final VOLCOR (corrected volume) values of an experiment are averaged from the last 7 data series of which the highest values and lowest values are discarded, to avoid bias caused by instrumental fluctuations; the item "Change of final VOLCOR due to time-resolved correction (%)" is calculated by the percent change from "Final VOLCOR, re-processed, SB-Fit (um^3/cm^3)" to "Final VOLCOR, DB-Fit (um^3/cm^3); the item "Change of final VOLCOR due to coagulation correction" is calculated by the percent change from "Final VOLCOR, re-processed, DB-Fit" to "Final VOLCOR, CcDB-Fit"; the item "Change of final VOLCOR overall" represents the overall update of VOLCOR from historical approaches, calculated by the percent change from "Final VOLCOR, re-processed, SB-Fit" to "Final VOLCOR, CcDB-Fit". Under the category "Other parameters", the item "Max particle number loading (cm^{-3})" is linearly back-extrapolated from the measured particle numbers 10^{th} and 30^{th} steps after reaching its maximum, to avoid potential data noise at the maximum; the item "Coagulation contribution (%)" is calculated from the

percentage of total coagulated particle numbers to the max particle number loading; the item "Averaged early-period PeakDp (nm)" averages the measured peak size of the particles within the first hour after wall-loss fitting starts, providing an indication of averaged particle size during the main nucleation phase. Outputs that will be discussed in the later sections are highlighted in green. Additionally, several notes for Table 3-6 – the item "Volume out-of-bound due to coagulation, step-wise (um^3/cm^3)" and "Volume out-of-bound due to coagulation, cumulative (um^3/cm^3)" records the volume of coagulated particles, which are too large to be detected by SMPS. These values are usually very small. The item "Particle wall-loss percentage (%)" and "Coagulation percentage (%)" represent the percentages of wall-deposited and coagulated particle numbers from an SMPS scan, respectively, out of the current measured total number. The item "Corrected volume, Omega = 1 (um^3/cm^3)" calculates the corrected total particle volume assuming deposited particles follow gas-particle partitioning exactly as if they were suspended, where omega refers to the extent of growth of already-deposited particles (Trump et al. 2016). This trend is calculated using Equation 3-16 for step *i* and stored in the document for potential future use:

$$V_{\omega=1,i} = \frac{N_{particle\ wall-loss\ corrected,i}}{N_{raw,i}} V_{raw,i} \quad \text{(Equation 3-16)}$$

The program also supports customized analysis options to further explore an experiment in single-runfile mode. For example, experimental starting time and wall-loss fitting starting time can be manually overwritten to evaluate the sensitivity of the fitting time selection; SMPS size cut-off switch can be turned off to evaluate its impact; SB-Fit can be manually input to evaluate traditional wall-loss correction; coagulation coefficients can be tuned, etc. Additionally, development options are also open to future users to load and analyze properties obtained from other instruments in the runfile. In short, the platform developed is a starting point to explore and

unlock the large data accumulated for thousands of experiments over the two decades using UCR collapsible chambers. Therefore, the model is well-noted for any potential development or revision by future users.

Table 3-4. Deliverables of the model.

Deliverable Names	Content	File Type	Data Source
Retrospective Summary (Batch Mode Only)	Statistics of core parameters	Excel file	All experiments
A_Historical Evaluation	Comparison to historical cut-off & fitting choices	Figure	Single experiment
B_NumVol Summary	Clustered time series of all analyzed NumVol corrections		
B_NumVol Dynamic	Cleaned NumVol time series from SB-Fit to DB-Fit		
B_NumVol Coagulation	Cleaned NumVol time series from DB-Fit to CcDB-Fit		
B_NumVol Update	Cleaned NumVol time series from SB-Fit to CcDB-Fit		
C_Decay Rates	Summary of all evaluated decay rates		
D_Section Decay	Averaged particle decay per quartile of an experiment		
F_Loss Impact	Percentage of PWL and Coag corrected number concentrations		
Individual Experiment Summary	Statistics of core time series	Excel sheet	

Table 3-5. Parameters recorded in Excel file output – Retrospective Summary.

Category	Parameter Item
General information	Run number
	Side
	Year
	Chamber batch
Particle decay rates	Decay rate, logged, SB-Fit (day^{-1})
	Decay rate, re-processed, SB-Fit (day^{-1})
	Averaged decay rate, CcDB-Fit (day^{-1})
	Averaged early-period decay rate, CcDB-Fit (day^{-1})
Particle wall-loss corrected volume concentrations (VOLCOR)	Final VOLCOR, logged, SB-Fit ($um^3\ cm^{-3}$)
	Final VOLCOR, re-processed, SB-Fit ($um^3\ cm^{-3}$)
	Final VOLCOR, DB-Fit ($um^3\ cm^{-3}$)
	Final VOLCOR, CcDB-Fit ($um^3\ cm^{-3}$)
	Change of final VOLCOR due to time-resolved correction (%)
	Change of final VOLCOR due to coagulation correction (%)
	Change of final VOLCOR overall (%)
Other parameters	Max particle number loading (cm^{-3})
	Total coagulated particle number (cm^{-3})
	Coagulation contribution (%)
	Experimental time (hr)
	Wall-loss fitting time (hr)
	Smoothed time gap between SMPS scans (s)
	Averaged final peakDp (nm)
	Averaged early-period peakDp (nm)
Parameters specifically for *m*-xylene SOA experiments (optional)	Max ozone concentration (ppb, if applicable)
	Initial NO concentration (ppb, if applicable)
	Consumed *m*-xylene concentration (ppb, if applicable)
	Light intensity (min^{-1}, if applicable)

Table 3-6. Time series of program outputs recorded in Excel file output – Individual Experiment Summary.

Category	Time Series Item
Timestamps	Absolute time in string format
	Absolute time in numerical format (day)
	Relative time in numerical format (day)
Dynamic decay rates	Decay rate, DB-Fit (day^{-1})
	Decay rate, CcDB-Fit (day^{-1})
Total number	Raw number, logged (cm^{-3})
	Raw number, re-cutoff (cm^{-3})
	Corrected number, logged (cm^{-3})
	Corrected number, SB-Fit (cm^{-3})
	Corrected number, DB-Fit (cm^{-3})
	Coagulated number generated from each step (cm^{-3})
	Raw+PWL number, CcDB-Fit (cm^{-3})
	Raw+PWL+Coag number, CcDB-Fit (cm^{-3})
Total volume	Raw volume, logged ($um^3\ cm^{-3}$)
	Raw volume, re-cutoff ($um^3\ cm^{-3}$)
	Corrected volume, logged ($um^3\ cm^{-3}$)
	Corrected volume, SB-Fit ($um^3\ cm^{-3}$)
	Corrected volume, DB-Fit ($um^3\ cm^{-3}$)
	Corrected volume, CcDB-Fit ($um^3\ cm^{-3}$)
	Corrected volume, Omega = 1 ($um^3\ cm^{-3}$)
	Volume out-of-bound due to coagulation, step-wise ($um^3\ cm^{-3}$)
	Volume out-of-bound due to coagulation, cumulative ($um^3\ cm^{-3}$)
Others	Raw PeakDp (nm)
	Coagulation-corrected PeakDp (nm)
	Particle wall-loss percentage (%)
	Coagulation percentage (%)

3.3 Results and Discussion

3.3.1 Retrospective overview

Historical experiments using multiple generations of UCR dual 90-m^3 collapsible chambers in the past two decades are re-visited. The experiments span from EPA001 (02/14/2002) to EPA2569 (02/03/2020) and normally both sides of the dual-chamber are used to conduct independent experiments (e.g., EPA2000a, EPA2000b). First, the program was used to load all available experiments that were recorded in the program-favored format. Second, a manual check of all generated number and volume curves was performed to filter out experiments with invalid data or fits. Next, experiments that needed minor changes were recorded and re-processed manually later and last, experiments with particle wall-loss fitting time less than 3 hours were discarded. This semi-automated filter reduced the number of analyzed experiments to 1939 (each side of the dual-chamber is counted individually). Over the past two decades, the UCR dual-chamber facility has been maintained regularly with replacement of the environmental chambers every 1~2 years. Modifications on chamber designs were applied during some of the replacement processes; however, the overall collapsible feature and approximate volume of the chamber remained consistent. Table 3-7 summarizes the evolution of different batches of collapsible chambers and their service periods. Experiments conducted often focused on SOA formation from varied precursors with or without the presence of seed aerosols. The program was executed to compare DB-Fit and CcDB-Fit to the formerly used SB-Fit method (SB-Fit is also named the "number-averaged" method by Nah et al. 2017). Evaluation with DB-Fit takes care of the dynamic change of wall-loss rates within individual experiments while CcDB-Fit further accounts for coagulation.

Table 3-7. Summary of UCR collapsible chamber batches and services.

Batch Name	Chamber Serial Number	Service Start Time	Service Start Run
Collapsible_A	16 & 17	Jul., 2002	EPA028
Collapsible_B	18 & 19	Sep., 2003	EPA169
Collapsible_C	20, 21 & 22	Aug., 2004	EPA337
Collapsible_D	23 & 24	Dec., 2005	EPA481
Collapsible_E	25 & 26	Feb., 2007	EPA683
Collapsible_F	27 & 28	Dec., 2007	EPA860
Collapsible_G	29 & 30	Aug., 2009	EPA1032
Collapsible_H	31 & 32	May, 2010	EPA1172
Collapsible_I	33 & 34	Jul., 2011	EPA1460
Collapsible_J	35 & 36	May, 2014	EPA1836
Collapsible_K	37 & 38	Jul., 2015	EPA2074
Collapsible_L	39 & 40	Nov., 2017	EPA2316
FixedVol_M[a]	41	Apr., 2021	EPA2617

[a]: This new-generation 120-m^3 fixed-volume chamber will be discussed in the next chapter.

Figure 3-6 summarizes the particle wall-loss rates calculated using SB-Fit, DB-Fit, and CcDB-Fit for each generation of chambers across the two decades. The comparison specifically includes averaged particle wall-loss rates from CcDB-Fit from the first hour after wall-loss fitting starts (referred to as CcDB-Fit-Early), providing the best estimation on particle wall-loss immediately following the nucleation burst. Each data point within the boxes is derived from an individual experiment–for the orange (CcDB-Fit) and blue (CcDB-Fit-Early) boxes, each data point is an average of the dynamic decay rates calculated within an individual experiment. The averaged DB-Fits have negligible numerical differences from the SB-Fits and are not displayed. As expected, no strong trends in particle wall-loss are observed among generations of chamber bags using the different correction methods indicating that the particle wall-loss mechanism for the chamber was steady over the two decades of collapsible chamber use. The averaged particle wall-loss rate decreased from 6.92 day^{-1} (average of gray boxes, Figure 3-6) to 6.00 day^{-1} (average of orange boxes) by accounting for coagulation. The averaged coagulation-corrected particle wall-loss rate in early periods of experiments was lower at 4.17 day^{-1} (average of blue boxes). The difference between 6.00 day^{-1} (CcDB-Fit) and 4.17 day^{-1} (CcDB-Fit-Early) indicates particle wall-loss rates dynamically change within the UCR collapsible chambers.

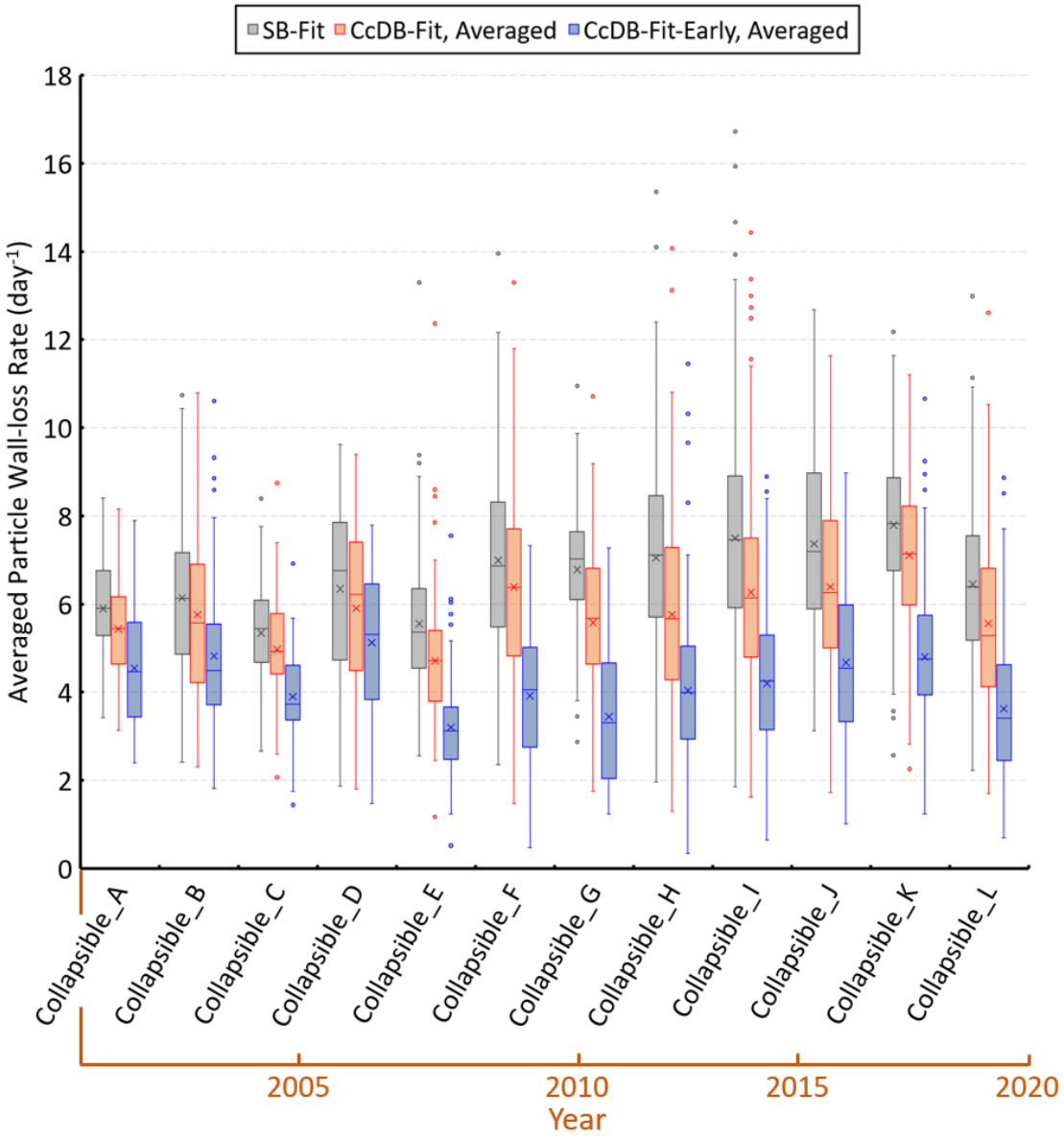

Figure 3-6. Summary of averaged particle wall-loss rates among different generations of UCR collapsible chambers in the last two decades. Gray boxes represent the decay rates derived by SB-Fit, which is the traditional single-factor size-independent coagulation-uncorrected rates. Orange boxes represent the average decay rates by CcDB-Fit, where the decay rates are coagulation-corrected and dynamic within an individual experiment. Blue boxes represent the averaged decay rates in the first hour after wall-loss correction starts (CcDB-Fit-Early).

A distribution of the maximum measured particle loadings as well as the particle wall-loss rates corresponding to the measured particle loadings are shown (Figure 3-7). A clear trend of increasing discrepancies between the gray and orange boxes is observed with increased maximum particle number loadings, consistent with the increased importance of coagulation correction when more particles are present. The majority of experiments in UCR collapsible chambers have maximum particle loadings between 10^4 and 5×10^4 cm^{-3}, where the effect of particle-particle coagulation starts to emerge between the wall-loss correction methods. No significant trends are observed between different particle loadings after accounting for coagulation. The particle wall-loss rates using traditional and updated correction methods are further plotted for all evaluated experiments (Figure 3-8). Generally, the updated decay rates are lower than decay rates derived from the traditional method due to coagulation correction. The differences grow with increased coagulation occurring for higher particle loadings. Data points above the 1:1 line represent experiments where the influence of particle dynamics outweighed corrections for coagulation.

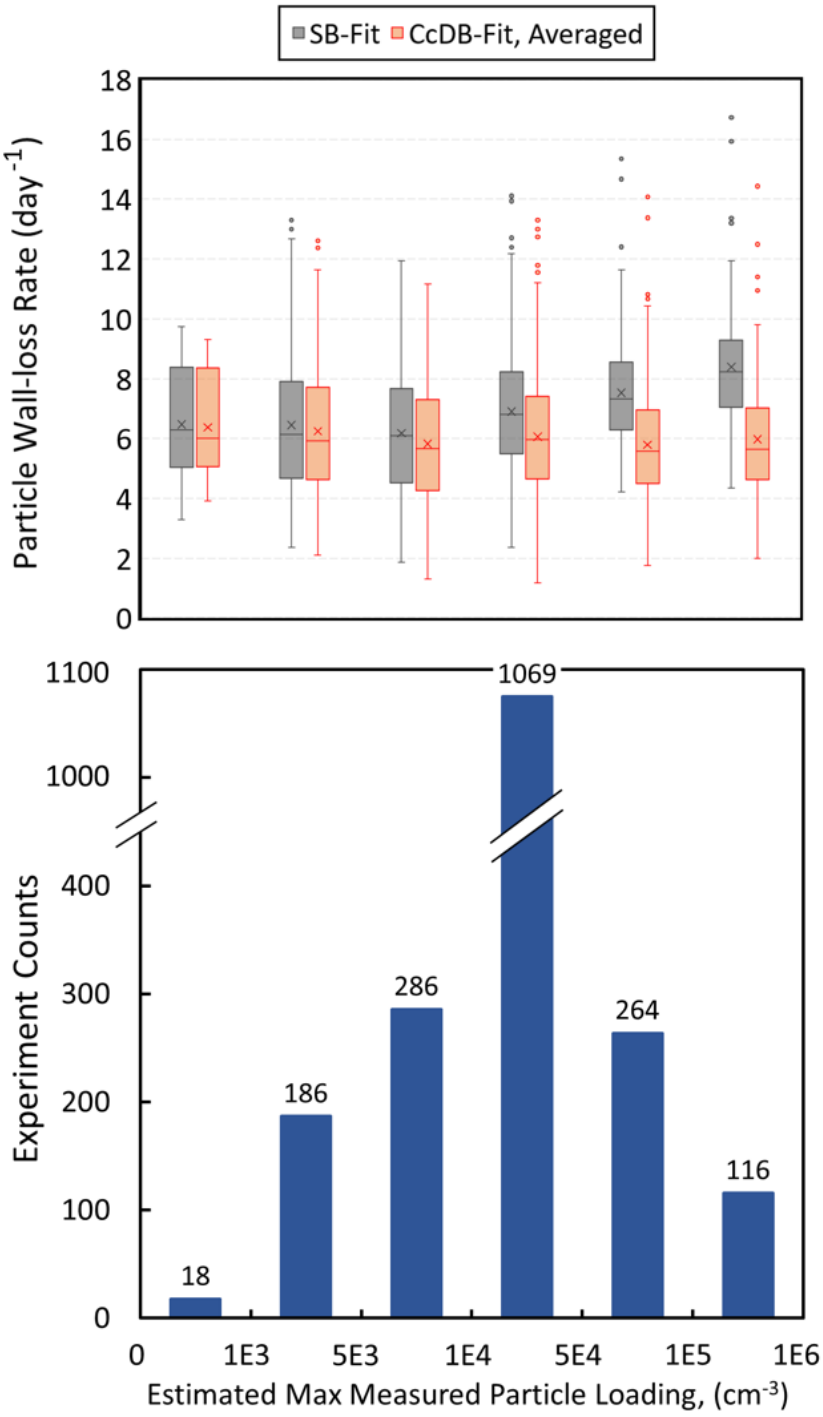

Figure 3-7. Summary of maximum measured particle number loadings from all analyzed experiments and the corresponding particle wall-loss rates from: 1) SB-Fit method (gray), representing the traditional single-factor size-independent coagulation-uncorrected rates and 2) CcDB-Fit method, averaged (orange), representing the most up-to-date particle wall-loss correction method for UCR collapsible chambers.

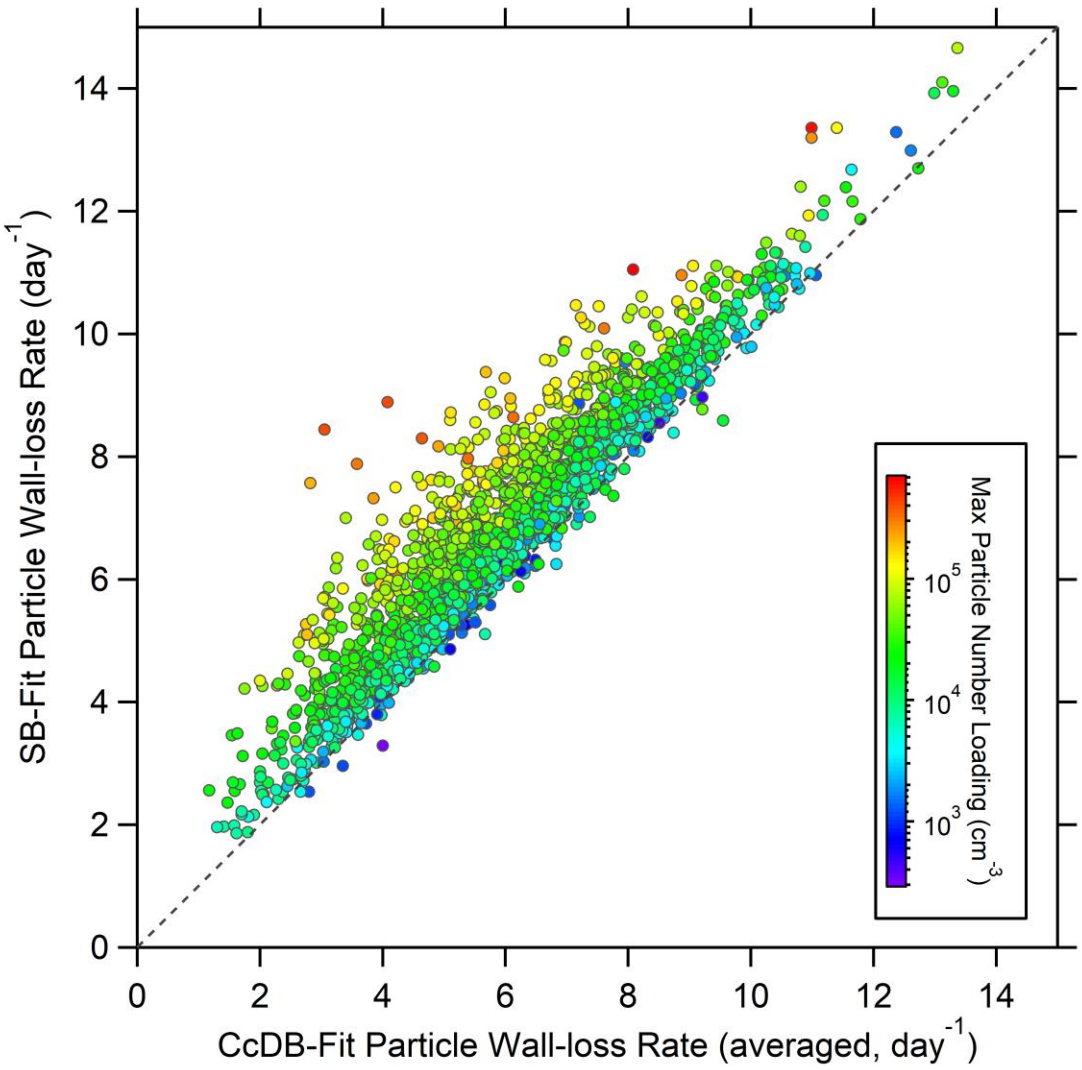

Figure 3-8. Comparison of particle wall-loss rates derived from the traditional correction method (SB-Fit, y-axis) and the most updated method (CcDB-Fit, x-axis), colored by the maximum particle number loadings. Each dot represents derived results from each individual experiment.

3.3.2 Effect of aerosol dynamics

Aerosol dynamics, including dynamics of particle-particle coagulation and dynamics of particle-wall deposition, affect particle loss processes in UCR collapsible chambers. Model outputs for four past experiments spanning 2 decades with representative normal (N1, N2) or high (H1, H2) particle number loadings are shown (Figure 3-9 to Figure 3-12) along with experimental details (Table 3-8). Figure 3-9 presents the dynamic particle wall-loss rates as a function of time with and without accounting for coagulation. The coagulation correction is observed to significantly impact the early periods of experiment H1 and H2 due to high particle number loadings early in these experiments. As experimental time progresses the decay rates with and without coagulation approach each other, indicating the decreased significance of coagulation as particle numbers decrease due to coagulation and wall-loss. Additionally, coagulation-corrected dynamic decay rates (red markers) increase for all four experiments. This can be possibly explained by:

1) Freshly nucleated particles are not expected to be charged;

2) Particle wall-loss rates are enhanced by the increased size-dependent electrostatics effect when suspended particles approach chamber-specific charge steady-state;

3) Particle size increase due to gas-particle partitioning processes and coagulation;

4) Increase in surface-area-to-volume ratio during the course of the experiment;

5) Increase in surface charge of wall materials (Teflon) with greater surface contact with the enclosure surface (aluminum) as the volume of the chamber reduces.

The competition between particle wall-loss and coagulation is illustrated (Figure 3-10) as the percentage of particle loss due to wall-deposition or coagulation for each SMPS timestep. The loss of particles is dominated by wall-deposition for experiments N1 and N2. However, in

experiments with high particle number loadings (H1 and H2), coagulation loss of particle numbers can be one magnitude higher than the wall-deposition loss in early periods. The maximum critical time where coagulation can be dominant in overall particle number losses can be concluded as 2~3 hours since the displayed two high-loading experiments are amongst the highest particle number loadings ever tested in UCR collapsible chambers.

Figure 3-11 and Figure 3-12 are the number and volume corrected concentration time series after corrections using all three methods. Particle total number corrections using traditional SB-Fit method results in wall-loss corrected particle numbers decreasing later in the experiments (Figure 3-11, Experiment N1 and N2) since the method does not dynamically account for increasing particle wall-loss as the experiment progresses. Additionally, wall-loss corrected particle numbers using both SB-Fit and DB-Fit methods experience a decrease after reaching peak concentrations and before reaching the plateau (Figure 3-11, Experiment H1 and H2) as neither method properly accounts for particle number loss due to coagulation. DB-Fit is superior to SB-Fit because it captures the dynamic change in particle wall-loss that is averaged out by SB-Fit. The third method, CcDB-Fit, successfully handles both dynamic particle wall-losses and coagulation corrections simultaneously and is observed to yield the most reasonably corrected number concentration time profile for all four experiments (Figure 3-11). Similarly, the CcDB-Fit also leads to the most reasonable volume corrected time profile (Figure 3-12).

The error in historical wall-loss corrected volume estimates due to neglecting coagulation is described by "volume over-correction percentage due to coagulation", which is calculated as:

$$V_{overcorrection\ percentage\ coagulation} = \frac{V_{DB-Fit} - V_{CcDB-Fit}}{V_{DB-Fit}} \times 100\% \qquad \text{(Equation 3-17)}$$

where $V_{DB\text{-}Fit}$ and $V_{CcDB\text{-}Fit}$ refer to the corrected final particle volume concentrations using DB-Fit and CcDB-Fit, respectively. The volume over-correction percentage due to coagulation can be observed as the differences between the red- and green-curves in Figure 3-12. The volume over-

correction percentage due to coagulation versus maximum particle number loadings for all experiments is seen in Figure 3-13 with colors representing the time after the experiment starts. As expected, greater over-correction of the final particle volume for increased maximum particle concentration is observed when coagulation is ignored. No strong trends are observed between over-correction ratios and time since the start of experiment (< 8 hr and > 8 hr) for the nearly 2000 experiments. This is due to the decreasing significance of particle number loss due to coagulation compared to wall-loss as the experiments progress (Figure 3-10). It is noted for chambers with lower wall-loss rates (e.g., new fixed-volume UCR chamber, Chapter 4) that coagulation will impact experiments for longer durations than observed for UCR collapsible chambers.

The over-correction percentages for all investigated experiments are found in Figure 3-14. One can visualize these over-correction percentages using Figure 3-12. The volume over-correction due only to dynamic particle wall-loss rates (red box and whisker) represents the differences between the blue- and red-curves (DB-Fit vs SB-Fit). The volume over-correction percentage due only to coagulation (green box and whisker) represents the differences between the red- and green-curves (CcDB-Fit vs DB-Fit). The overall volume over-correction due to both coagulation and dynamic particle wall-loss (pink box and whisker) represents the differences between the blue- and green-curves (CcDB-Fit vs SB-Fit). The volume correction when accounting for only dynamic particle wall-loss rates tends to be smaller than the correction for coagulation. Overall, a median over-correction for total particle volume ~10% was observed in the historical data. Further, CcDB-Fit is recommended to be used for the most accurate corrected volume estimates from the historical data as it corrects for dynamic particle wall-loss and coagulation.

To summarize: 1) dynamic particle wall-loss rates are observed within a single experiment due to evolution of particle size, particle charge distribution, chamber surface charge and chamber geometry; 2) for UCR collapsible chambers, when high particle number loadings (>> 5×10^4 cm^{-3}) are present, coagulation loss can drive particle number loss but only for the first several hours; 3) compared to the traditional SB-Fit method, the CcDB-Fit method performs much better by accounting for both coagulation and dynamic changes to particle wall-loss rates.

Table 3-8. Summary of four experiments in the past decades representing two normal experiment particle number loadings and two high experiment number loadings.

Name in This Work	Historical Run Number	Year of Experiment	Chamber Batch Name	Maximum Particle Number Loading (cm^{-3})
Experiment N1	EPA1107B	2010	Collapsible_G	1.3×10^4
Experiment N2	EPA2372A	2018	Collapsible_L	1.0×10^4
Experiment H1	EPA1899B	2014	Collapsible_J	2.8×10^5
Experiment H2	EPA1441A	2011	Collapsible_H	3.8×10^5

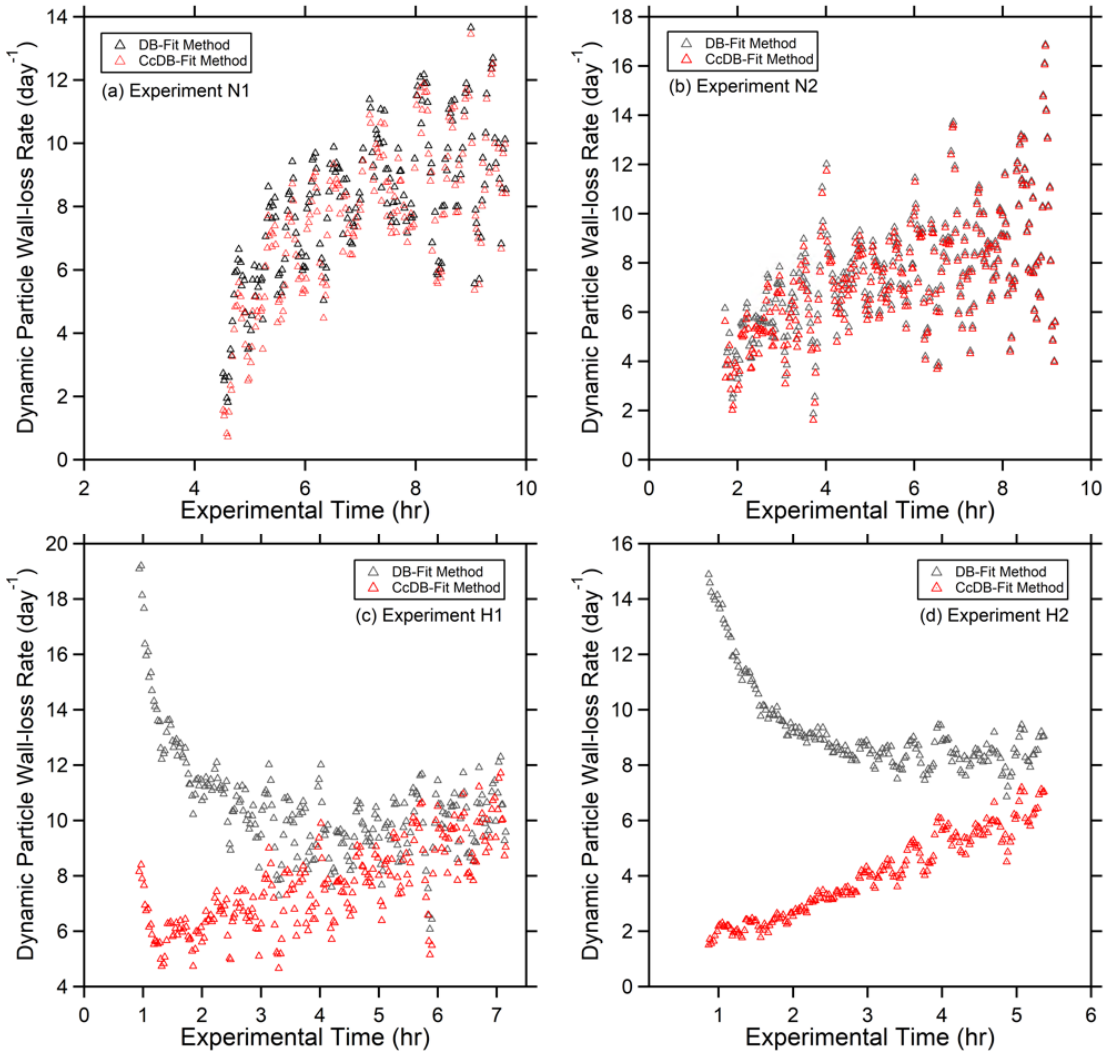

Figure 3-9. Summary of dynamic particle wall-loss rate versus time for four experiments in the past decades with **(a)** and **(b)** representing normal particle number loading; **(c)** and **(d)** representing high particle number loading. Black markers represent real-time particle wall-loss rate calculated by DB-Fit method and red markers represent calculation results using coagulation-corrected CcDB-Fit method.

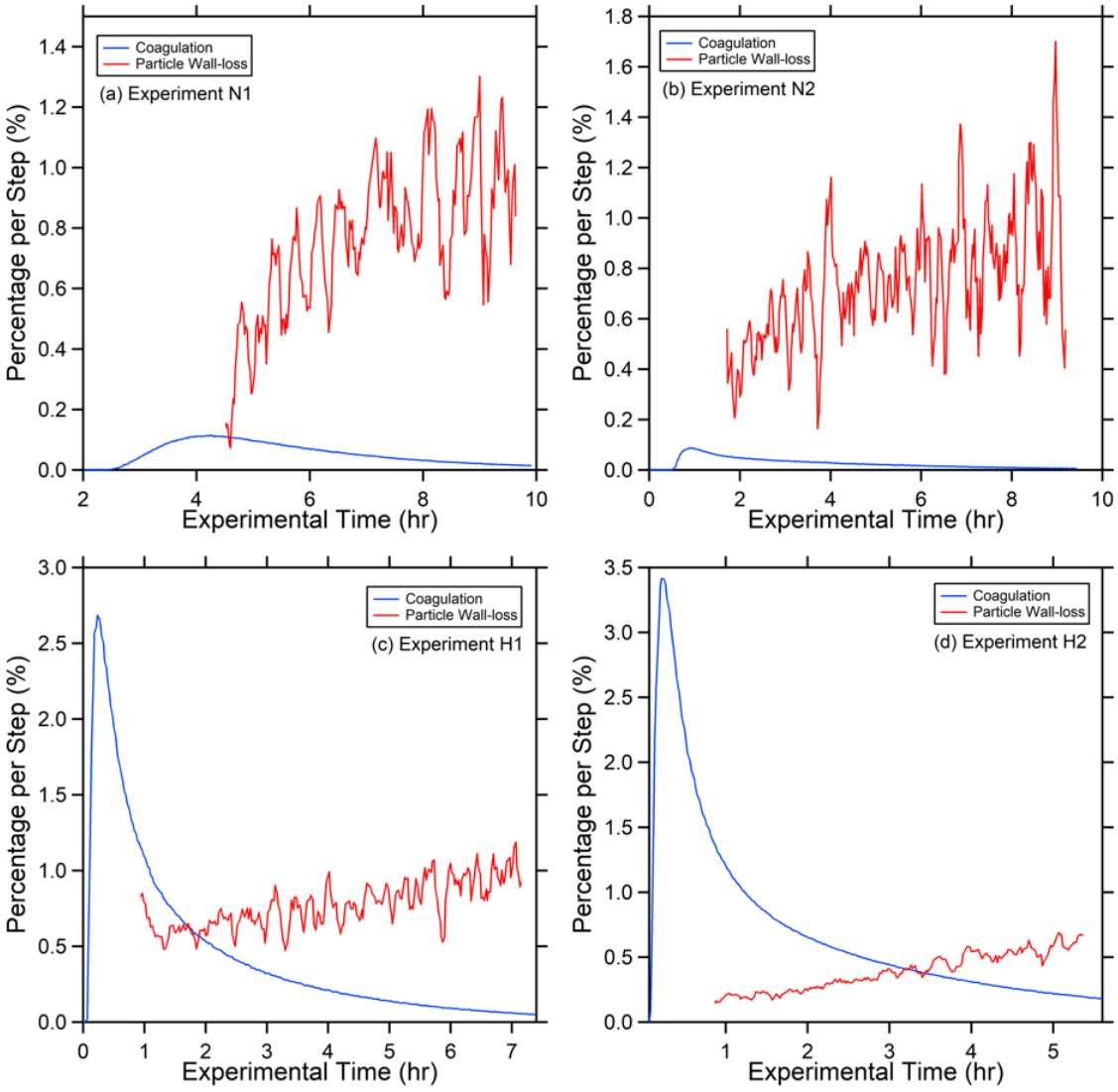

Figure 3-10. Summary of number percentage wall loss per time step for four experiments in the past two decades with **(a)** and **(b)** representing normal particle number loading; **(c)** and **(d)** representing high particle number loading. Blue curves represent the ratio of calculated particle loss due to coagulation to the measured total particle numbers for each timestep and red curves represent the ratio of calculated particle loss due to wall-deposition to the total particles for each step.

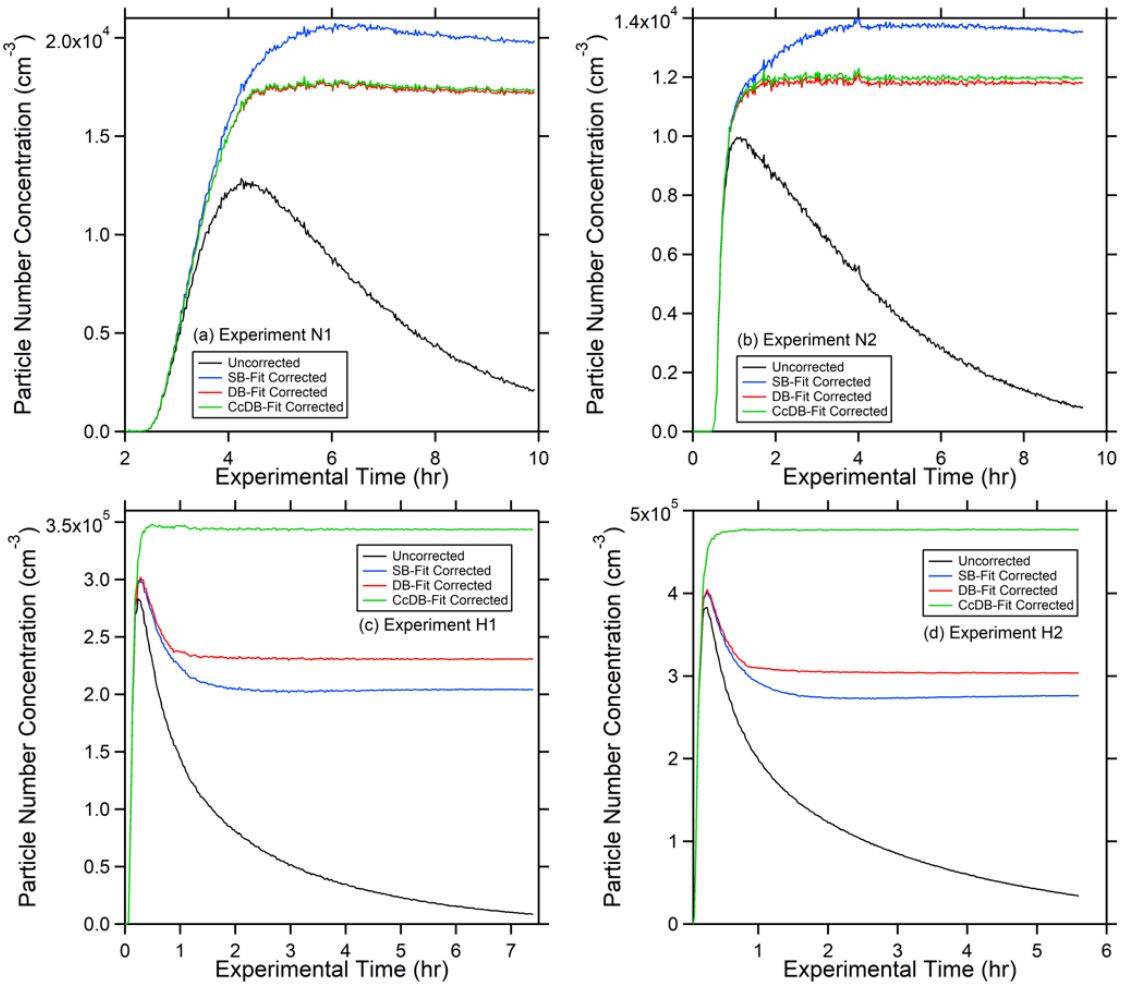

Figure 3-11. Summary of corrected particle number concentration progressions using different wall-loss correction methods for four experiments in the past two decades with **(a)** and **(b)** representing normal particle number loading; **(c)** and **(d)** representing high particle number loading.

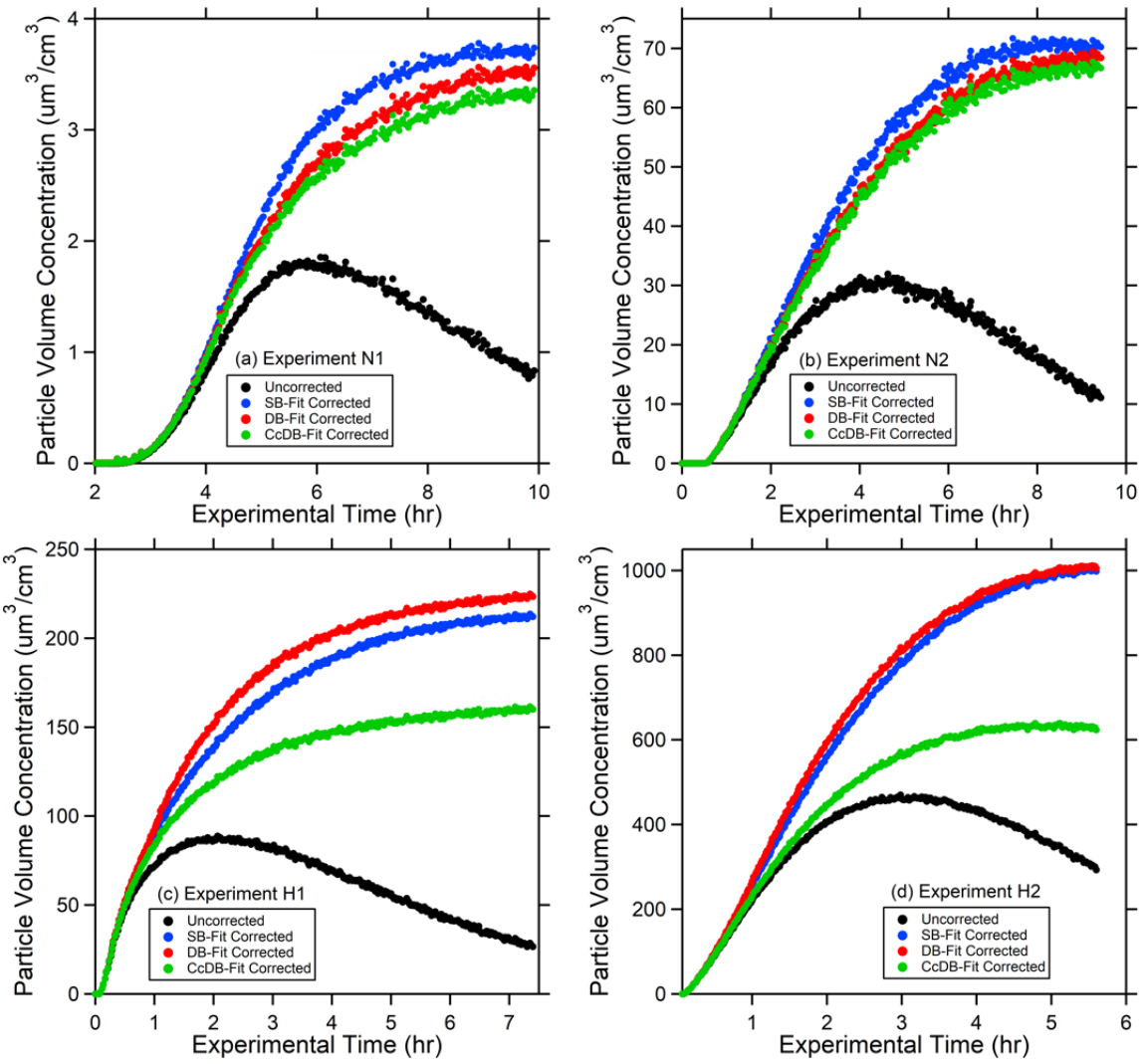

Figure 3-12. Summary of corrected particle volume concentration progressions using different wall-loss correction methods for four experiments in the past two decades with **(a)** and **(b)** representing normal particle number loading; **(c)** and **(d)** representing high particle number loading.

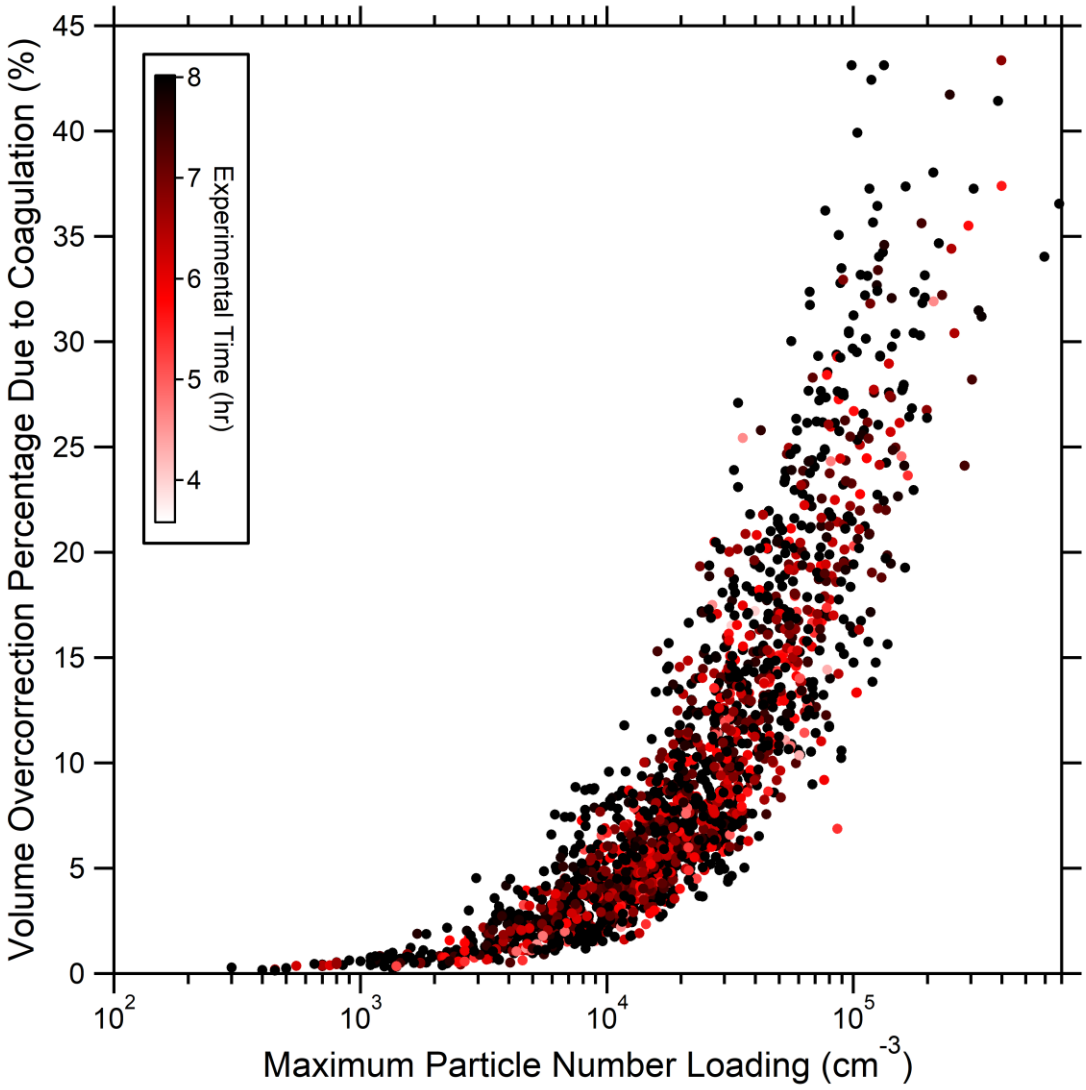

Figure 3-13. Summary of final particle volume over-correction percentages due to coagulation (Equation 3-17) for all evaluated 1939 experiments at different particle number loadings, colored by the experimental time. Each marker represents an individual chamber experiment. Black markers represent experiments ≥ 8 hours.

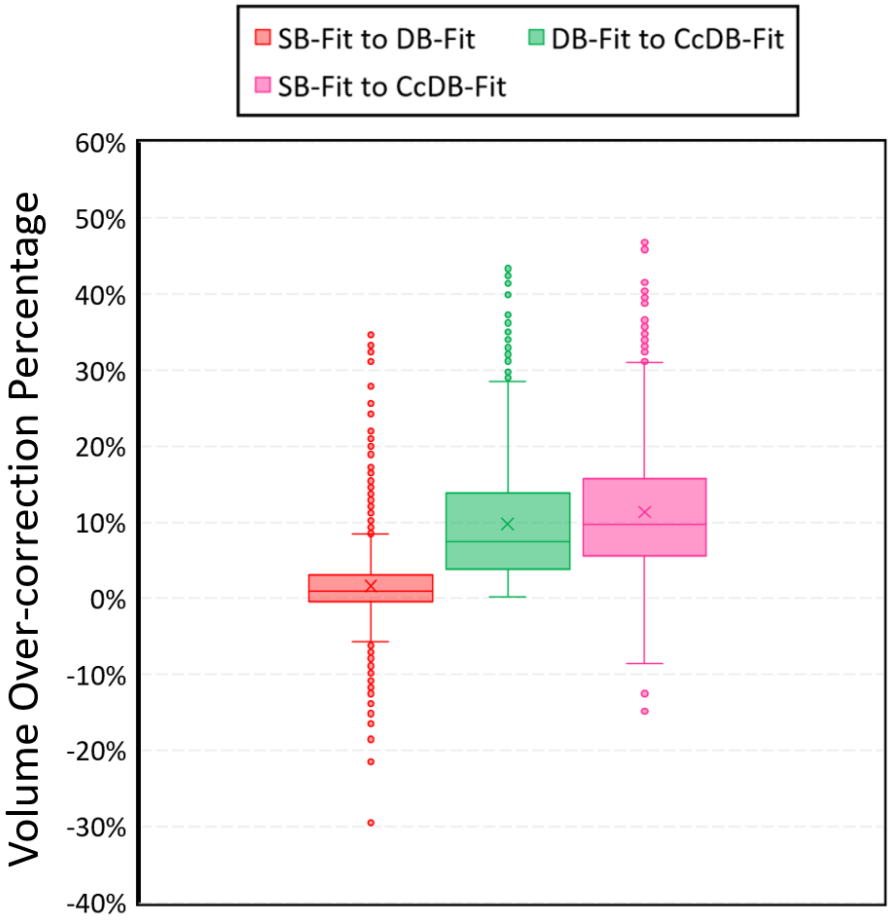

Figure 3-14. Summary of final particle volume over-correction ratios between particle wall-loss correction methods for all evaluated 1939 experiments. Red box and whisker represent the historical final volume over-correction by not accounting for dynamic wall-loss rate (SB-Fit to DB-Fit), green box and whisker represent the historical volume over-correction by not accounting for coagulation correction (DB-Fit to CcDB-Fit) and pink box and whisker represent the final volume over-correction for not accounting for either dynamic wall-loss rate or coagulation (SB-Fit to CcDB-Fit).

3.3.3 Effect of coagulation

Cocker et al. (2001) previously reported the characteristic time scale of coagulation for particles in a chamber as ~ 3.1 days for a particle number concentration of 10^4 cm^{-3} for seeded experiments and ranging from 200 seconds to 56 hours for particle number concentrations from 10^4 to 10^7 cm^{-3} for experiments without seed aerosol. Therefore, for most seeded experiments as well as for nucleation experiments producing a number concentration on the order of 10^4 particles cm^{-3}, the time scale for coagulation is much greater than the time scale of the experiment suggesting that coagulation processes were unimportant for such experiments. However, more recently, the effect of coagulation has gained greater attention (e.g., Charan et al. 2019; Sunol et al. 2018; Wang et al. 2018). In the current work we revisit the impacts of particle coagulation on particle size distribution and calculated particle wall loss in experiments using UCR collapsible chambers.

This section compares CcDB-Fit to DB-Fit particle wall-loss rate calculations to further explore the impact of coagulation on wall-loss correction. Figure 3-12, Figure 3-13 and Figure 3-14 (the green box) directly show that final corrected volume/mass concentrations of particles in an experiment can be systematically over-corrected for particle wall-loss when coagulation is neglected; the highest observed percentage to date for UCR collapsible chamber experiments is ~ 45%. The positive bias from the 1:1 line for DB-Fit and CcDB-Fit final corrected volumes for all experiments is shown in Figure 3-15.

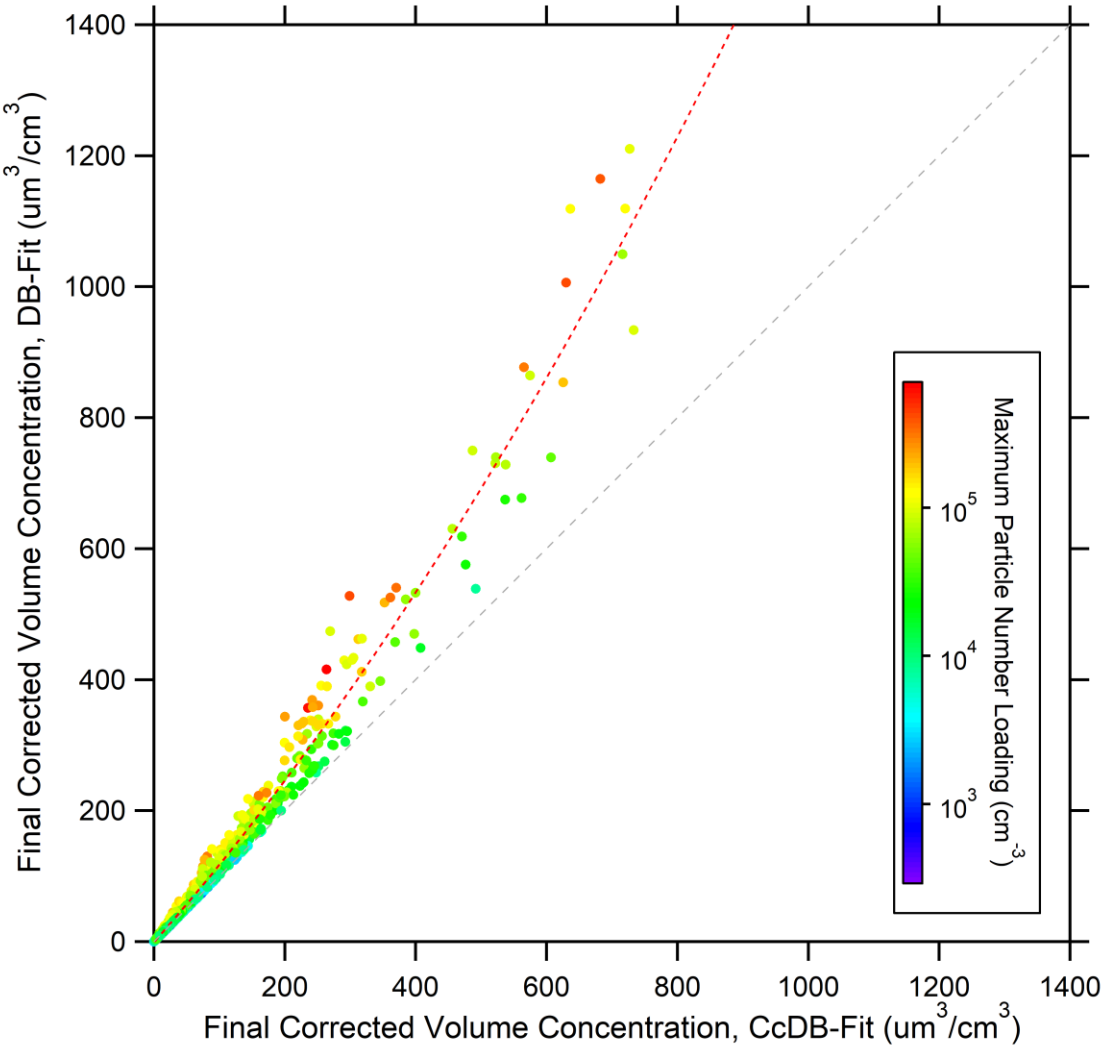

Figure 3-15. Comparison of final corrected volume concentrations using DB-Fit method versus CcDB-Fit method, colored by maximum particle number loading presented in the experiment. Each data point is derived from an individual experiment.

Figure 6-B from Charan et al. (2019) provides theoretical calculations on coagulation effects in a chamber. Coagulation impact on final number loss percentage due to particle number loading and particle size one hour after start of wall-loss correction is investigated in the current work for measured data from 1939 experiments in UCR collapsible chambers (Figure 3-16). Final coagulation percentage is calculated from the ratio of total coagulated particle numbers in an experiment to the measurable maximum particle number loadings since it is impossible to directly measure maximum total particle loadings in experiments due to particle losses. The final coagulation percentage positively correlates with particle number loadings and is insensitive to particle peak size, consistent with the theoretical calculation from Charan et al. (2019). The absolute values of the measured percentage are generally lower than the theoretical calculation due to the fact that particle wall-loss influences the measured total particle number loss. The maximum measured particle numbers will be reduced by an average of 30% due to coagulation processes for the most common particle number loadings in UCR collapsible chambers ($10^4 \sim 5 \times 10^4$ cm^{-3}). This percentage can reach 90% for experiments with our most-extreme particle loadings ($> 4 \times 10^5$ cm^{-3}). The impact of coagulation on the final volume over-correction to account for particle wall-loss (Equation 3-17) are further illustrated in Figure 3-17. For historical experiments conducted in UCR collapsible chambers in the past two decades, a minimum of ~ 5% overestimation is expected when coagulation is neglected (DB-Fit) vs. when coagulation is accounted for (CcDB-Fit) for experiments with maximum measured particle number loading exceeding 10^4 cm^{-3}. The overestimation percentage increases to ≥ 15% when particle loadings higher than 5×10^4 cm^{-3} are present. Additionally, Figure 3-18 presents the statistics of volume over-correction percentages due to the coagulation effect with different types of experimental precursors, while Figure 3-19 presents peak particle sizes in early periods (1 hour after wall-loss correction) of the experiments after the nucleation burst and at the end of the experiments.

Experiments conducted in UCR collapsible chambers with biogenic precursors, especially mono- and sesqui-terpenes, tend to have larger nucleation bursts, resulting in more significant coagulation effects, while ones with anthropogenic precursors, tend to have less of a coagulation effect. *a*-Pinene ozonolysis experiments conducted in UCR collapsible chambers had some of the largest coagulation impacts and formed some of the largest particles. Regardless, the previously-discussed estimations only provide bulk part trends and suggestions; therefore, the over-correction percentage derived by revisiting a UCR collapsible chamber experiment should be evaluated by the program for individual precursors and experiments.

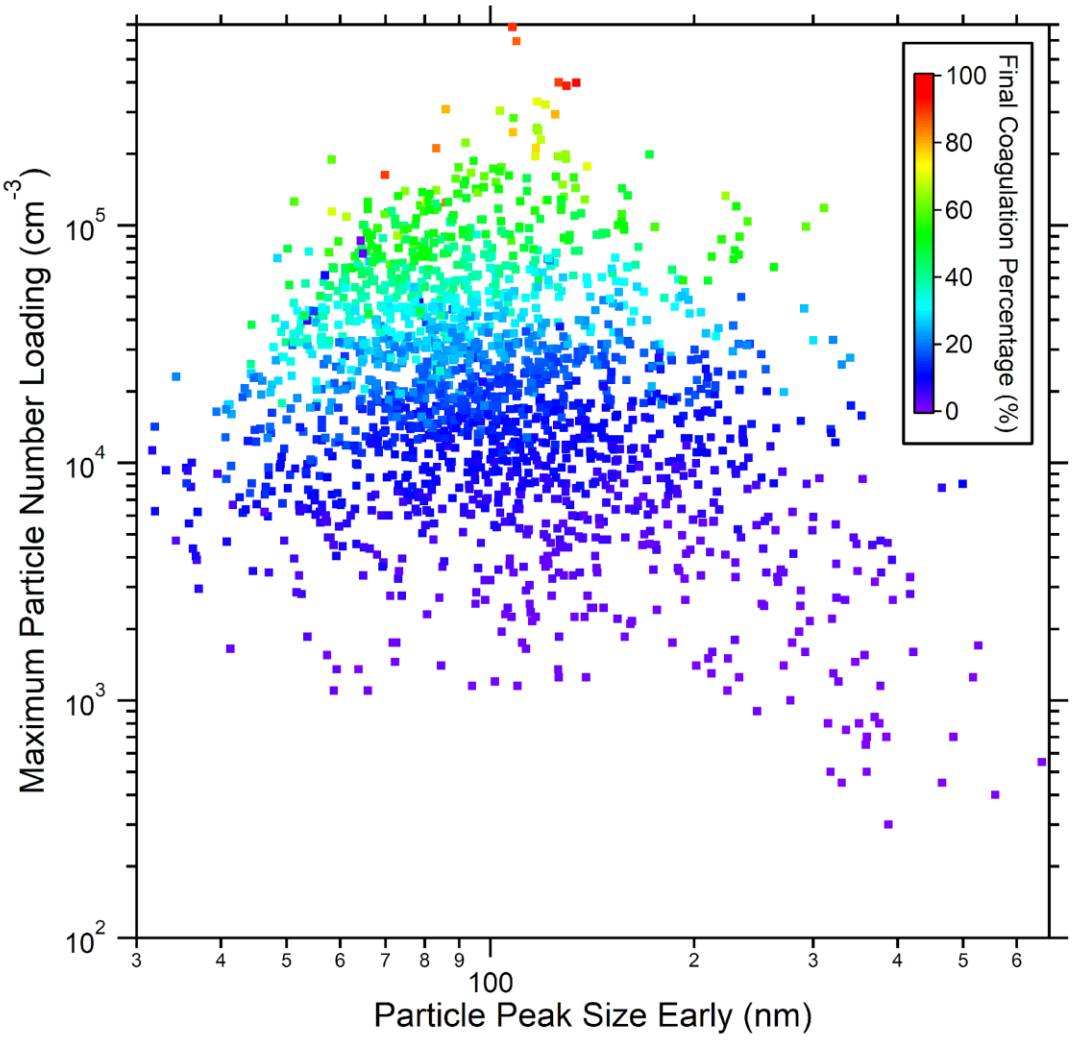

Figure 3-16. Plot of final coagulation percentage as a function of maximum particle number loading and particle peak size at the early period of an experiment after the nucleation burst (see Section 3.3.1). Each data point is derived from an individual experiment.

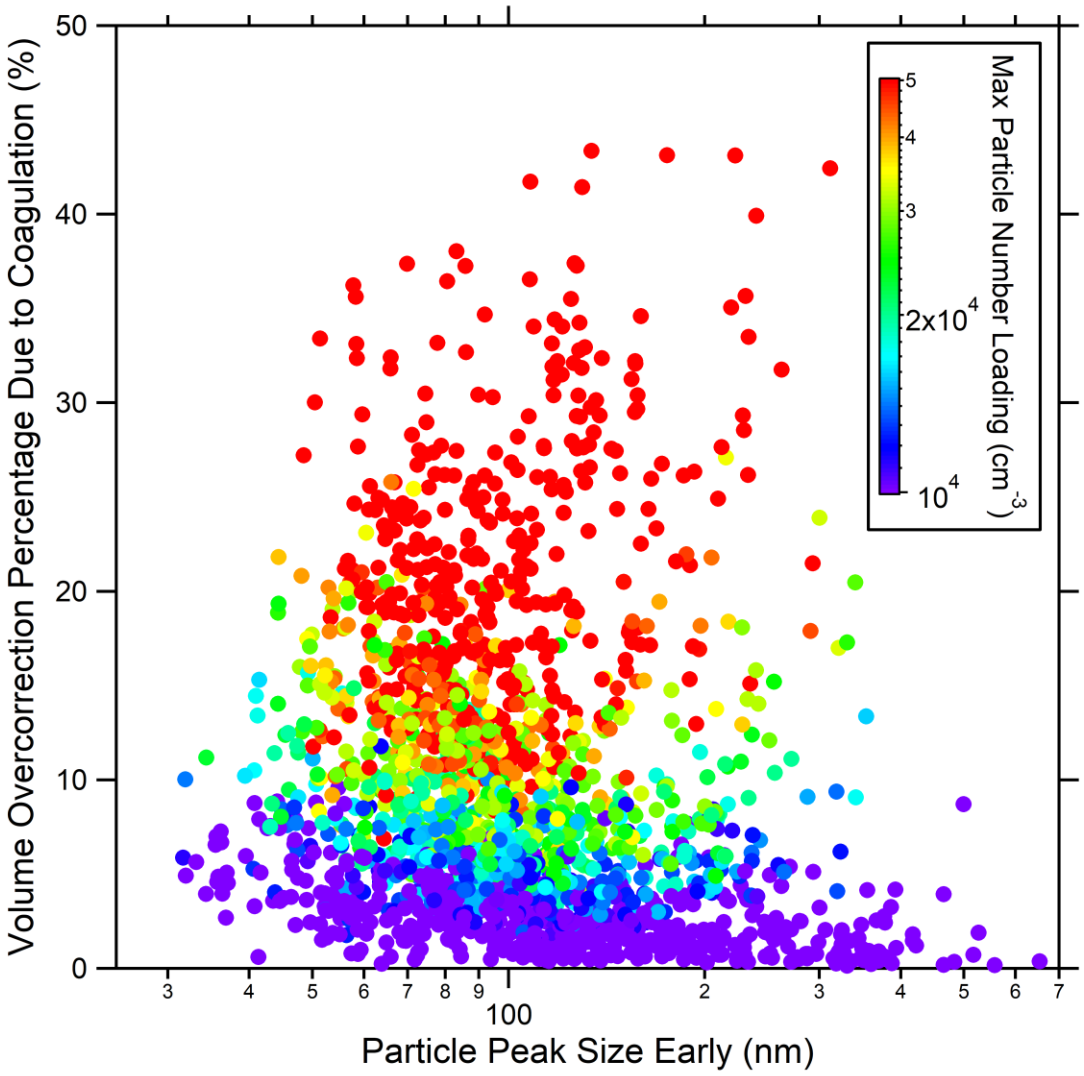

Figure 3-17. Plot of volume overcorrection percentages due to not accounting for coagulation as a function of particle peak size (1 hour after wall-loss correction starts), colored by the maximum measured particle number loadings. The color bar lower and upper bounds have been manually cut to the thresholds of 10^4 and 5×10^4 cm^{-3}, respectively. Each data point is derived from an individual experiment.

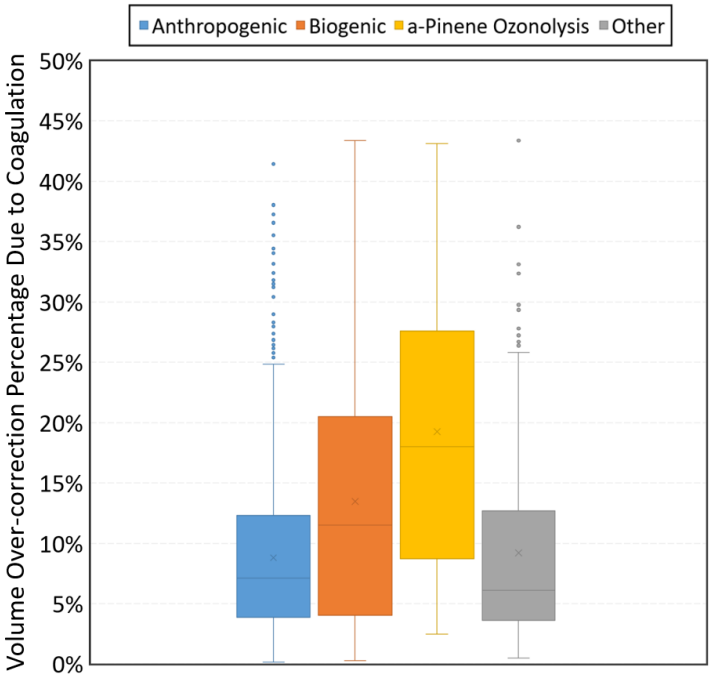

Figure 3-18. Volume overcorrection percentages due to not accounting for coagulation for different classes of SOA precursors.

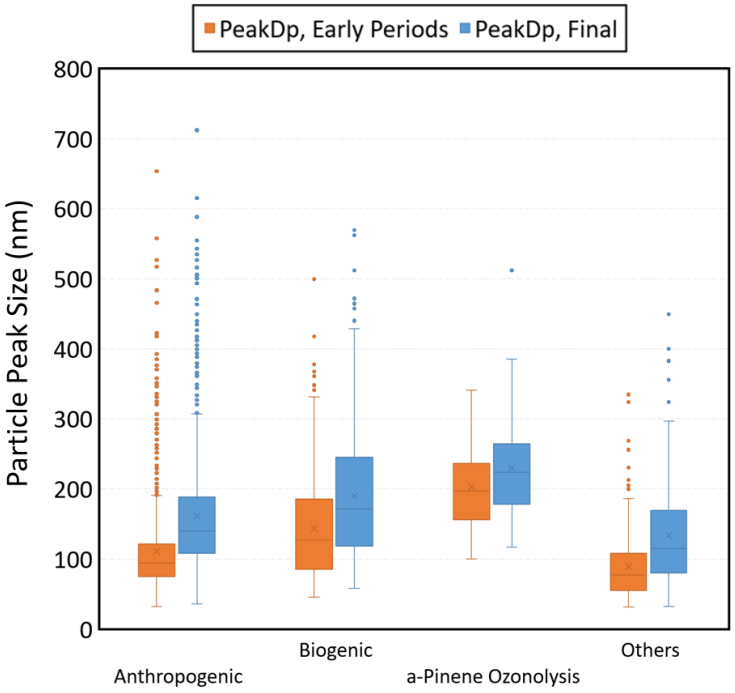

Figure 3-19. Particle peak sizes 1 hour after wall-loss correction starts (orange) and at the end of the experiments (blue), respectively, for different classes of SOA precursors.

3.4 Conclusions

Traditionally, an experiment-specific, size-independent, coagulation-uncorrected single-factor particle wall-loss rate was derived directly from measured SMPS data to correct particle wall-loss for each individual experiment conducted in UCR collapsible chambers. Using this approach overestimated the corrected particle volume/mass by not accounting for particle-particle coagulation. Dynamic changes of particle wall-loss rates were observed in UCR collapsible chambers, attributed to the changes of particle size, particle charge distribution, chamber surface charge along with chamber geometry. A particle coagulation dynamics model was developed using the CcDB-Fit particle wall-loss correction method to accurately account for both coagulation and particle dynamics by calculating the dynamic coagulation-corrected particle wall-loss rates for each experiment.

A program, embedded with the updated model, was developed and applied to re-evaluate the particle wall-loss correction results from ~ 2000 historical experiments conducted in UCR collapsible chambers over the past two decades. The retrospective summarizes the difference of particle wall-loss rates calculated using traditional and updated correction methods across different years and generations of chamber bags. The particle wall-loss rate discrepancies between the different correction methods grew with increasing particle number loadings. Dynamic changes of particle wall-loss rates within individual experiments were verified by direct observations. Particle number loss due to coagulation was observed to have a significant impact on the total particle number loss during the first few hours of the experiment when higher particle number loadings were present. Overall, minimum of ~ 5% and ~ 15% overestimation of the final corrected particle volume are determined when coagulation is not accounted for in experiments with at least 10^4 cm^{-3} particles and 5×10^4 cm^{-3} particles, respectively.

Chapter 4: Experimental Characterization of Particle Wall-loss Behaviors and Development of a New Particle Loss Model for the Next-generation UCR 120-m^3 Fixed-volume Chamber

4.1 Introduction

Minimizing uncertainties from particle-loss corrections are critical for accurately quantifying aerosol yield from environmental chamber experiments. Explored by the previous chapters, particle wall-loss behaviors in the UCR previous-generation dual 90-m^3 collapsible Teflon chambers were dominated by electrostatic-driven deposition (Sections 2.3.1 and 2.3.2). The percentage of particle wall-loss correction (average wall-loss rate) versus measurable mass yield for UCR collapsible chambers was more significant compared to reported values from other smaller chambers (Le et al. 2023; Charan et al. 2018; Carter et al. 2005; Cocker et al. 2001). The traditional size-independent experiment-specific single-factor coagulation-uncorrected particle wall-loss rates, derived from fitting the total measured particle number decays in later periods of experiments with no new particle formation, (referred to as "number-averaged method" in Nah et

al. (2017) and “SB-Fit method” in the previous chapter), were determined to be insufficient at addressing correction uncertainties induced by dynamic change of particle wall-loss patterns during an experiment and also particle-particle coagulation (Sections 3.3.1 – 3.3.3). An updated semi-empirical particle wall-loss correction method calculating and applying the dynamic size-independent coagulation-corrected particle wall-loss rates was introduced in the previous chapter to minimize these correction uncertainties. However, further mitigation strategies were still warranted for the UCR collapsible chambers to minimize surface charging and reduce uncertainties in particle wall-loss correction.

In this study, particle wall-loss characterizations are conducted using a monodisperse particle injection method with minimal coagulation for the UCR new-generation 120-m^3 fixed-volume chamber, which was constructed to replace the previous-generation dual collapsible chambers. Efforts have been taken in the new chamber system to minimize particle wall-loss rates caused by chamber surface charge. A three-component particle wall-loss correction method has been established for the new chamber to characterize the particle wall-loss pattern for the new chamber and correct for particle losses due to chamber dilution, wall-deposition and coagulation. The new method is also evaluated against historically-used correction methods for a series of SOA experiments. Size-dependent, coagulation-corrected particle wall-loss patterns from regular polydisperse seed-only experiments are also evaluated and compared to the patterns obtained through monodisperse experiments.

4.2 Experimental

4.2.1 The new-generation 120-m^3 fixed-volume chamber

The UCR/CE-CERT new-generation 120-m^3 fixed-volume chamber (referred to as UCR fixed-volume chamber for future discussion, also categorized as "FixedVol_M" or bag No. 41 in Table 3-7) was designed and constructed to replace the previous-generation dual collapsible chambers used since 2003 (referred to as UCR collapsible chambers). The summary of chamber design parameters and features are shown below (Table 4-1, modified from Table 3-1, Li 2022). The schematic diagram of the chamber is also presented (Figure 4-1). Only the chamber design updates are discussed in this section as instrumental details are already discussed in another study (Carter et al. 2005). Overall, the new chamber is designed to have a larger volume and to operate at lower precursor concentrations when desired. It is also designed to minimize the impact of electrostatic charges on chamber surfaces in order to reduce the overall particle loss rate and achieve longer experimental durations (from typically ~ 8 – 10 hr to up to multiple days, compared to the previous-generation collapsible chambers). It is noted that since the chamber design has been migrated from collapsible to fixed-volume, the differential pressure between the inside of the chamber and the enclosure room during experiments is lower, resulting in non-negligible air exchange through leaks on the chamber surfaces. Therefore, chamber dilution needs to be accounted for when correcting particle losses in the UCR fixed-volume chamber.

Table 4-1. Summary of different generations of core chambers in UCR.

Item	UCR Collapsible Chambers	UCR New Fix-volume Chamber
Surface Material	FEP Teflon®	FEP Teflon®
Max Volume Capacity	~ 90 m^3 (dual)	~ 120 m^3
Dimensions	Collapsible, ~ 6 m (H) x ~ 3 m (W) x ~ 5 m (D)	~ 4.6 m (H) x ~ 4.9 m (W) x ~ 5.3 m (D)
Surface Area to Volume Ratio	1.43 m^{-1} – ~ 5 m^{-1} [a]	~ 1.22 m^{-1}
Chamber Surface Charge Control	No control	External soft x-ray photo ionizers (Hamamatsu)
Chamber Surface Charge Constants	N/A	±10 V [b]
Pure Air System	Aadco 737series (Cleves, Ohio) air purification system, followed by canisters containing granulated charcoal, Purafil® and molecular sieve (13X, Delta Adsorbents), followed by heated Carulite 300® and a particle filter pack	Same as UCR collapsible chamber
Cleaning Method	Hand/glove touch	Touchless
Light Sources	Arc lights or blacklights [c]	Blacklights
Light Intensity	Up to $k_{NO2 \rightarrow NO}$ = 0.402 min^{-1}	Up to $k_{NO2 \rightarrow NO}$ = 0.402 min^{-1}
Temperature Capacity	5 – 40°C	5 – 40°C
Relative Humidity Capacity	0 – 100%	0 – 100%
Shortest Distance from Chamber to Light Sources	~ 5 m	~ 4.4 m
Differential Pressure (Relative to Chamber Enclosure Room)	> 2.5 Pa when idling; ~ 8.7 Pa during experiments	2.0 – 3.0 Pa when idling; ~ 3.7 Pa during experiments
Chamber Dilution	Negligible	Not negligible
Background SOA	< 0.14 ug m^{-3}, tested by injecting 1 ppm H_2O_2 [d]	< 0.014 ug m^{-3}, tested by injecting 2 ppm H_2O_2 [d]

[a]: gradually increases within experiments and might reach 5 m^{-1} when the chamber has fully collapsed.
[b]: measured by Ultra Stable Surface Volt Meter, Model USSVM II, Alphalab Inc. after chamber surface neutralized by the soft x-ray photo ionizer.
[c]: see Carter et al. (2005).
[d]: measured after 8 hours of irradiation.

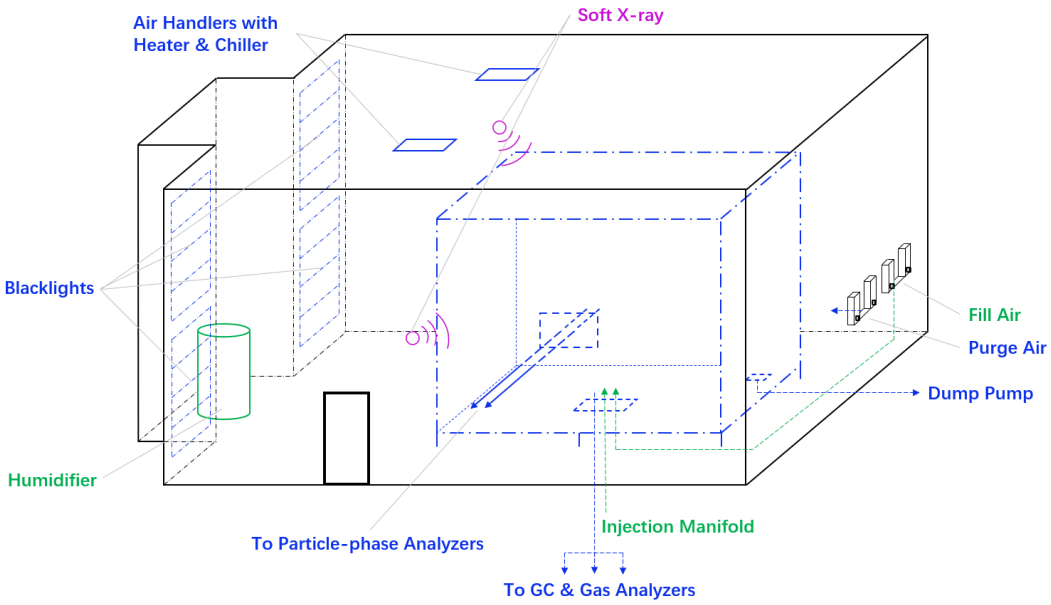

Figure 4-1. Schematic of the UCR new-generation 120-m^3 fix-volume chamber and enclosure.

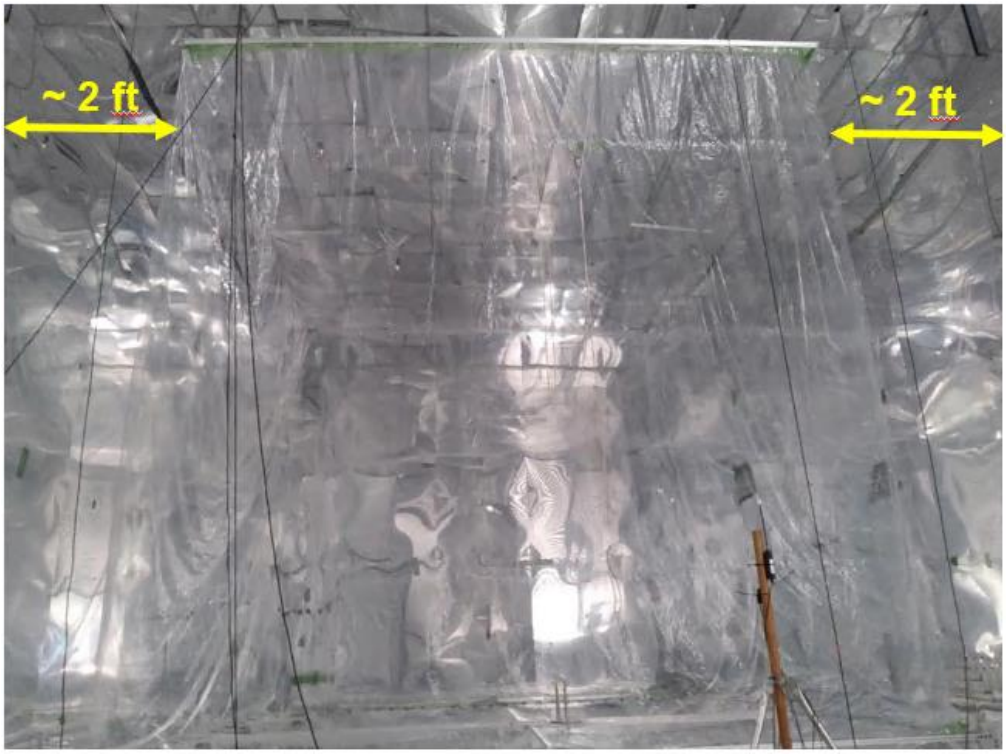

Figure 4-2. A picture of the real chamber. A distance of around 2 feet is kept between chamber walls and conductive aluminum enclosure walls.

From the previous chapters we concluded that the UCR collapsible chambers were significantly affected by electrostatic charges on chamber surfaces due to the surface material rubbing against each other between the dual chambers, conductive enclosure surfaces or rubber gloves (during chamber routine maintenances). Therefore, mitigations have been applied on the design of the new chamber. The new chamber is hung in the enclosure room, framed and supported by aluminum T-slot structures (80/20 Inc.) on its top and bottom sides. The structure feet touching the conductive aluminum enclosure grounds are isolated using Teflon mats ~ 3 mm thick. The shape of the new chamber is constrained by the frame structure and the chamber at a sufficient distance from the enclosure walls to prevent the chamber surface from rubbing against the conductive aluminum enclosure walls (Figure 4-2). The chamber wall materials also do not have the chance to rub against each other during the course of an experiment because of the use of a single chamber instead of the former dual chambers. When cleaning the chamber after an experiment, a simplified PID controlled process has been developed using the pressure differential between the chamber and the enclosure, where purified fill air is continuously flushed into the chamber while the dump pump is actively cycled on and off to maintain chamber shape. The chamber autonomous cleaning cycle normally lasts at least one day.

Additionally, despite the efforts to reduce the contact between chamber surfaces and known electrostatic sources, there are still occasions where chamber surface charge can accumulate, such as people walking around the chamber enclosure, chamber maintenance, etc. Therefore, three external Soft X-ray PhotoIonizers (Hamamatsu Photonics, Figure 4-3) are available to minimize the chamber surface charge prior to experiments. An Ultra Stable Surface Volt Meter (Model USSVM II, Alphalab Inc.) was used to test the Teflon surface voltages at different conditions (Table 4-2) and the photo ionizers demonstrated to minimize chamber surface charge.

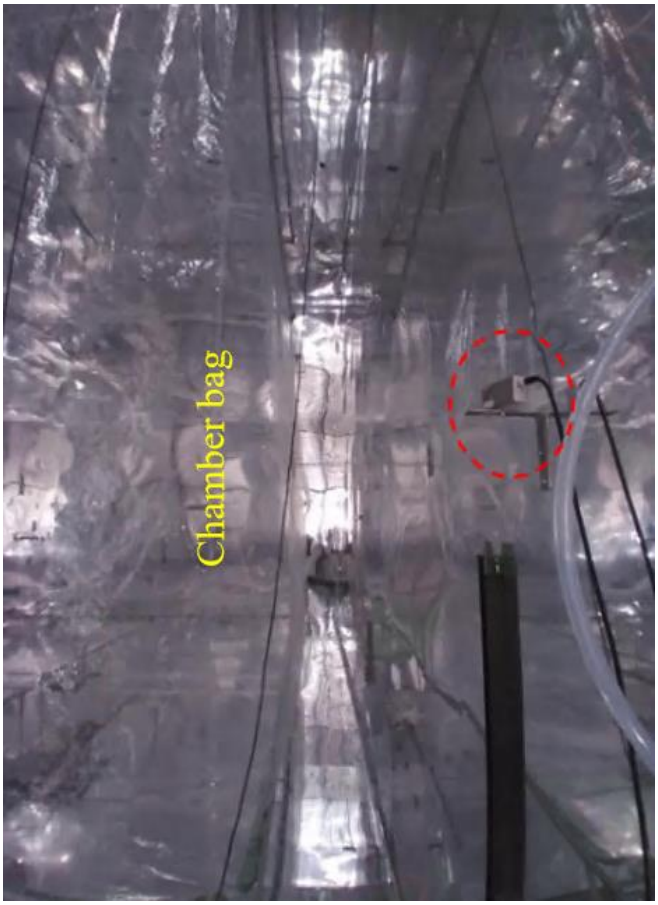

Figure 4-3. A picture of one of the soft x-ray photo ionizers deployed for eliminating chamber surface charge on the right-hand side of the chamber. The other ionizers are distributed on other sides of the chamber (Figure 3-2, Li 2022).

Table 4-2. Test results of surface voltages on chamber FEP surfaces or FEP films at different conditions.

Condition	Surface Voltage Readings (V)
Statically sit over-night	± 30 – 100 at places touching an aluminum sheet
	± 200 at places touching another FEP film
Gently rubbed by an aluminum sheet	± 3000
Gently rubbed with bare hands	± 10000
Treated by soft x-ray photo ionizers	± 10

4.2.2 Particle wall-loss characterization

4.2.2.1 Polydisperse and monodisperse experiments

Particle wall-loss behaviors in the UCR/CE-CERT new-generation fixed-volume chamber were characterized in this study using the monodisperse particle injection method, in order to evaluate size dependent wall loss and evaluate the significance of electrostatic effect for conditions where particle-particle coagulation is negligible. Polydisperse particle injection method commonly used by other chamber groups (e.g., Charan et al. 2018; Wang et al. 2018; Nah et al. 2017) was also used for some characterization experiments. Experiments (Table 4-3) were conducted at room temperature (~ 21°C) and ultra-low relative humidity (< 0.1%). Ammonium sulfate (Sigma-Aldrich, 99%, referred to as AS for later discussions) was nebulized to generate mono- and poly-dispersed seed particles. The experimental protocol for polydisperse particle injection experiments has been discussed in Section 2.2.1. A portable high-flow differential mobility analyzer (DMA) system, described by Xu and Collins (2021), was used to supply size-selected mono-dispersed particles (Figure 4-4). Monodisperse AS particles were generated by atomizing a 0.1 M aqueous AS solution with an atomizer (TSI Inc. Model 3076). The atomized particles were dried by directing them through a molecular sieve diffusion column. The dry AS particles were then classified ranging from 50 – 300 nm by the DMA column. The aerosol was brought to a steady state charge distribution before and after size classification by the DMA by using soft x-ray neutralizers. Double-charged particles during the injection of 200 – 300 nm particles were utilized and investigated for target particle sizes larger than 300 nm. Alternatively, diluted SOA particles with single peak mode and no measurable size shift during the course of the experiment were also used in some of the experiments.

Table 4-3. List of experiments used in this work to explore the size-dependent particle wall-loss patterns in UCR new-generation fixed-volume chamber.

Run Number	Dilution Rate (% per hour)	Particle Composition	Particle Size Investigated	Notes
2654	0.50[a]	Ammonium Sulfate	50 & 200 nm 73 nm[b]	Discussed in Section 4.3.2.
2656	0.50[a]	Ammonium Sulfate	100 & 300 nm 152 nm[b]	
2660	0.50[a]	Ammonium Sulfate	75 nm 112 nm[b]	
2662	0.50[a]	Ammonium Sulfate	50 & 250 nm 73 nm[b]	
2664	0.50[a]	Diluted SOA[c]	400 nm	
2669	1.00[a]	Ammonium Sulfate	50 & 200 nm 73 nm[b]	
2671	1.00[a]	Ammonium Sulfate	200 nm	
2672	1.00[a]	Ammonium Sulfate	152 & 240 nm 397 nm[b]	
2683	0.50[a]	Ammonium Sulfate	208 nm 340 nm[b]	
2708	0.50[a]	Diluted SOA[d]	350 nm	
2731	0.95	Ammonium Sulfate	50 & 200 nm 73 nm[b]	
2733	1.02	Ammonium Sulfate	50 & 215 nm 73 & 352 nm[b]	
2734	1.02	Ammonium Sulfate	75 & 250 nm 112 & 415 nm[b]	
2735	0.94; 0.49[d]	Ammonium Sulfate	100 & 250 nm 152 & 415 nm[b]	
2681	0.50[a]	Ammonium Sulfate	50 & 200 nm	Discussed in Section 4.3.1.
2715	0.54	Ammonium Sulfate	Polydisperse	Discussed in Section 4.3.4.
2724	0.78	Ammonium Sulfate	Polydisperse	
2759	1.70	Ammonium Sulfate	Polydisperse	

[a]: Based on the best estimation from adjacent experiments whose dilution data was available.

[b]: The investigated double-charged particle peak size(s).

[c]: Diluted SOA with single peak mode and no measurable size drift during the course of the experiment.

[d]: Long experiments, duration of each measurement was > 8 hr, with manual dilution process in between.

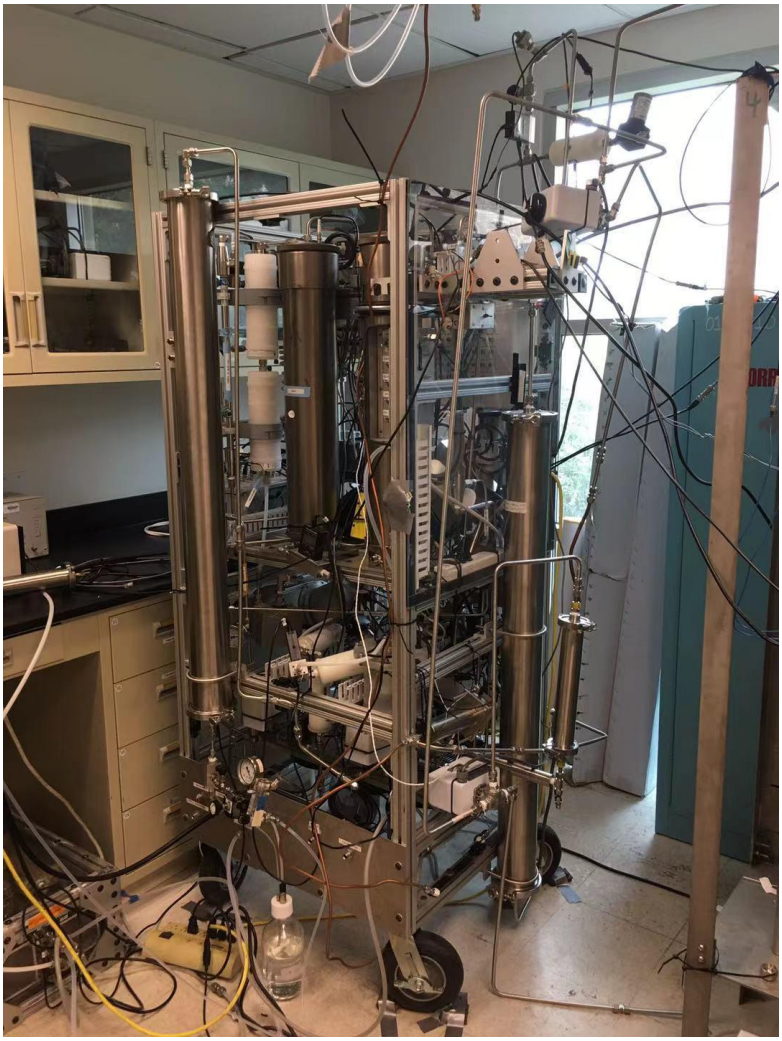

Figure 4-4. The portable high-flow DMA system with atomizer (Xu and Collins 2021).

4.2.2.2 Particle measurement and wall-loss rate corrections

As was discussed previously in detail (Section 2.2.3), a dual-SMPS system was used to study the decay patterns of the positively-charged particles and total particles during the experiments. The particle wall-loss behaviors of positively-charged particles were measured by the SMPS equipped with a negative HV supply (BERTAN 602C-100N) but without a neutralizer prior to the DMA entrance. The particle wall-loss behaviors of total particles were measured by a standard SMPS with an ^{85}Kr neutralizer prior to the DMA entrance. Due to the existence of chamber dilution in the new system, the dynamic size-dependent particle wall-loss rates were calculated by Equation 3-1 with dilution-corrected particle number concentrations using 15 adjacent SMPS timesteps to minimize step-wise uncertainties. The size-dependent particle wall-loss rates were then derived from averaging the dynamic rate constants over time.

Next, the collected size-dependent particle wall-loss rates were corrected for potential bias caused by same-mobility but multiple-charged particles. Figure 4-5 shows a stable particle size distribution output from the high-flow DMA system. Particles were assumed to reach Fuchs' charge equilibrium before entering the DMA system, thus for a given selected mobility size, a portion of multiple-charged particles might also pass through. The DMA-output particles reached the Fuchs' charge equilibrium again by passing through the secondary neutralizer, but still a small fraction can be left as multi-charged. This effect can be negligible in most of the cases due to the two-phase neutralizing, but it might be relatively non-negligible when the DMA selects e.g., 75 nm mobility-equivalent particles, as the initial particle sources for 75 nm particles is much less abundant compared to particles at 113 nm (the same-mobility but double-charged particle physical size). Regardless, care has been taken correcting for the same-mobility multiple-charged particles due to their different physical sizes resulting in different wall-loss rates.

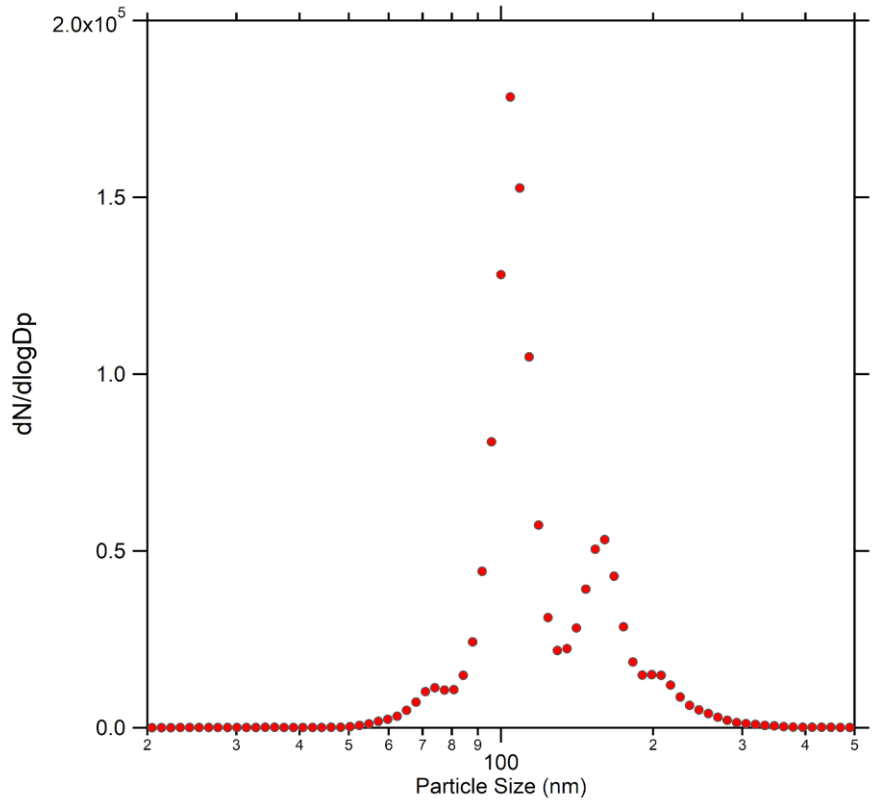

Figure 4-5. The atomizer output particle size distribution prior to the entrance of the high-flow DMA column.

4.2.3 Three-component size-dependent particle wall-loss correction method

The three-component size-dependent particle wall-loss correction method (referred to in this work as the Size-dependent method) based on the MATLAB platform (referred to in this work as the script) has been developed as a part of evaluation of the current day-to-day variability on particle wall-loss and a potential alternative method to more accurately characterize size dependent particle wall-loss rates. Table 4-4 summarizes the different particle wall-loss correction methods that are evaluated by the script. It is noted that although the methods from the previous chapter remain the same name here, dilution loss is exclusively corrected when applying these methods for the UCR new-generation fixed-volume chamber. The overall logic diagram of the script is displayed in Figure 4-6 and the size-dependent particle loss correction schematics is displayed in Figure 4-7. The three components include chamber dilution, particle-particle coagulation and particle-wall deposition. The dilution of the chamber is quantified by injecting an inert tracer compound (usually perfluorohexane, PFH; sometimes perfluorobenzene, PFB) to the chamber prior to starting an experiment and measuring the concentration time series using an GC-FID. In normal mode of the script, the particle-particle coagulation is still assumed to be volume-conserved (no total volume change before or after coagulation) – the total volumes of the coagulated dimers that become too large to be measured by the current SMPS range are still accounted for. A size-dependent particle wall-loss curve generated from the series of monodisperse particle injection characterization experiments is applied to correct the loss of particle numbers and volumes in each SMPS size bin. Therefore, the total particle volume correction, which eventually leads to the total particle mass correction, can be summarized as:

$$\Delta V(t) = \Delta V_{dilution}(t) + \Delta V_{coagulation}(t) + \Delta V_{particle\ wall-loss}(t) \quad \text{(Equation 4-1)}$$

Table 4-4. Different particle wall-loss methods evaluated by the script.

Method Name	Calculation Source	Time-resolved	Coagulation-corrected	Dilution-corrected	Size-dependent
SB-Fit	Total number decay during the whole fitting time	No	No	Yes	No
CcDB-Fit	Local total number decay	Yes	Yes	Yes	No
Size-dependent	Number decay during the whole fitting time	No	---[a]	Yes	Yes

[a]: see Section 4.2.3.4.

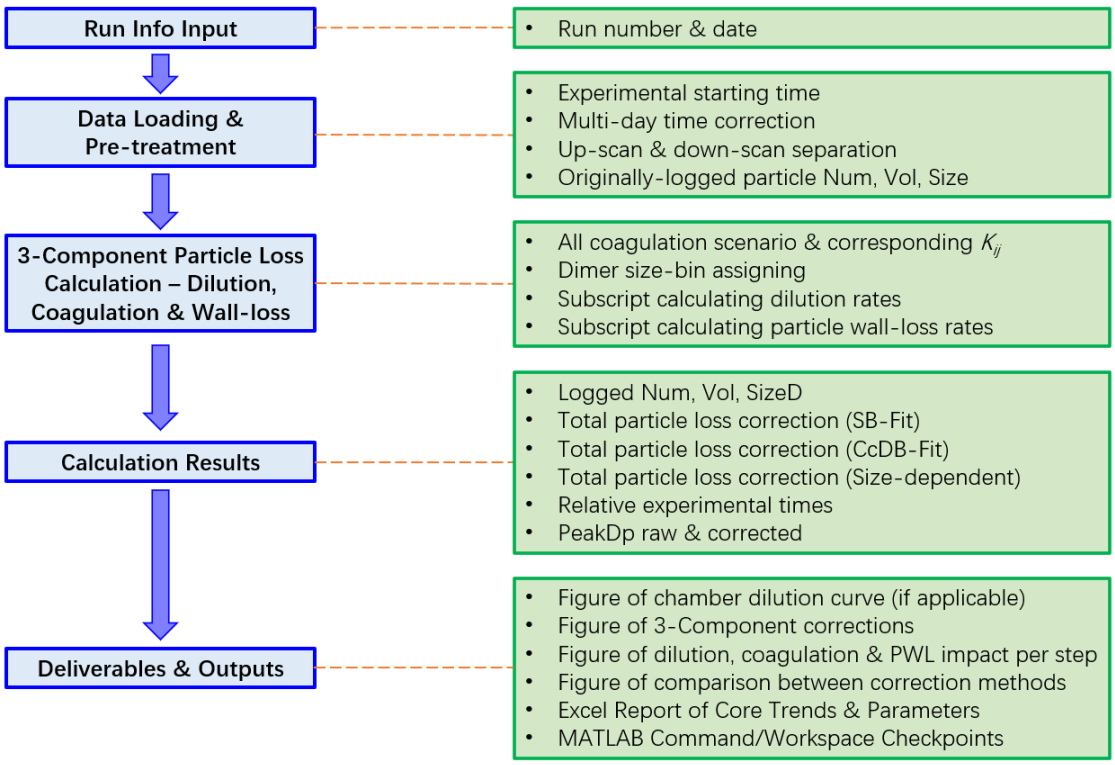

Figure 4-6. The overall logic diagram of the script.

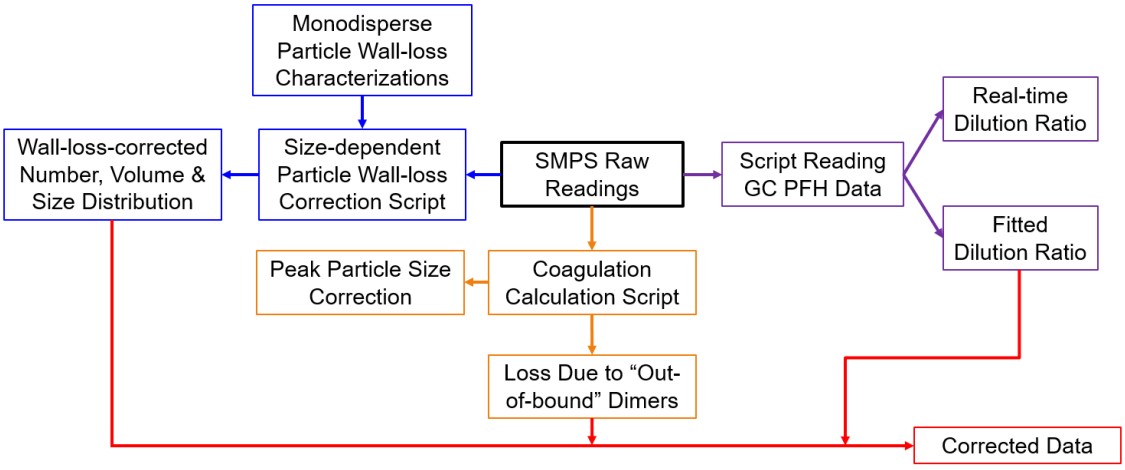

Figure 4-7. Schematic diagram of the three-component size-dependent particle wall-loss correction method.

4.2.3.1 Data loading and pre-treating

The script performs calculations based on loaded data and manual inputs from users in the command window through interactive questions and answers. Particle number concentration, volume concentration and size distribution are measured by 3 alternate custom SMPS instruments, named West SMPS, East SMPS and Black SMPS, respectively. Similar LabVIEW programs (Figure 7-2 and Figure 7-5) were developed to control the instruments and output raw files in the same format. The developed particle loss correction script uses the raw .txt files generated by the selected SMPS, thus SMPS timestamps, number concentrations, volume concentrations and size distribution are all loaded. The collected SMPS timestamps have a limited format, thus the script conducted a further correction for AM/PM notation and for multiple experimental days. Relative experimental time matrix is further prepared upon the manual input of experimental starting time in the command window. The current SMPS scanning scheme includes up-scan (high-voltage spans from low to high) and down-scan (high-voltage spans back), and the current version of script separates and evaluates only up-scan data.

4.2.3.2 Dilution calculation

Initial tracer compound concentration values as a function of GC measurement time intervals are collected and the data after the experimental starting time are selected to fit (second order polynomial) for a wider range of timestamps that are compatible with the SMPS timesteps (Figure 4-8). In order to ensure the quality of the fit, options are provided whether or not to tune the first three fitted data points by the prompt questions in the MATLAB command window. As the result, fitted tracer concentrations are assigned to each SMPS timestep. Then, the dilution ratios between adjacent steps are calculated using (Equation 4-2):

$$dil(i) = -\frac{[Trc]_i - [Trc]_{i-1}}{[Trc]_i} \quad \text{(Equation 4-2)}$$

where $[Trc]_i$ is the fitted tracer concentration at SMPS timestep i and $[Trc]_{i-1}$ is the fitted tracer concentration before the current step. The step-wise number/volume dilution in each SMPS size bin are then calculated by multiplying the raw data with the stepwise dilution ratios. Additionally, a brief estimation of overall total chamber dilution rate (in units of percent per hour) is calculated from the tracer concentrations at experimental time zero and end. This value can be used for the script to provide the best available estimation of particle dilution loss for an adjacent experiment where tracer concentrations are not available for whatever reasons.

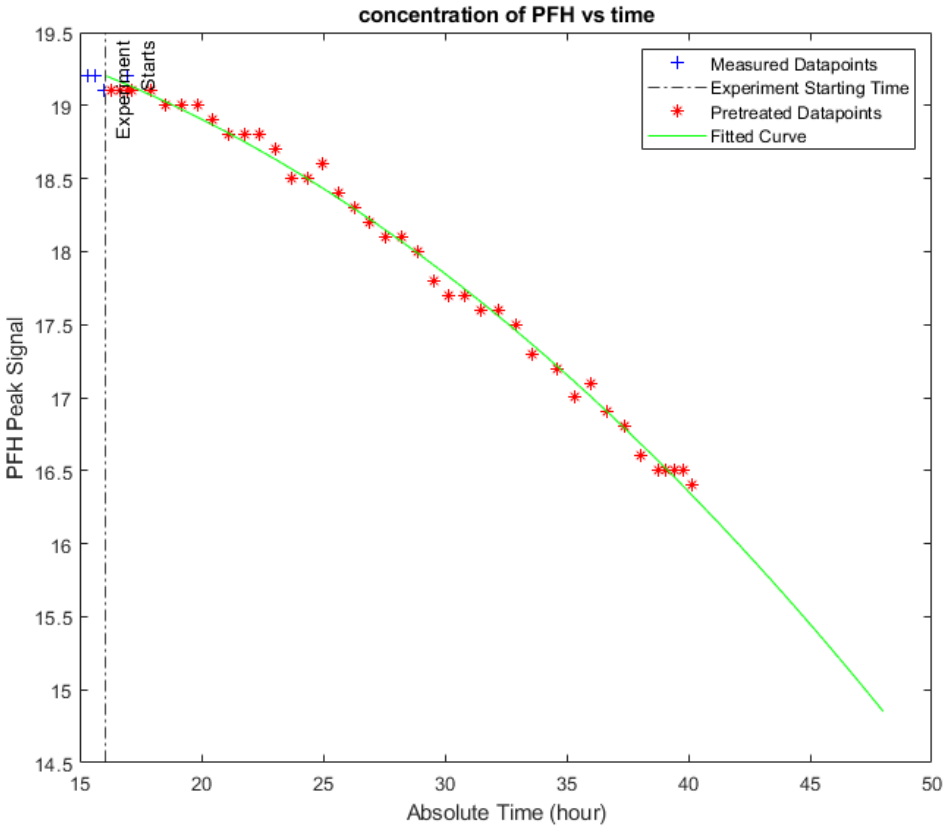

Figure 4-8. Example of the tracer concentration fitting outcome generated by the script for an experiment.

4.2.3.3 Coagulation calculation

The calculation for particle-particle coagulation has been discussed in detail in Section 3.2.3. The coagulation coefficients, K_{ij}, are derived from Seinfeld and Pandis (2016) and a coagulation coefficient multiplier, which is set as 1 by default, is applied to all K_{ij} values, providing possibilities to conduct sensitivity evaluation of coagulation coefficients when needed.

The shape factor χ, defined as the ratio of the electrical mobility of a volume-equivalent sphere particle to the electrical mobility of the particle itself (Hinds 1999; Dahneke 1973; Kasper 1982), is set with a value of 1 by default, representing the assumption of conserved-volume after coagulation. The total volume concentrations of coagulated dimer particles whose sizes are beyond the upper limit of the SMPS detection range are collected and accumulated as the coagulation particle loss (referred to in this work as coagulation out-of-bound), although this value is usually very small. During the course of an experiment, particle size change is mainly due to 1) particle growing and aging, caused by nucleation burst and the followed-up gas-particle partitioning and 2) particle-particle coagulation. Since the coagulation calculation is based on each size bin, the coagulation-corrected particle size distribution as a function of experimental time, reflecting the particle growth assuming no coagulation, is also provided for further study purposes.

4.2.3.4 Particle wall-loss calculation

For the Size-dependent method, the size-dependent particle wall-loss pattern for UCR fixed-volume chamber was obtained from the series of monodisperse wall-loss characterization experiments discussed in Section 4.2.2. The data collected was then fitted by Crump and Seinfeld (1981) theory based on Corner and Pendlebury (1951) results for a cubic chamber with a side length of L:

$$\beta = \frac{1}{L}\left[\frac{8\sqrt{k_e D}}{\pi} + v_s \coth\left(\frac{\pi v_s}{4\sqrt{k_e D}}\right)\right] \quad \text{(Equation 4-3)}$$

where β is the size-dependent particle wall-loss rate, k_e is the eddy-diffusion coefficient of the chamber, D refers to the particle Brownian diffusivity and v_s represents the terminal particle settling velocity. For a given particle size of D_p, D and v_s are further calculated by:

$$D = \frac{kTCc}{3\pi\mu D_p} \quad \text{(Equation 4-4)}$$

$$v_s = \frac{{D_p}^2 \rho g Cc}{18\mu} \quad \text{(Equation 4-5)}$$

$$Cc = 1 + \frac{2\lambda}{D_p}\left[1.257 + 0.4exp\frac{-1.1D_p}{2\lambda}\right] \quad \text{(Equation 4-6)}$$

where k is the Boltzmann constant, T is the temperature, μ is the viscosity of air, Cc is the Cunningham slip-correction factor, ρ is the density of the particle, g is the gravitational constant and λ is the mean free path of air.

When fitting the theoretical curve, the best-fit k_e value was found and applied to calculate the theoretical size-dependent particle wall-loss rates for the chamber. These size-dependent particle wall-loss rates are then assigned to the corresponding SMPS size bins to correct for particle wall-loss throughout the experiment within each size bin. It is noted that the fitted size-dependent pattern is assumed to represent the averaged performance of the current chamber, where the oscillation, change or shift of particle wall-loss rates are neglected until the next round of investigation or characterization. Since the size-dependent particle wall-loss rates are obtained by independent monodisperse characterization experiment series, the application of these rates and the correction of particle wall-loss for a real SOA experiment is independent to the coagulation correction for the SOA experiment itself (superscript [a] Table 4-4).

4.2.3.5 Script outputs and deliverables

The script generates output files as listed in Table 4-5. Core parameters and time series from the processed experiment are clustered in the Excel file, as illustrated in Table 4-6 and Table 4-7. Details of items listed in these tables were previously discussed in Section 3.2.5. The script is extensively organized and commented for future generations of users to utilize, explore and develop other perspectives analyzing the SMPS data. For example, all coagulation parameters,

such as coagulated dimer size factor and all coagulation kernels can be tuned for sensitivity analysis in evaluation mode; size-dependent particle wall-loss rates can be loaded from other data sources, etc. The script is also designed to take care of fragmented SMPS raw files. Fragmented raw files occasionally originate during operation of SMPS due to pausing the acquisition program for instrument failure or users adjusting the scanning parameters. The fragmentation results in multiple batches of raw files collected for a single experiment where the time gap of SMPS can reach tens of minutes. The script treats each individual fragment for particle wall-loss and then combines these results using a user-friendly interaction design via the MATLAB command window. In short, this script is a powerful tool to analyze the evolution of particle number concentrations, volume concentrations and size distribution based on measured SMPS data from an experiment using the UCR new-generation fixed-volume chamber.

Table 4-5. Deliverables of the script.

Deliverable Names	Content	File Type	Data Source
Dilution Fitting Curve	Fitting of tracer compound concentration timeseries based on GC measurement	Figure	Single experiment
Size-dependent Output	Clustered time series of corrected particle number & volume from dilution, coagulation and size-dependent wall-deposition		
PWL Correction Comparison	Clustered time series of corrected particle number & volume with all analyzed correction methods		
Loss Impact	Percentage of dilution, coagulation and wall-deposition to raw particle numbers		
Individual Experiment Summary	Statistics of core parameters and time series	Excel sheet	

Table 4-6. Parameters recorded in Excel sheet output – Individual Experiment Summary.

Category	Parameter Item
General information	Run number
	Date (the last modified date on raw .txt file)
	Relative experimental time (hour)
	Relative experimental time (day)
Particle losses (for multiple fragments of raw SMPS files use)	Total number loss due to dilution at end time (cm^{-3})
	Total number loss due to coagulation at end time (cm^{-3})
	Total number loss due to PWL at end time (SB-Fit, cm^{-3})
	Total number loss due to PWL at end time (CcDB-Fit, cm^{-3})
	Total number loss due to PWL at end time (Size-dependent, cm^{-3})
	Total volume loss due to dilution at end time (um^3 cm^{-3})
	Total volume loss due to coagulation at end time (um^3 cm^{-3})
	Total volume loss due to PWL at end time (SB-Fit, um^3 cm^{-3})
	Total volume loss due to PWL at end time (CcDB-Fit, um^3 cm^{-3})
	Total volume loss due to PWL at end time (Size-dependent, um^3 cm^{-3})
Other parameters	Coagulation dimer viscosity shape factor
	Coagulation kernel tuning factor
	Coagulation out-of-bound total volume (um^3 cm^{-3})
	Particle wall-loss rate, SB-Fit (day^{-1})
	Averaged particle wall-loss rate, CcDB-Fit (day^{-1})

Table 4-7. Time series recorded in Excel sheet output – Individual Experiment Summary.

Category	Time Series Item
Timestamps	Absolute time in string format
	Absolute time in numerical format (day)
	Relative time in numerical format (day)
Total number	Raw number, logged (cm^{-3})
	Number loss, dilution (cm^{-3})
	Number loss, coagulation (cm^{-3})
	Number loss, particle wall-loss (Size-dependent, cm^{-3})
	Number loss, particle wall-loss (SB-Fit, cm^{-3})
	Number loss, particle wall-loss (CcDB-Fit, cm^{-3})
	Corrected total number, Size-dependent (cm^{-3})
	Corrected total number, SB-Fit (cm^{-3})
	Corrected total number, CcDB-Fit (cm^{-3})
Total volume	Raw volume, logged ($um^3\ cm^{-3}$)
	Volume loss, dilution ($um^3\ cm^{-3}$)
	Volume loss, coagulation out-of-bound ($um^3\ cm^{-3}$)
	Volume loss, particle wall-loss (Size-dependent, $um^3\ cm^{-3}$)
	Volume loss, particle wall-loss (SB-Fit, $um^3\ cm^{-3}$)
	Volume loss, particle wall-loss (CcDB-Fit, $um^3\ cm^{-3}$)
	Corrected total volume, Size-dependent ($um^3\ cm^{-3}$)
	Corrected total volume, SB-Fit ($um^3\ cm^{-3}$)
	Corrected total volume, CcDB-Fit ($um^3\ cm^{-3}$)
	Corrected total volume, Omega = 1 (Size-dependent, $um^3\ cm^{-3}$)
	Corrected total volume, Omega = 1 (CcDB-Fit, $um^3\ cm^{-3}$)
Others	Particle wall-loss rate, CcDB-Fit (day^{-1})
	PeakDp, raw (nm)
	PeakDp, Coagulation-corrected (nm)
	PeakDp, Coagulation-corrected, size-dependent wall-loss corrected (nm)
	Dilution percentage (%)
	Coagulation percentage (%)
	Total particle wall-loss percentage (Size-dependent, %)
	Total particle wall-loss percentage (CcDB-Fit, %)

4.3 Results and Discussion

4.3.1 Performance of the new chamber

Overall particle wall-loss performance: Table 4-8 summarizes two pairs of experiments designed with identical injection concentration but using different generations of chambers. The particle wall-loss correction calculations using both the traditional SB-Fit method and the updated CcDB-Fit method were performed; correction results from the latter method are displayed (Figure 4-9). The particle volume wall-loss correction is approximately one tenth as large after the migration of the chamber design. The much lower particle losses in UCR new fixed-volume chamber offer several advantages, such as 1) longer experiment duration – lower particle losses allow for longer maximum experimental durations, providing opportunities to study gas-particle systems where the completion of chemistry and gas-particle partitioning exceeds the duration limit of the previous chamber; 2) improved correction accuracy and experimental reproducibility and 3) opportunities to explore vapor wall-loss, which might be underrepresented in the previous chambers when particle losses were relatively higher.

Table 4-8. Experiments with same designed initial conditions in different generations of chambers.

Run Number	Target	Chamber	Duration (hr)
1843A	*m*-xylene (80 ppb) + NO (50 ppb)	Previous Collapsible	8.4
2688	*m*-xylene (80 ppb) + NO (50 ppb)	New Fixed-volume	12.7
1860B	*m*-xylene (120 ppb) + H_2O_2 (1 ppm)	Previous Collapsible	9.6
2619	*m*-xylene (120 ppb) + H_2O_2 (1 ppm)	New Fixed-volume	9.2

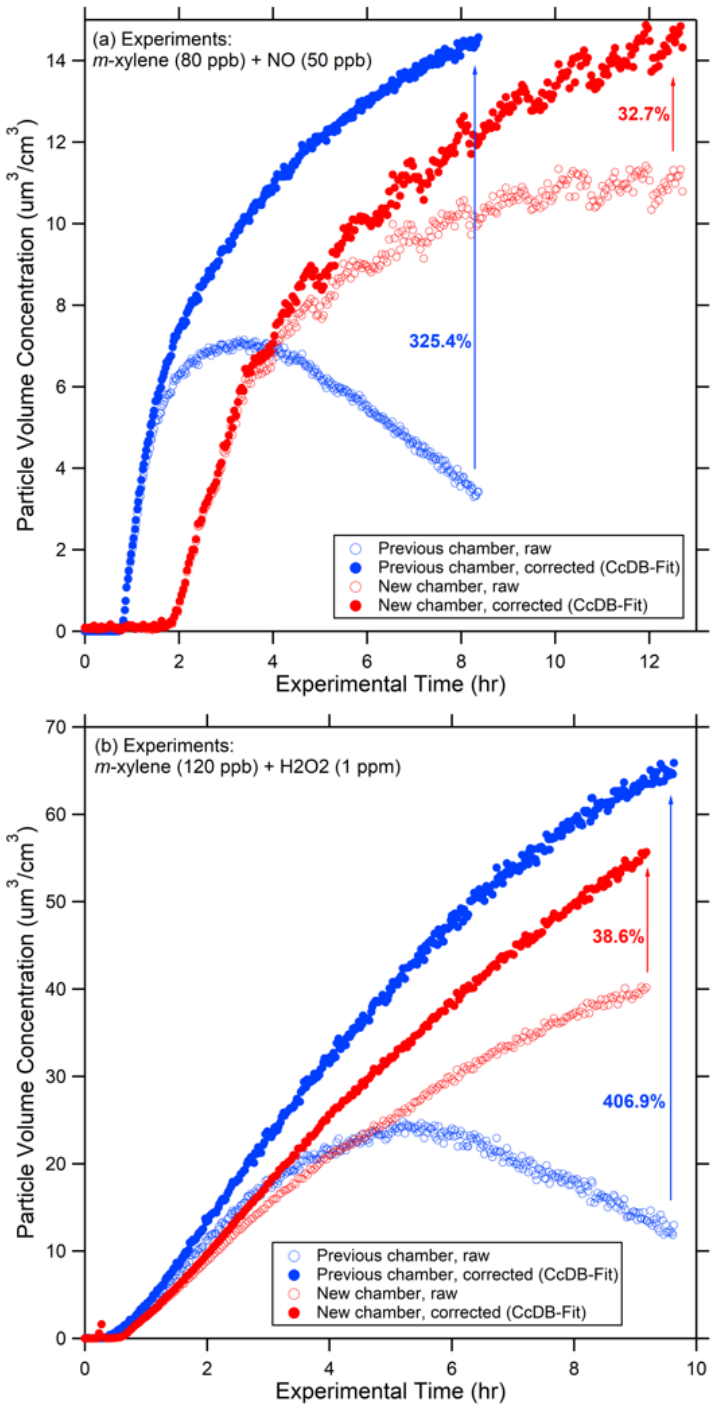

Figure 4-9. Raw and wall-loss corrected particle volume time series for **(a)** *m*-xylene (80 ppb) + NO (50 ppb) and **(b)** *m*-xylene (120 ppb) + H_2O_2 (1 ppm) experiments. Blue trends represent the experiments conducted in the previous-generation UCR collapsible chambers and red trends represent the experiments using the new fixed-volume chamber. Hollow circles represent SMPS-measured volume and solid circles represent corrected volume using the CcDB-Fit method.

The effect of electrostatic surface charges: Similar to the approach discussed in Section 2.3.1, the effect of electrostatic surface charges on the new-generation fixed-volume chamber has been explored by measuring the decay patterns of total particles as well as the positively-charged portion within. The chamber surfaces were first charged by rubbing with gloves and clean towels to simulate the charged condition from previous-generation collapsible chambers. Two typical monodisperse particle sizes (50 nm and 200 nm) were injected to the chamber, measured by the dual-SMPS setup, where one of the systems was not equipped with a neutralizer. After 10 hours of particle decay measurement, the chamber was neutralized using the external soft x-ray photo ionizers, and then particles were replenished with a second monodisperse injection. Figure 4-10 illustrates the normalized particle decay patterns for the selected particle sizes. As expected, particle wall-loss rates for both sizes of particles were significantly enhanced when the chamber surfaces were charged. Also, as discussed in Sections 2.3.1 and 2.3.2, under the condition of charged chamber surfaces, positively-charged 50 nm particles decayed much faster than total particles in the early period before experiencing kinetic charging limitation. The reproduced result further supports the earlier explanations of particle wall-loss behaviors in a charged chamber. Additionally, under the condition of neutralized chamber surfaces, which is also the normal charging status of the UCR fixed-volume chamber during current experiments, preferential loss of charged particles was not observed. This illustrates that the updated chamber design minimizes electrostatic-induced particle wall loss and day-to-day variability.

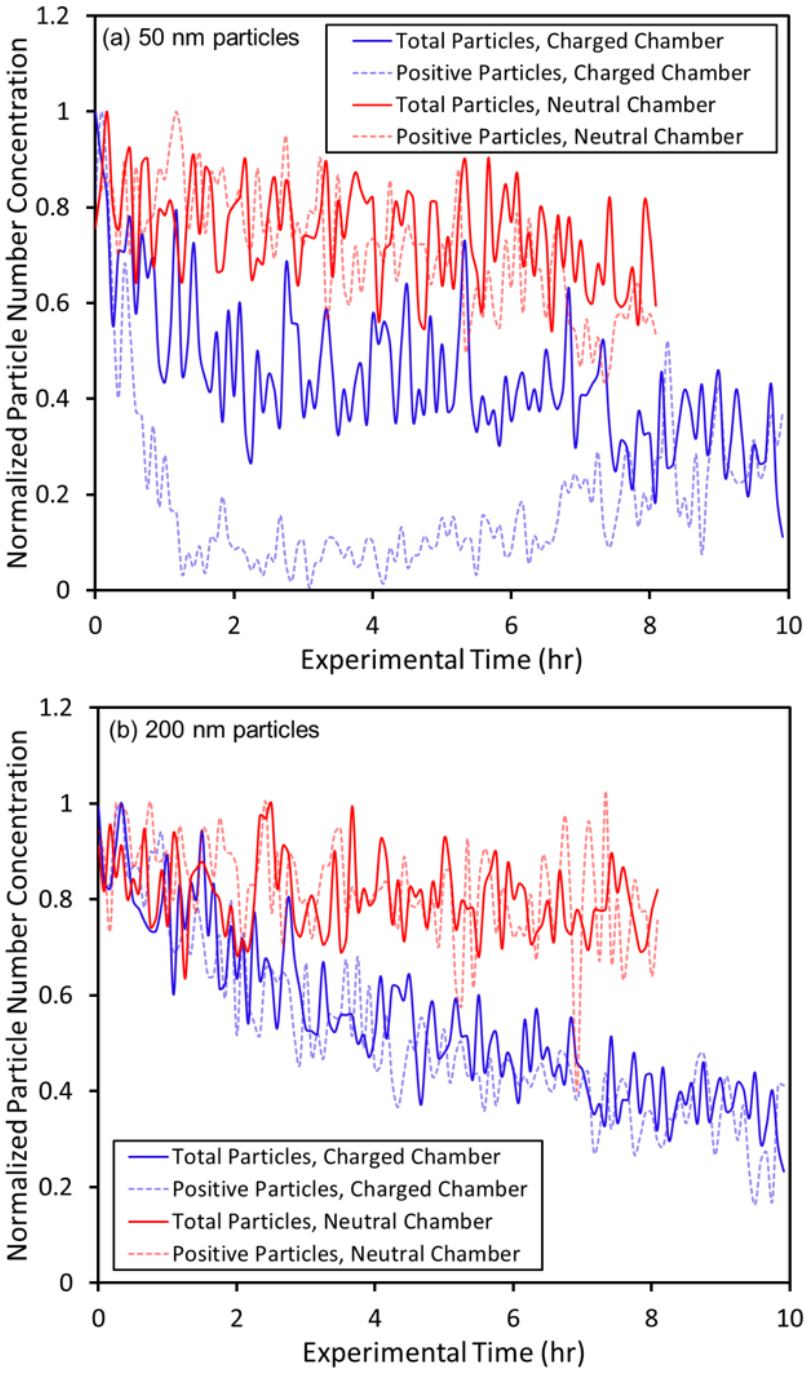

Figure 4-10. Decay of normalized particle number concentrations for **(a)** 50 nm particles and **(b)** 200 nm particles in the new fixed-volume chamber (run No. 2681). Blue trends represent the particle decay patterns when the chamber surfaces were charged and red trends represent the particle decay patterns when the chamber surfaces were neutralized by the external soft x-ray photo ionizers. Solid curves represent the total particles measured by normal SMPS and dashed curves represent the positively-charged particles measured by SMPS without a neutralizer.

4.3.2 Size-dependent particle wall-loss patterns

Measurements of coagulation-free particle wall-loss behaviors of select mobility sizes were obtained from monodisperse seed particle decay or diluted single-mode SOA decay experiments. The obtained size-dependent decay rates were corrected for chamber dilution and double-charged particles and are shown in Figure 4-11. The electrostatic effect on particle wall-loss is assumed to be negligible when fitting the collected experimental data using the Crump and Seinfeld (1981) theory. The best-fit of k_e for UCR fixed-volume chamber is 0.062 s^{-1} when the cube side length L was set to 4.93 m. The variance of experimentally obtained particle wall-loss rates might be attributed to variable particle convection conditions within the chamber due to: 1) the use of external air handlers – the purpose is to adjust temperature better for the huge chamber and enclosure, but air handlers also create air flow towards the outside chamber surfaces; 2) different chamber starting pressures – the starting differential pressure varied from 0.012 to 0.018 inH_2O, resulting in slightly different initial chamber geometry; and 3) the application of constant make-up air flows into the chamber to control the dilution ratio during some of the experiments. Sensitivity of particle wall-loss with respect to $k_e$was evaluated using upper-bound and lower-bound k_e values of 0.12 s^{-1} and 0.02 s^{-1}, respectively, for an example SOA experiment (run No. 2747, a-pinene + NO_x). The corrected particle volume timeseries using the Size-dependent correction method with best-fit, upper-bound and lower-bound particle wall-loss patterns are shown in Figure 4-12. The bias between the best-fit and upper-bound correction increases with experimental time, with a maximum value of 4.4% after 24 hours; the same trend and maximum bias value are also observed between the best-fit and lower-bound correction. Figure 4-13 shows the components of particle volume loss correction using the Size-dependent method for experiment No. 2747. As illustrated in Figure 4-13, the particle volume loss due to chamber

dilution is the same magnitude as volume loss due to particle wall-loss. It is noted that particle volume loss due to coagulation out-of-bound is very small and can typically be neglected.

The measured particle wall-loss rates for the new-generation UCR fixed-volume chambers are lower than most of the recently reported environmental chamber facilities and are much lower than the previous-generation UCR collapsible chambers (Figure 4-14). Compared to the previous-generation collapsible chambers, the UCR new particle wall-loss rates are more sensitive to particle sizes, where the highest decay rate in typical SMPS range (1.3 day^{-1}, 30 nm) is ~ 5 times higher than the lowest rate (0.25 day^{-1}, ~ 250 nm). As expected from the discussion in Chapter 2.3.4, the "spoon shape" indicator is observed for the new pattern, indicating the insignificant impact of electrostatic surface charges. Now that the electrostatic effect is minimized, the much-larger UCR chamber has much lower losses than other smaller chambers that report negligible electrostatic effects (e.g., Caltech new 19-m^3 chamber, Charan et al. 2018).

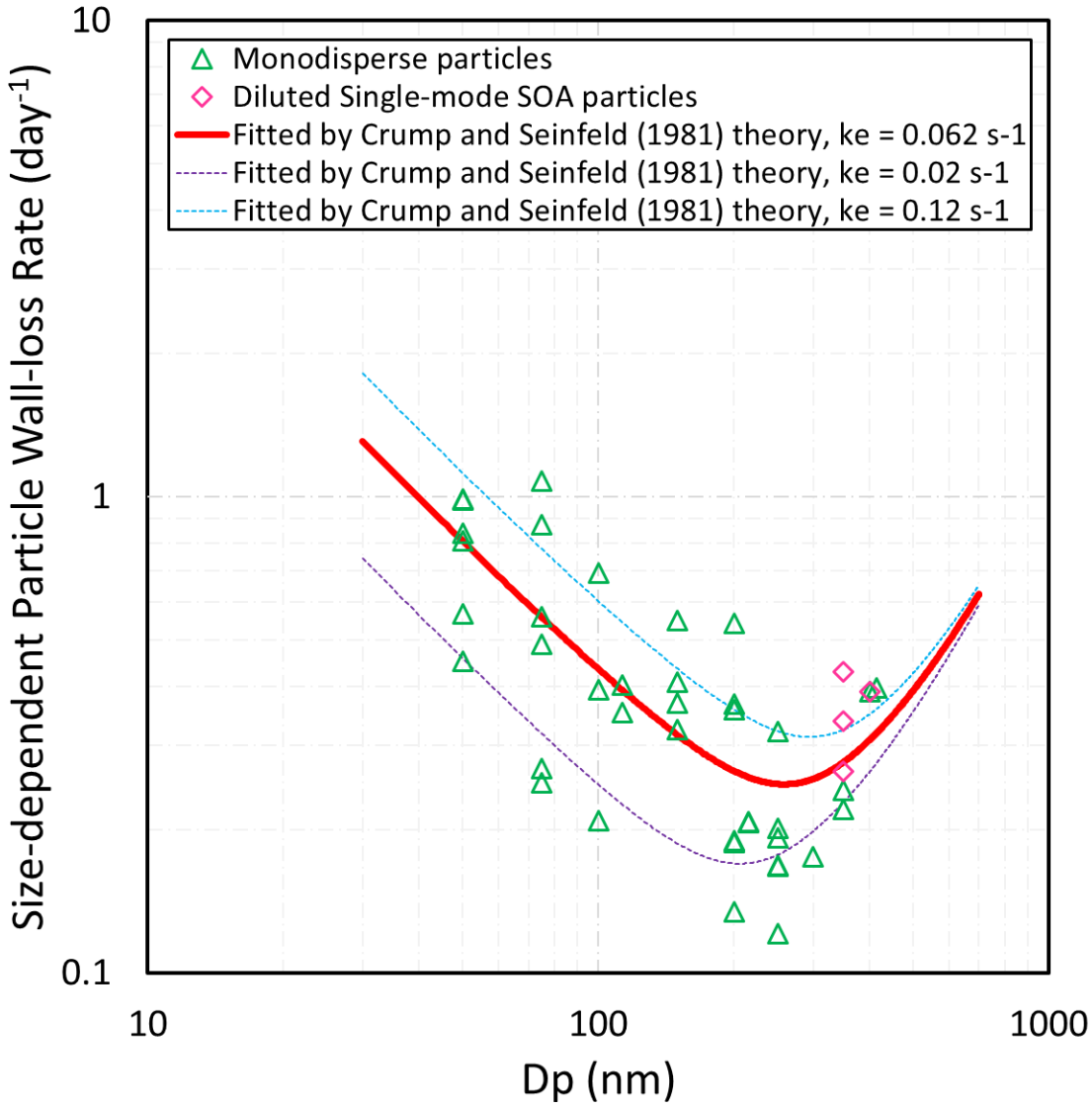

Figure 4-11. Size-dependent coagulation-free particle wall-loss rates collected from experiments. Green markers represent data from monodisperse seed injection experiments. Pink markers represent data from diluted SOA particles with single peak mode without measurable size drift. Red curve represents the optimal fitting from the experimental data using Crump and Seinfeld (1981) theory, where k_e = 0.062 s^{-1}. Purple curve represents the estimated lower bound, where k_e = 0.02 s^{-1}. Blue curve represents the estimated upper bound, where k_e = 0.12 s^{-1}. The size range of the fitted curve is from 30 nm to 700 nm.

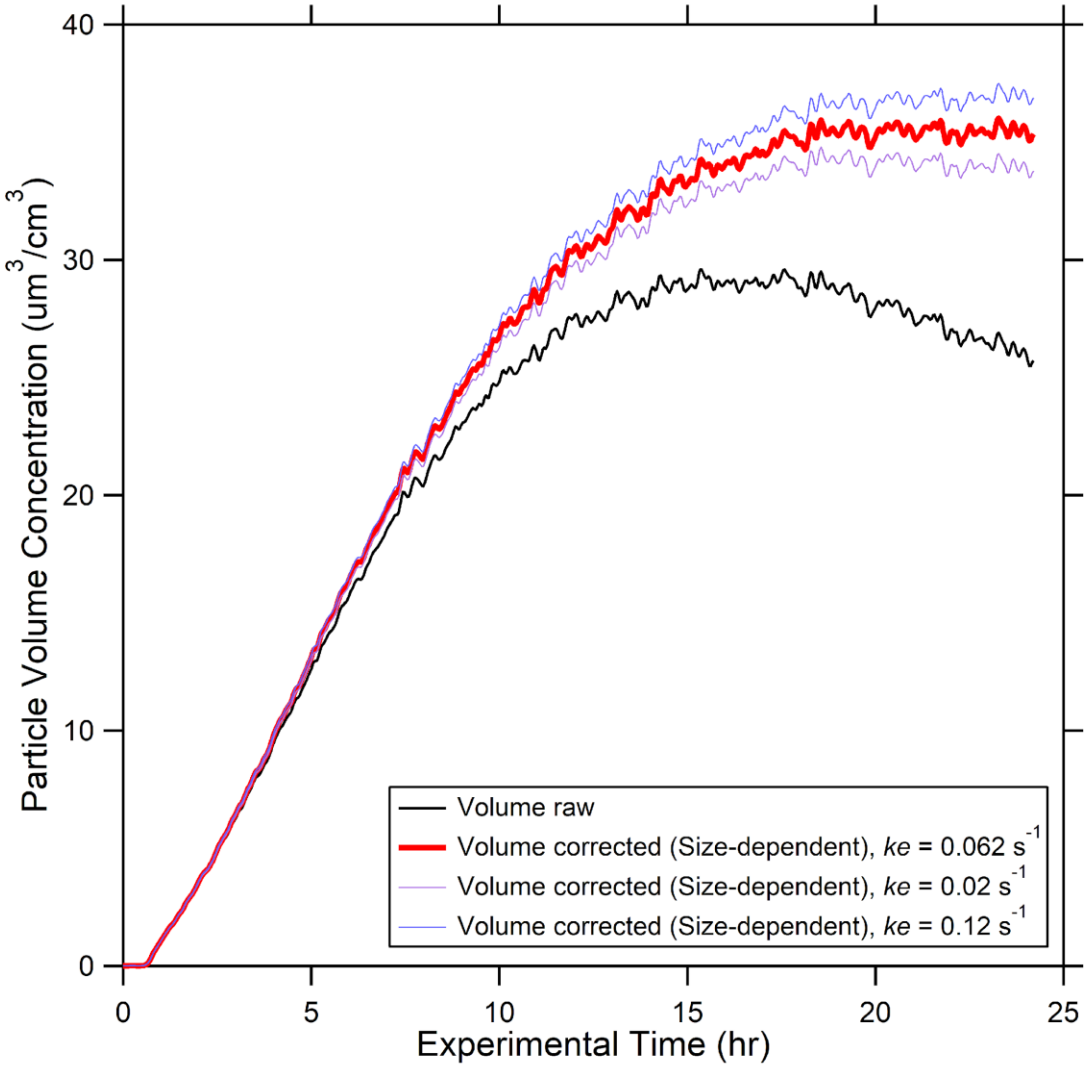

Figure 4-12. Corrected particle volume concentration timeseries from run No. 2747 using the Size-dependent correction method and applying different k_e. Black curve represents uncorrected volume concentrations, red curve represents the corrected values with the optimal fit (k_e=0.062 s^{-1}), pink curve represents the corrected values with the lower-bound fit (k_e=0.02 s^{-1}) and blue curve represents the corrected values with the upper-bound fit (k_e=0.12 s^{-1}).

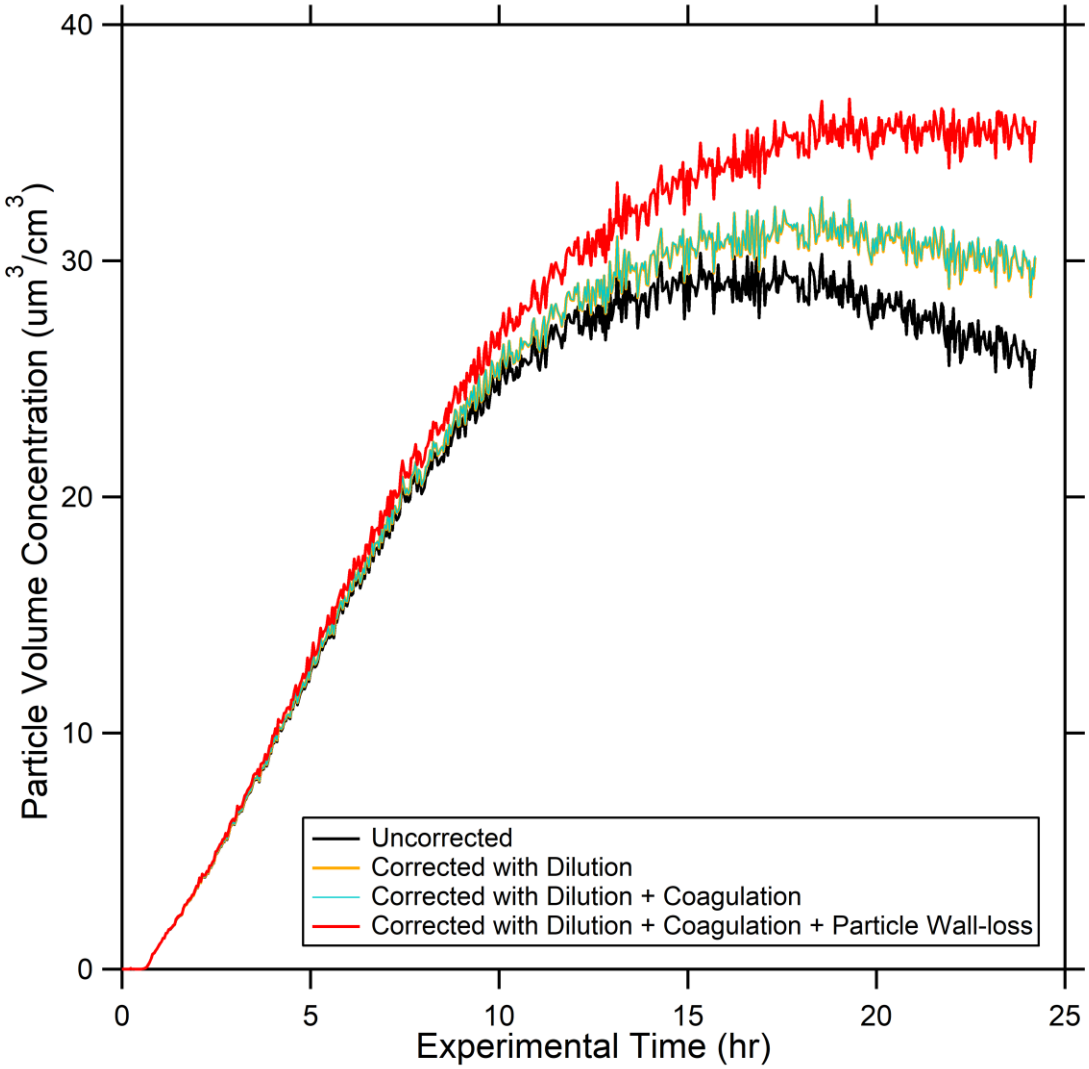

Figure 4-13. Break-down of different components of corrected particle volume time series for run No. 2747 using the Size-dependent method. Black curve represents uncorrected particle volume concentrations; orange curve represents particle volume concentrations corrected with dilution; teal curve, which is almost overlapped with orange curve, represents volume concentrations corrected with dilution as well as coagulation out-of-bound; red curve represents the final corrected particle volume concentrations, which additionally includes correction for particle wall-loss using k_e = 0.062 s^{-1}.

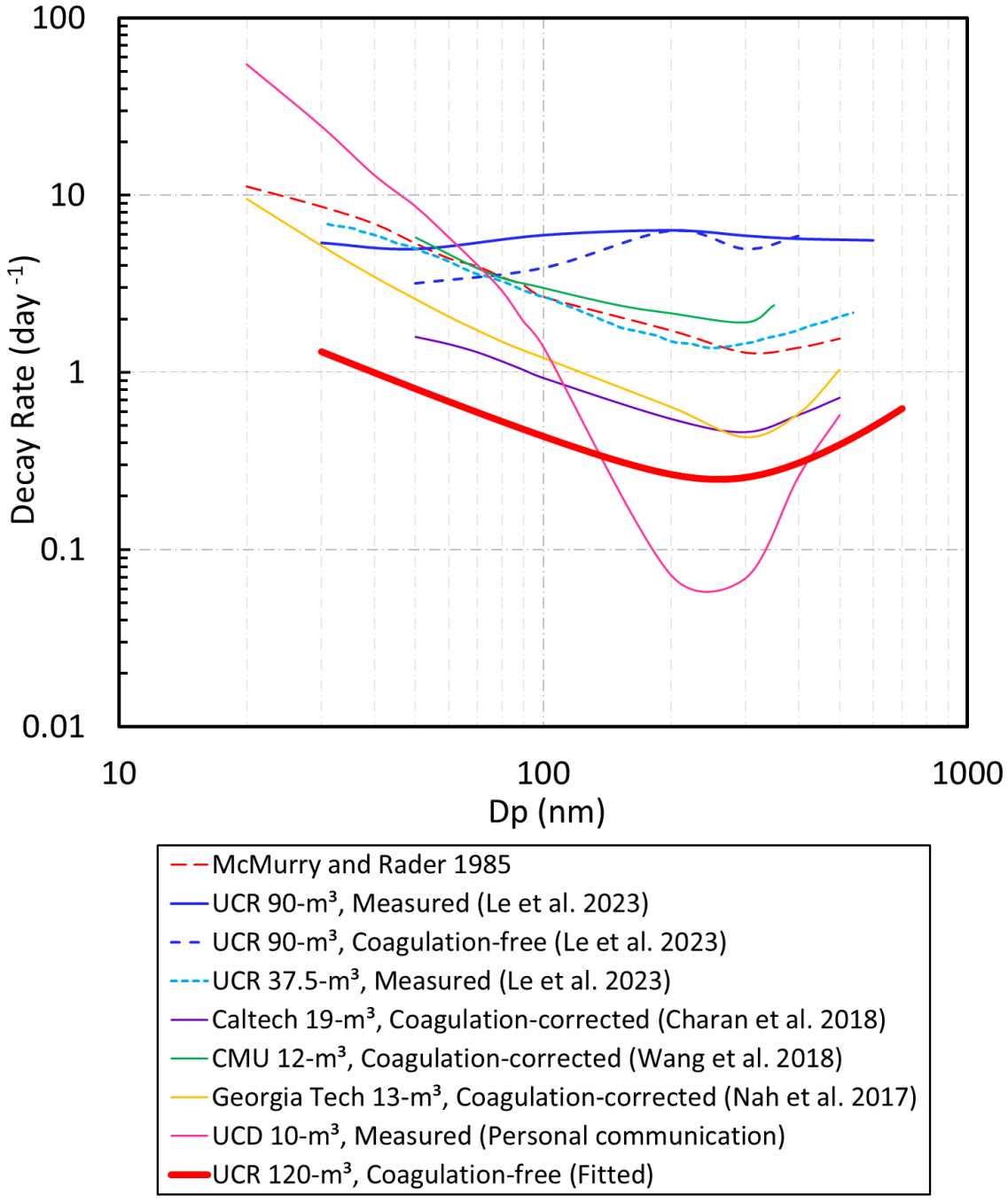

Figure 4-14. Inter-comparison of averaged or fitted size-dependent particle number loss patterns among different chamber facilities or calculations. "Measured" represents measured particle loss that includes particle-particle coagulation; "Coagulation-corrected" represents particle wall-loss rates computationally-corrected for coagulation and "Coagulation-free" represents particle wall-loss rates obtained from monodisperse particle injection experiments.

4.3.3 Evaluation of different particle wall-loss correction methods

The performance of the newly-developed Size-dependent correction method is compared to other correction methods used for UCR environmental chambers (SB-Fit method and CcDB-Fit method). Table 4-9 summarizes observations for seven experiments conducted using the new-generation UCR fixed-volume chamber while Figure 4-15 provides the corrected volume time series for sample experiment No. 2747. Among these seven analyzed experiments, the final volume concentrations using the CcDB-Fit method are always lower than final volume concentrations using the SB-Fit method because the CcDB-Fit method is using coagulation-corrected wall-loss rates. The comparison of corrected particle volumes using the CcDB-Fit method and the Size-dependent method yields a normalized root mean square deviation (NRMSD) of 4.62%, representing the averaged percent difference between the Size-dependent method and the CcDB-Fit method.

Table 4-9. List of the 7 analyzed experiments using the UCR fixed-volume chamber.

Run Number	Precursor	Duration (hr)	Max Particle Number Loading (cm^{-3})	Dilution Ratio (% per hr)	Final Volume Concentration (SB-Fit, $um^3\ cm^{-3}$)	Final Volume Concentration (CcDB-Fit, $um^3\ cm^{-3}$)	Final Volume Concentration (Size-dependent, $um^3\ cm^{-3}$)
2697	*a*-pinene	22.7	4100	0.39	52.0	48.9	45.6
2746	*a*-pinene	24.1	1850	0.60	6.0	5.9	6.2
2747	*a*-pinene	24.2	4800	0.59	39.7	36.5	35.2
2760	phenol	11.1	8000	2.52	75.8	72.2	76.5
2773	phenol	12.4	7100	3.0	56.6	53.9	56.4
2774	phenol	11.0	6500	2.9	38.3	37.4	37.4
2775	phenol	12.8	7700	3.3	42.1	40.8	39.6

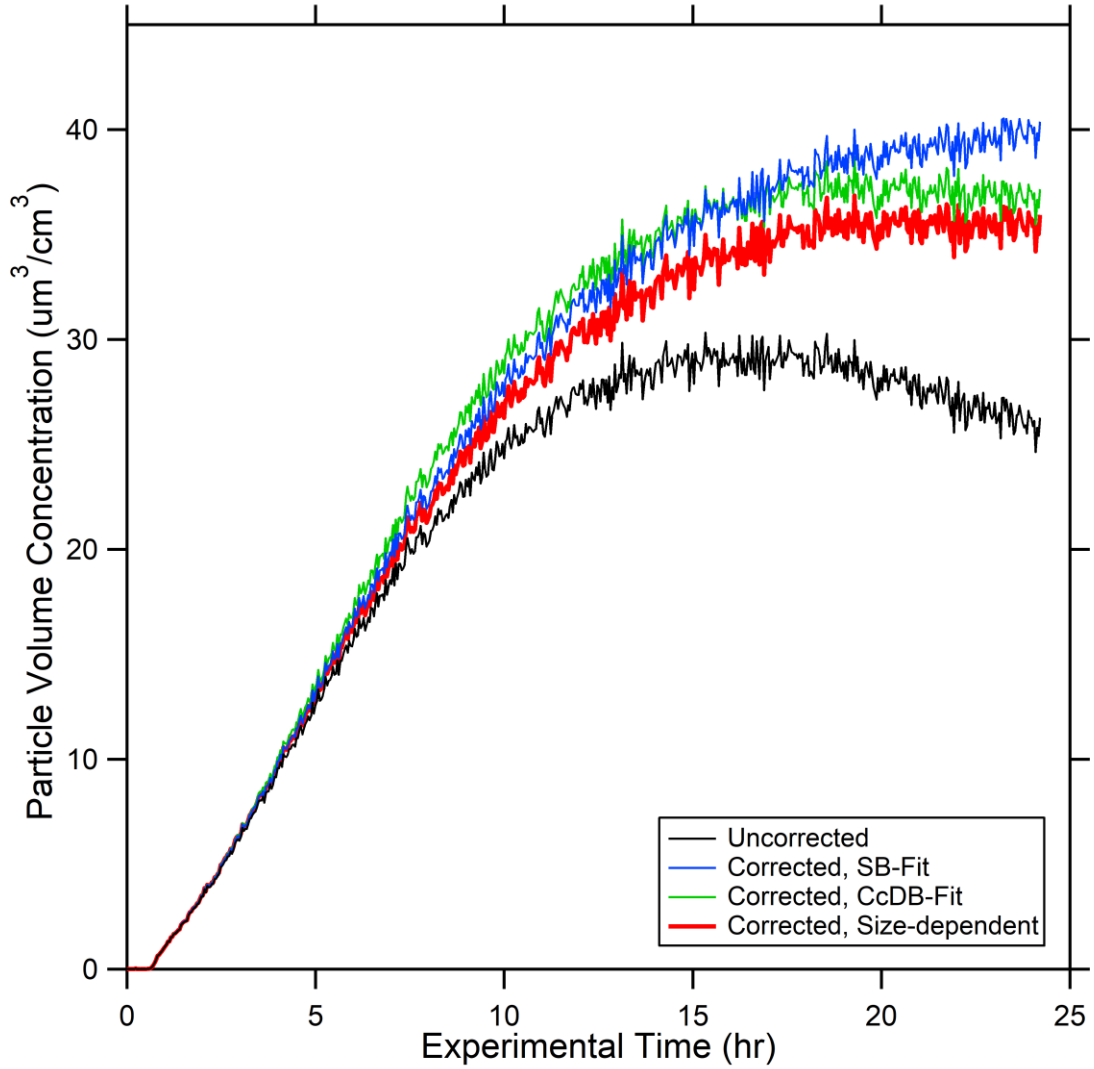

Figure 4-15. Particle volume concentration timeseries for run No. 2747. Chamber dilution correction used in all three methods used the fit of the measured tracer concentration timeseries.

The dilution correction and particle wall-loss correction are independent sections in the Size-dependent method. As discussed in Section 4.2.3.2, if measurements of the inert tracer (PFH in most of the cases) are available for an experiment, the script loads the trend directly and applies a curve fit for the experiment. When tracer data is unavailable for an experiment, the operator is asked to input a single dilution rate constant, which is used to finish the execution processes of the script. Dilution rates of the UCR fixed-volume chamber are dependent on experiment starting pressure, the total sample gas flow rates from instruments, as well as the specific chamber leak conditions during an experiment. Currently, dilution rates of experiments using the UCR fixed-volume chamber range from 0.15 to 3.3 percent per hour. A series of dilution rates are used to illustrate the sensitivity of the corrected result to the manually-input dilution rates for an experiment where inert tracer concentrations are not available. Here we present the corrected final particle volume concentrations values using both the CcDB-Fit and the Size-dependent method for run No. 2747 with a series of manually input chamber dilution rates (Table 4-10), and an example of the corrected particle volume timeseries is also presented (Figure 4-16). The final corrected particle volume concentrations calculated by the semi-empirical CcDB-Fit method are barely impacted by differing dilution rate inputs, because this correction method evaluates total loss at each time step using measured SMPS data, which accounts for changes in particle number due to combination of dilution, coagulation and wall-loss. Since coagulation correction is calculated directly from the measured particle size distribution measured by SMPS, the CcDB-Fit method subsequently balances the leftover losses between dilution and wall-loss. Therefore, the higher the input dilution rate, the lower the applied wall-loss rate, resulting in minimal changes to the overall wall-loss correction. However, when using the Size-dependent correction method, where dilution and wall-loss corrections are independent, the final corrected volume responds significantly to dilution rate inputs. The sensitivity of final wall-loss correction

to manual dilution rate inputs increases for the Size-dependent correction method for longer experimental durations. Thus, for experiments conducted in UCR fixed-volume chamber, when the experiment-specific inert tracer trend is available both the Size-dependent and CcDB-Fit correction methods are recommended to be conducted and evaluated, in order to better understand the particle wall-loss correction uncertainties.

Table 4-10. List of the corrected final particle volume concentrations for 24-hour run No. 2747 using the Size-dependent correction method with varied manual input dilution rates.

Dilution Rate (% per hr)	Final Corrected Particle Volume Concentration, Size-dependent (um^3 cm^{-3})	Final Corrected Particle Volume Concentration, CcDB-Fit (um^3 cm^{-3})
Original tracer trend	35.9	37.2
0.59 (original-trend-equivalent)	35.4	37.2
0.15	32.8	37.2
2	47.1	37.1
3	62.7	37.1

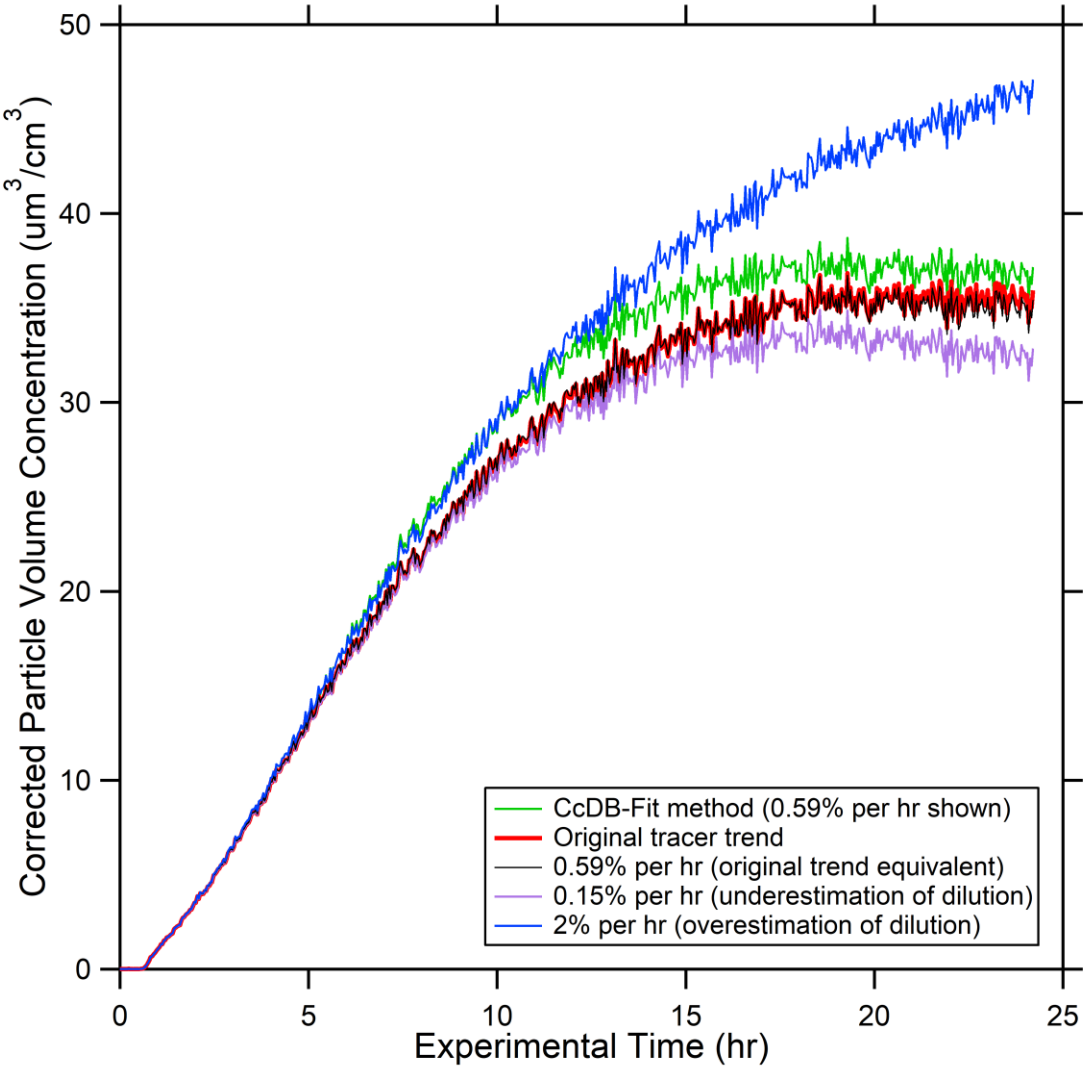

Figure 4-16. Example of corrected particle volume concentration timeseries for run No. 2747 with varied manually-input dilution rates. No visible differences were found from the CcDB-Fit method when adjusting the dilution rates thus only 0.59% per hour trend shown (Green). All other colors represent correction results using the Size-dependent method. Red curve represents the correction using the fit of the actual inert tracer trend; black curve represents the correction using the dilution rate derived from linear estimation of the actual tracer trend; purple curve represents a case of underestimation of dilution and blue curve represents a case of overestimation of dilution.

4.3.4 Polydisperse particle wall-loss patterns

Nonvolatile AS particles are widely used in environmental chambers as seed particles for SOA growth and for particle wall-loss studies. Particle wall-loss characterization experiments conducted in other chambers (e.g., Charan et al. 2018; Wang et al. 2018; Nah et al. 2017; Pierce et al. 2008) track measured particle number concentrations for each size bin, correct for coagulation and fit the losses to obtain final size-dependent, coagulation-corrected particle wall-loss rates. These other works only use polydisperse seed characterization experiments to obtain their size-dependent particle wall-loss patterns and do not have a second, independent verification of the performance of the calculated particle wall-loss pattern. In the current work, size-dependent particle wall-loss pattern for UCR fixed-volume chamber was evaluated in Section 4.3.2 using a series of monodisperse seed injection experiments and diluted single-mode SOA experiments. Further, it is commonly assumed for chamber experiments when accounting for coagulation that the shape factor is unity, meaning particle-particle coagulation is volume-conserved (therefore measured volume before and after coagulation does not change). The same shape factor assumption is also commonly applied to the polydisperse AS seed-only wall-loss characterization experiments. A series of polydisperse seed-only experiments were also used to evaluate particle wall-loss patterns in the UCR fixed-volume chamber (Table 4-3). It was observed in all three experiments that after the particle injection was complete: 1) measured total particle volume concentrations experienced an increase for several hours, then started to decrease and 2) the corrected total particle volume concentrations increased throughout the experiments (Figure 4-17). The observations clearly indicate that the SMPS-measured particle volume change in AS seed experiments is driven by more than simple particle wall-loss. It is theorized that the pure AS seed particles SMPS-measured volume is not conserved during coagulation due to the

irregular shapes of the coagulated particles. Shape factors up to 1.07 for AS particles were reported from previous studies (Kuwata and Kondo 2009; Biskos et al. 2006; Zelenyuk et al. 2006) with the factors changing as a function of particle preparation and treatment processes, such as particle drying rate and coagulation. Coagulated dimer AS particles were reported to have a shape factor of ~ 1.1 (Rothfuss and Petters 2016; Zelenyuk et al. 2006; Hinds 1999). To efficiently account for changes in particle shape during dimerization, a single shape factor for dimer particles was assigned to the Size-dependent correction method so that the corrected particle volume concentration remained constant throughout the polydisperse experiments. A shape factor of ~ 1.06 was found to plateau the wall-loss corrected particle volume concentrations for all three polydisperse experiments (Figure 4-17). This shape factor effectively accounts for the irregular shape of coagulated dimers (lower electrical mobility for the same mass particle) that led to the coagulation-corrected SMPS-measured particle volume increasing prior to shape correction. The dimer shape factor is still assumed to be 1 when processing data from normal SOA experiments.

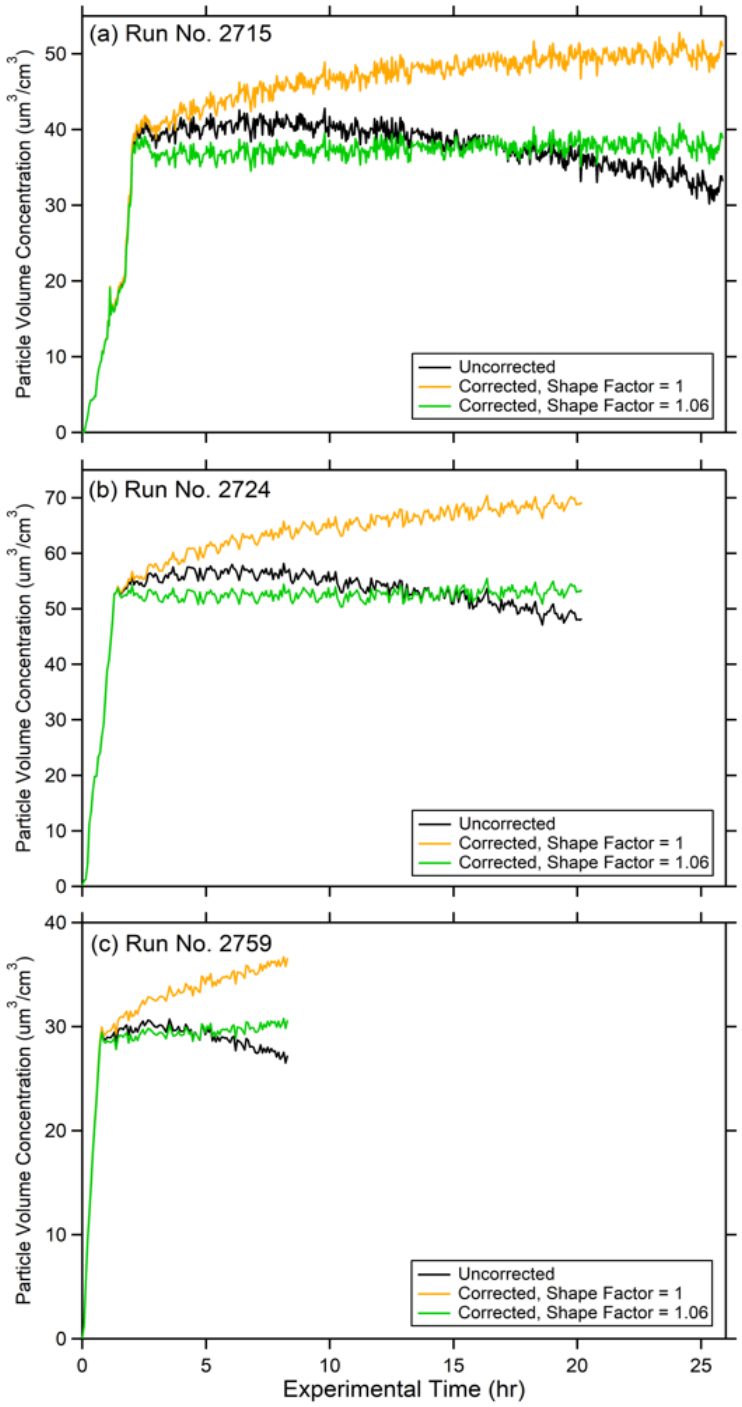

Figure 4-17. Particle volume concentration timeseries for all investigated polydisperse seed-only experiments. Black curves represent measured particle volume concentrations, orange curves represent the corrected particle volume concentrations using Size-dependent method with default shape factor and green curves represent the corrected particle volume concentrations using the same method assuming a shape factor of 1.06.

Nah et al. (2017) derived size-dependent coagulation-corrected particle wall-loss rates for polydisperse seed-only experiments under different particle number loadings, and found that the wall-loss patterns did not agree between different initial particle loadings. Theoretically, the particle loss patterns of AS seeds in a chamber are only attributed to coagulation and wall-loss, which should lead to overlap of their coagulation-corrected wall-loss patterns. The authors attributed the observation to two possible reasons – 1) particle charging difference between experiments and 2) Brownian coagulation rate coefficients being underestimated (and not resolvable scalable by applying a single multiplier to uniformly increase all K_{ij} values). Size-dependent, coagulation-corrected particle wall-loss rates for polydisperse seed-only experiments with different particle number loadings are also calculated for UCR fixed-volume chamber. The evolution of particle size distribution due to both coagulation and particle wall-loss for an example experiment is provided (Figure 4-18). As expected, the particle peak diameters shift towards larger sizes during the course of the experiments, due to the preferential particle wall- and coagulation-loss at smaller sizes compared to larger particles.

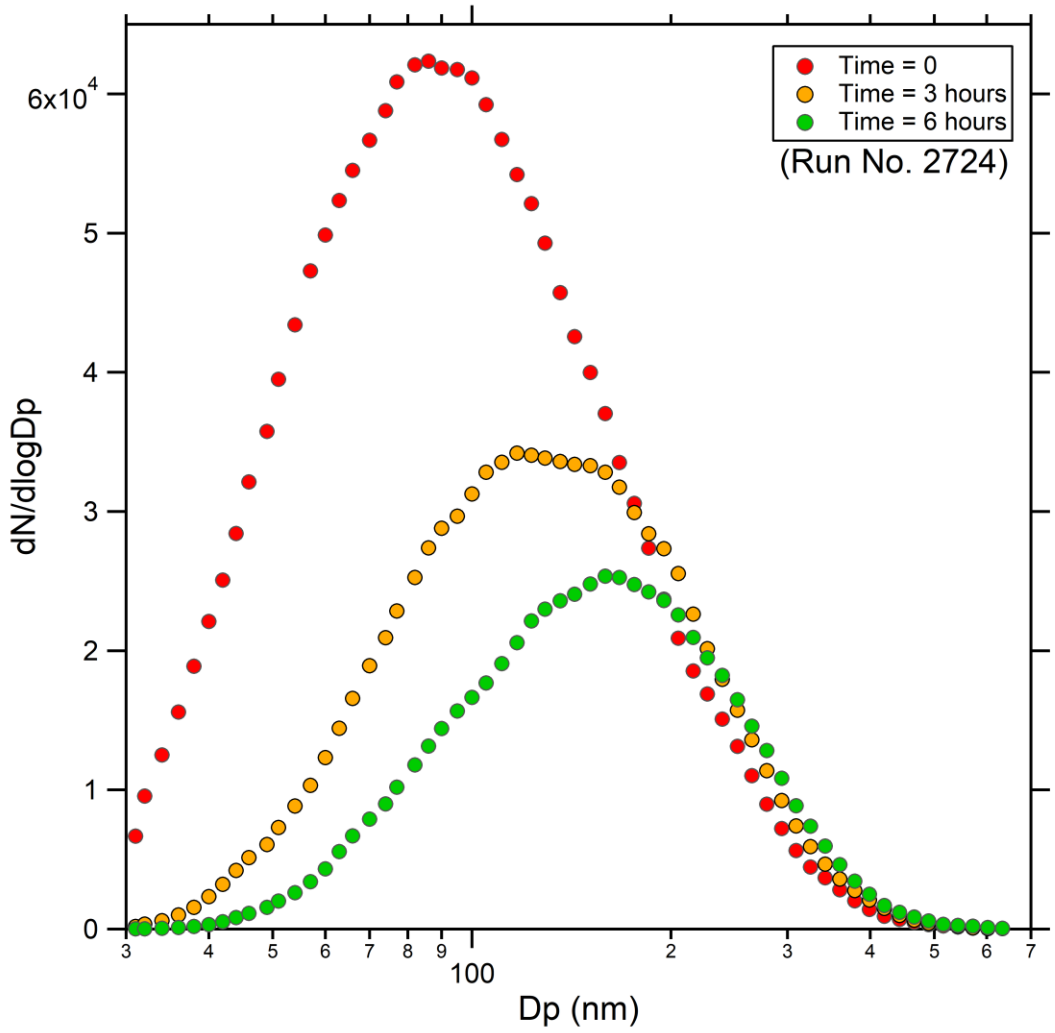

Figure 4-18. Particle size distribution evolution at different time from an example polydisperse seed-only experiment.

The six-hour average decay patterns of all three experiments with and without coagulation correction are shown (Figure 4-19a). The negative decay rates at larger particle sizes (> ~ 150 nm) for coagulation uncorrected patterns are observed due to the combination of 1) generation of larger particles from coagulation processes of smaller particles and 2) very low particle wall-loss rates at those sizes in UCR fixed-volume chamber. However, even after correcting for particle coagulation, the size-dependent coagulation-corrected particle wall-loss patterns still have negative values at some sizes and the overall curves still vary from the monodisperse fitted curve derived from the previous section. The coagulation-corrected decay rates from the experiment with 2.4×10^4 cm^{-3} initial particles (blue circles, solid) has smaller decay rates than the experiments with ~ 3.4×10^4 cm^{-3} initial particles (red and green circles, solid). The curves also reach their minimum value at different sizes (~ 220 nm for blue; ~ 260 nm for red and green). The discrepancies in this work are not as significant as Nah et al. (2017), likely due to our smaller particle loading differences. Possible reasons for the negative decay rate values after accounting for coagulation can be 1) the coagulation coefficients (K_{ij}) are too low (imperfect assumption that coagulation is only Brownian); 2) errors when accounting for multiply-charged particles within the SMPS inversion code; and 3) particle decay rates in UCR collapsible chambers are much lower than coagulation effects at these sizes making these size ranges extremely sensitive to small biases in the coagulation corrections. Dynamic particle wall-loss rates at each size bins were also found to change with experimental time, further supporting the observation that current particle-particle coagulation calculations may not be accurate. The sensitivity of average size-dependent coagulation-corrected decay rates to coagulation correction were evaluated by doubling the coagulation rate constants for all sizes (Figure 4-19b). Particle wall-loss patterns doubling K_{ij} reduce the number of size bins with negative loss and lower wall-loss rates for smaller sizes; however, negative decay rates start to appear for the smallest sizes.

This indicates that the bias between the current coagulation calculation and the observed loss rate differs with particle size. Thus, monodisperse particle wall-loss characterizations are still recommended for an environmental chamber facility to directly bypass the need for coagulation correction and reduce the uncertainties in measured size-dependent particle wall-loss patterns.

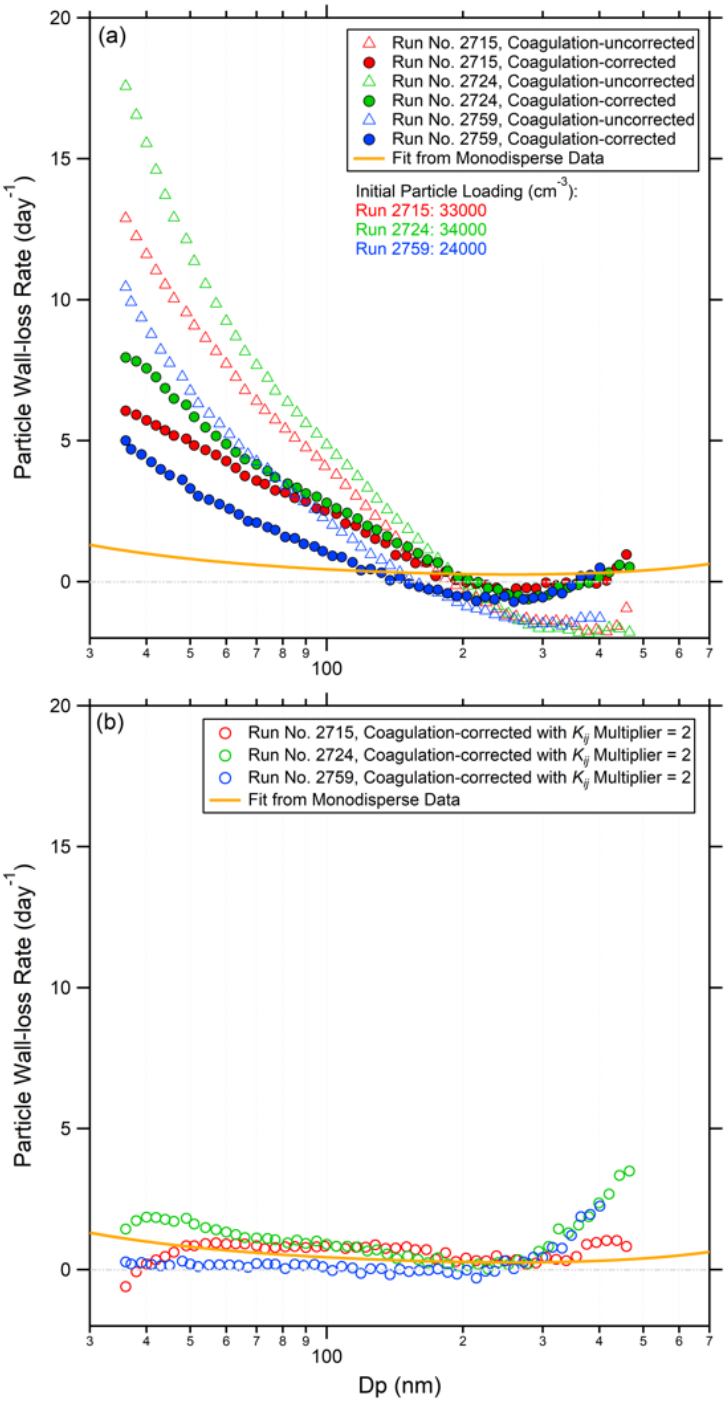

Figure 4-19. Averaged size-dependent particle wall-loss patterns collected from all investigated polydisperse seed-only experiments. The averaging time is 6 hours after the total particle number reaches the maximum for each investigated experiment. **(a)** presents coagulation-uncorrected patterns (triangles), coagulation-corrected patterns (solid circles) with manual shape factor of 1.06 and pattern fitted from monodisperse data (orange curve). **(b)** displays coagulation-corrected patterns (hollow circles) with shape factor of 1.06 and all coagulation rate constants are scaled up by a factor of 2.

4.4 Conclusions

The UCR/CE-CERT new-generation 120-m^3 fixed-volume chamber has been constructed to mitigate particle wall-loss based on findings in the previous two chapters. The new chamber has a larger volume compared to the previous-generation chamber. Particles in the new chamber are lost to the wall surfaces much slower, reducing the correction for particle volume wall-loss and enabling longer-duration (up to multiple days) experiments. The new chamber is no longer collapsible, simplifying the experimental and cleaning operations. The new chamber is electrically isolated from surrounding conductive materials in the enclosure room to minimize introduction of electrostatic charges to the chamber surfaces. Using external soft x-ray photo ionizers ensures the neutralization of chamber surfaces prior to experiments. The combined mitigation efforts greatly reduce the overall particle wall-loss rates by minimizing the effect of chamber surface charges. Chamber dilution is no longer negligible due to the fixed-volume chamber design; therefore, dilution effects on particle loss are tracked and corrected by measuring the decay of an inert tracer during the course of an experiment.

Particle wall-loss correction methods from earlier chapters are based on real-time SMPS measurements and include the empirical "SB-Fit" method and the semi-empirical "CcDB-Fit" method. A series of monodisperse particle wall-loss experiments support the hypothesis of minimum electrostatic effect by yielding a "spoon" curve and being able to be fit to the Crump and Seinfeld (1981) theory using k_e = 0.062 s^{-1} and neglecting the electric field. The size-dependent particle wall-loss patterns of the UCR fixed-volume chamber are far lower than most of the recently-reported decay patterns from other chamber facilities.

An interactive script based on the MATLAB platform has been developed to create the "Size-dependent" method to correct the particle wall-loss based on the monodisperse characterization results. The Size-dependent method calculates the particle losses due to chamber dilution, coagulation out-of-bound and size-dependent particle wall-loss independently. The particle volume/mass correction results using this method are sensitive to manually-input dilution rates when tracer dilution data is unavailable. Therefore, reliable tracer concentration measurements should be conducted for every experiment in the new chamber. The script also provides corrections using the traditional SB-Fit and the CcDB-Fit method, empowering the operators to calculate multiple correction results using multiple methods to further understand particle wall-loss correction uncertainties. Currently, particle-loss correction results using the CcDB-Fit method and the new Size-dependent method yield an averaged 4.62% volume-growth bias. Further evaluations between the performances of the methods are warranted for different experimental designs and particle size distributions time series.

The script also generates size-dependent, coagulation-corrected particle wall-loss rates for polydisperse seed-only experiments. An overall shape factor of ~ 1.06 was needed to account for the apparent SMPS-measured volume increase. It is recommended that chamber operators using SMPS-based particle size distributions consider the shape factor when characterizing particle wall loss using dry polydisperse AS particles. The combinations of low overall particle wall-loss rates in UCR fixed-volume chambers and inaccuracies in coagulation calculations led to some negative size-dependent particle wall-loss rates after correction for coagulation. Further evaluation of appropriate K_{ij} values representative of the coagulation processes within the chamber is warranted. Additionally, monodisperse seed-only characterization experiments are recommended to directly obtain coagulation-free particle wall-loss patterns without having to account for coagulation.

Most importantly, electrostatically-susceptible collapsible chambers with data acquisition and processing based on the WinXP, Office 2003 and LabVIEW 6 platforms were used prior to 2019. During this thesis work our chamber system progressed significantly to an electrostatically-minimized fixed-volume chamber with data acquisition and processing based on Windows 10, Office 2016 and LabVIEW 19 or even later versions, all of which required major upgrades and new approaches within the LabVIEW-based instrumentation and formerly excel-based data analysis package. The developed interactive script in this work is a key milestone for chamber data applications and establishes a new platform for clustering and managing multi-instrument data for environmental chamber experiments.

Chapter 5: Summary of Major Findings and Suggested Future Works

This thesis summarizes the latest understanding on particle loss processes when conducting experiments in different generations of indoor Teflon environmental chambers at CE-CERT, UCR. The insights not only contribute to how to evaluate particle loss and correct chamber data more accurately and responsibly for experiments conducted in UCR previous and new generations of chambers, but also provide information and suggestions to the whole environmental chamber community.

5.1 Where we were before

The averaged particle decay rates in UCR collapsible chambers were relatively insensitive to particle size, with a large day-to-day variance. Thus, the experiment-specific, number-averaged and size-independent decay rates were determined using SMPS data acquired from each conducted chamber experiment. Coagulation was assumed to be insignificant and therefore tools were not developed and coagulation was not accounted for in prior experiments. This assumption meant that empirical number-averaged particle wall-loss rates derived directly from measured SMPS data included both loss of particles to the wall and due to coagulation. This resulted in overestimation of the particle wall-loss when correcting for particle volume losses. Additionally, the average particle wall-loss in the 90-m^3 UCR collapsible chambers, the largest indoor environmental chambers in the world, exceeded those reported for some smaller-sized

(~ 10 to 20-m^3) chambers. Therefore, the large particle wall-loss rates, combined with the aforesaid reasons, led to significant uncertainty and potential bias during evaluation of SOA formation potentials using our previous-generation collapsible chambers. Corrections for number/volume/mass lost during experiments were on the order of hundreds of percent of the final measured values. The relatively high average particle wall-loss rates may have also resulted in underrepresentation of semi-volatile vapor wall-loss and hindered assessment of these processes. All in all, the scientific questions prior to the existence of this thesis were:

1) What caused the relative high particle wall-loss rates and significant day-to-day variance in UCR collapsible chambers?

2) Acknowledging the limitations of the traditional number-averaged particle wall-loss correction method, can we develop a better correction method to more accurately account for particle loss?

3) What improvements in chamber design are necessary to decrease the actual particle wall-loss rate and further improve measurements of SOA formation?

5.2 Where we are now

As of completion of this thesis, the understanding of the cause of the large particle-wall loss behavior in the UCR 90-m^3 collapsible chambers has been significantly moved forward. To answer the ***first*** scientific question, the keywords are "electrostatics" and "particle charging dynamics".

As discussed in Chapter 2, for UCR previous-generation collapsible chambers, experimental observations clearly demonstrated the fact that the particle wall-loss behaviors were significantly affected by the charged chamber surfaces. The enhancement of particle wall-loss rates due to electrostatics effect are explained by 1) the chamber was collapsible leading to

friction of the wall material; 2) the chamber walls were constantly rubbing against each other in the dual-chamber design due to the external mixing system (air handlers) during experiments, 3) the chamber walls were in direct contact with the reflective and conductive aluminum enclosure that it resides in, and 4) the chamber walls were frequently touched by operators during the post-experiment cleaning processes. The dominant electrostatics effect caused day-to-day particle wall-loss variabilities, insensitivity to size-dependent particle wall-loss, and relatively-high reported particle wall-loss rates in UCR collapsible chambers.

Particle charging dynamics also play a key role in particle wall-loss behaviors. The particles inside a chamber originate from nucleation or from direct injection of seed particles prior to the start of the experiment. The suspended particles continuously interact with surrounding ions caused by ubiquitous cosmic radiation, resulting in dynamic particle charging/discharging processes approaching a chamber-specific particle charge steady-state during the course of an experiment. Further, charged particles were observed to be lost to the charged chamber walls much faster than were the un-charged yet particles with the difference a strong function of particle size. Smaller charged particles (e.g., 50 nm) experience much faster preferential loss to the charged chamber walls than do larger charged particles (e.g., 200 nm); however, smaller particles have a greater kinetic charging limitation, resulting in much slower charge replenishing rates for the smaller particles. Combining both aforesaid processes, 1) particles tend to reach a case-specific charge steady-state inside the chamber during the course of an experiment, with the overall decay rate boosted by the charged chamber surfaces and 2) the electrostatic enhancement on particle wall-loss in UCR collapsible chambers varies with particle size and experimental time due to the dynamic change of the particle charge distributions.

A dual-SMPS setup is introduced where the particle neutralizer is only used in one of the SMPS to study the behaviors of size-resolved charged and total particles. An experimental

protocol of injecting mono-dispersed seed particles to the chamber to avoid coagulation correction calculations was recommended, and for a large chamber, a high-flow DMA system was applied to achieve the measurable particle loadings.

To answer the ***second*** scientific question, the answer is: "Yes, we can. The modified correction method needs to calculate particle wall-loss rates after accounting for particle-particle coagulation and the method also must account for any dynamic changes of particle wall-loss rates during the course of an experiment."

As discussed in Chapter 3, the traditional particle wall-loss correction method used for UCR collapsible chambers did not rule out the interference from particle-particle coagulation, causing overestimation of the corrected particle volume/mass. A particle coagulation dynamics model was developed to calculate the dynamic coagulation-corrected particle wall-loss rates. The modified correction method also accounts for the dynamic change of the particle wall-loss rates during an experiment, which is attributed to the change of particle size and charge distribution along with changing chamber geometry. Combining both features, the new model performs more accurate particle wall-loss corrections, reducing uncertainties and bias due to coagulation and particle dynamics. The model was then used to re-evaluate the particle wall-loss correction results from ~ 2000 valid historical experiments conducted in the UCR collapsible chamber during the past two decades. The new analysis furthers our understanding of the significance of coagulation processes and particle wall-loss evolution during an experiment, as well as the extent to which coagulation impacts the traditional wall-loss correction as a function of particle number loadings. The increased accuracy of particle wall-loss correction is currently being applied to and used to evaluate standard SOA characterization experimental repeats (80 ppb *m*-xylene + 50 ppb NO) over the past two decades. Preliminary data shows that even maintaining constant initial injections goals, small subtleties still cause measurable bias regarding the generated SOA.

To answer the ***third*** scientific question, the answer is: "Yes, we need an improved chamber design, with mitigation strategies applied to reduce the electrostatic effect. Next, we need to re-characterize the particle wall-loss patterns for our new facility."

As discussed in Chapter 4, the UCR new-generation 120-m^3 fixed-volume chamber has been constructed to replace the previous-generation collapsible dual chambers. Mitigation strategies applied to the chamber design include removing contact between chamber surfaces and other materials and the use of external soft x-ray photo ionizers to reduce chamber surface charge. This resulted in the reduction of particle wall-loss rates due to chamber surface charging for the new chamber leading to an order of magnitude (or more) reduction in particle wall-loss rates. The rates were fully characterized as a function of particle size using a series of monodisperse particle injection wall-loss experiments, where the total particle number concentrations present in the chamber were small enough to ignore coagulation. Size-dependent, coagulation-free particle wall-loss rates were then obtained by the optimized fitting of the experimental data based on the traditional Crump and Seinfeld (1981) theory.

A new particle wall-loss correction method was explored after acquiring the size-dependent decay patterns for the UCR new chamber. This method evaluates the particle wall-loss from the size-dependency perspective while the previously-used methods ("SB-Fit" and "CcDB-Fit" methods) fundamentally packaged and fitted such dependency into single factors. At the same time, the raw SMPS file outputs experienced a major format change after a critical system and software update occurred in 2019. As the result, a MATLAB script was developed to process the updated raw files while being able to also perform particle wall-loss corrections using both historical methods and the newly-developed method. All correction methods have been updated to include the ability to correct for chamber dilution (which the current chamber setup is subject to). Good agreement on the correction performances was found between the Size-dependent

method and the CcDB-Fit method when properly accounting for chamber dilution. Both correction methods will be used for future experiments with the UCR fixed-volume chamber in order to further understand particle wall-loss correction uncertainties. Additionally, attempts have been made to characterize the size-dependent wall-loss pattern for the new chamber using coagulation-corrected data from polydisperse dry seed-only experiments. It was observed that the coagulation of dry ammonium sulfate particles resulted in a measured increase in total particle volume due to the irregular shape of the coagulated dimers. Therefore, the volume-conserved coagulation assumption does not hold in a polydisperse dry AS particle system, and in our case, a shape factor of ~ 1.06 was determined to be most accurate to represent the coagulated dimer sizes. It was also found that the coagulation corrected polydisperse dry AS system was not effective for evaluating particle size dependent wall loss in the UCR fixed-volume chamber due to the relative magnitude of the coagulation correction compared to the wall loss rates for select particle sizes. Therefore, the coagulation-minimized monodisperse seed injection method is recommended to characterize the size-dependent particle wall-loss patterns for environmental chambers with small particle wall-loss rates.

5.3 Where to go in the future

As of completion of this thesis, tools have been developed and the platform has been established to better understand particle dynamics within multiple generations of UCR/CE-CERT environmental chambers. The journey of research is still ongoing: a massive data pool of historical experiments using the 90-m^3 collapsible chambers with improved accuracy has been unlocked and an upgraded chamber with optimized particle wall-loss rates has been put into use.

Looking backward, two decades of historical data, including but not limited to the updated corrections of SOA volume/mass concentrations, is readily accessible via the new data

clustering and processing platform. Some particle dynamic parameters that impact SOA yield are extracted by the new platform from historical experiments, such as maximum particle number loading, particle peak size during nucleation or after aging, particle surface area mid-nucleation, precursor consumption rate, etc. These parameters are critical for future investigations via traditional evaluation routes, for investigations of SOA formation with respect to gas-phase kinetic modeling, or for new interdisciplinary applications (e.g., machine learning). Re-evaluation of historical experimental data sets for different SOA systems is recommended. Improved prediction of dynamic particle wall-loss also warrants re-evaluation of experiments where environmental parameters were designed to change during the experiments, such as chamber temperature or humidity. The repeatability of the standard chamber experiment for both characterization and training purposes requires further exploration from an experimental operational perspective. The deliverable plots from the model can also help future users easily identify problematic data points from historical experiments leading to quick decisions to fix the experimental data. The same platform can even be modified for re-assessing experiments with other chambers, such as UCR Mez chamber and Mobile chamber.

Looking forward, with the upgraded UCR fixed-volume chamber, experiments with much longer durations can be explored, enabling investigations on precursor compounds undergoing extended oxidation or environmental parameter changes. Vapor wall-loss investigations are also recommended that take advantage of the significantly lower particle wall-loss interferences. With the development of the size-dependent particle wall-loss correction method, all future experiments are recommended to be evaluated using both methods simultaneously to understand the particle wall-loss correction uncertainties. The new environmental chamber design can be used to evaluate SOA generation with very different extents of particle wall-loss. For example, experiments with designs similar to ones conducted in

previous chambers can be reproduced in the new chamber providing insight into the extent of gas-particle partitioning to particles that have been lost to the wall. More importantly, further platform development based on the current data clustering and processing system are warranted to better manage and record multiple instrumental data in the era of new software/hardware.

Bibliography

Adachi, M., Kousaka, Y., and Okuyama, K. (1985). Unipolar and bipolar diffusion charging of ultrafine aerosol particles. *J. Aerosol Sci.* 16 (2):109–123. doi:10.1016/0021-8502(85)90079-5.

"Ambient (outdoor) Air Pollution." (2022). World Health Organization, 19 December 2022, https://www.who.int/news-room/fact-sheets/detail.

Bakolis, I., Hammoud, R., Stewart, R., Beevers, S., Dajnak, D., MacCrimmon, S., Broadbent, M., Pritchard, M., Shiode, N., Fecht, D., Gulliver, J., Hotopf, M., Hatch, S.L., and Mudway, I.S. (2021). Mental health consequences of urban air pollution: prospective population-based longitudinal survey. *Soc. Psychiatry Psychiatr. Epidemiol.* 56 (9):1587–1599. doi:10.1007/s00127-020-01966-x.

Bell, M.L., Dominici, F., Ebisu, K., Zeger, S.L., and Samet, J.M. (2007). Spatial and temporal variation in PM2.5 chemical composition in the United States for health effects studies. *Environ. Health Perspect.* 115 (7):989–995. doi:10.1289/ehp.9621.

Biskos, G., Paulsen, D., Russell, L.M., Buseck, P.R., and Martin, S.T. (2006). Prompt deliquescence and efflorescence of aerosol nanoparticles. *Atmos. Chem. Phys.* 6 (12):4633–4642. doi:10.5194/acp-6-4633-2006.

Biskos, G., Reavell, K., and Collings, N. (2005). Unipolar diffusion charging of aerosol particles in the transition regime. *J. Aerosol Sci.* 36 (2):247–265. doi:10.1016/j.jaerosci.2004.09.002.

Bowman, F.M., Odum, J.R., Seinfeld, J.H., and Pandis, S.N. (1997). Mathematical model for gas-particle partitioning of secondary organic aerosols. *Atmos. Environ.* 31 (23):3921–3931. doi:10.1016/S1352-2310(97)00245-8.

Brunekreef, B. and Holgate, S.T. (2002). Air pollution and health. *Lancet* 360 (9341):1233–1242. doi:10.1016/S0140-6736(02)11274-8.

Buckley, A.J., Wright, M.D., and Henshaw, D.L. (2008). A technique for rapid estimation of the charge distribution of submicron aerosols under atmospheric conditions. *Aerosol Sci. Technol.* 42 (12):1042–1051. doi:10.1080/02786820802400645.

Carter, W.P.L., Cocker, D.R., Fitz, D.R., Malkina, I.L., Bumiller, K., Sauer, C.G., Pisano, J.T., Bufalino, C., and Song, C. (2005). A new environmental chamber for evaluation of gas-phase chemical mechanisms and secondary aerosol formation. *Atmos. Environ.* 39 (40):7768–7788. doi:10.1016/j.atmosenv.2005.08.040.

Charan, S.M., Huang, Y., and Seinfeld, J.H. (2019). Computational Simulation of Secondary Organic Aerosol Formation in Laboratory Chambers. *Chem. Rev.* 119 (23):11912–11944. doi:10.1021/acs.chemrev.9b00358.

Charan, S.M., Kong, W., Flagan, R.C., and Seinfeld, J.H. (2018). Effect of particle charge on aerosol dynamics in Teflon environmental chambers. *Aerosol Sci. Technol.* 52 (8):854–871. doi:10.1080/02786826.2018.1474167.

Cocker, D.R., Flagan, R.C., and Seinfeld, J.H. (2001). State-of-the-art chamber facility for studying atmospheric aerosol chemistry. *Environ. Sci. Technol.* 35 (12):2594–2601. doi:10.1021/es0019169.

Collins, D.R., Flagan, R.C., and Seinfeld, J.H. (2002). Improved inversion of scanning DMA data. *Aerosol Sci. Technol.* 36 (1):1–9. doi:10.1080/027868202753339032.

Cooper, G., Langer, G., and Rosinski, J. (1979). Submicron Aerosol Losses in Aluminized Mylar Bags. *J. Appl. Meteorol.* (1962-1982), 18 (1): 57–68. doi:10.1175/1520-0450(1979)018<0057:SALIAM>2.0.CO;2.

Corner, J. and Pendlebury, E.D. (1951). The coagulation and deposition of a stirred aerosol. *Proc. Phys. Soc. Sect. B* 64 (8):645–654. doi:10.1088/0370-1301/64/8/304.

Crump, J.G., Flagan, R.C., and Seinfeld, J.H. (1982). Particle wall loss rates in vessels. *Aerosol Sci. Technol.* 2 (3):303–309. doi:10.1080/02786828308958636.

Crump, J.G. and Seinfeld, J.H. (1981). Turbulent deposition and gravitational sedimentation of an aerosol in a vessel of arbitrary shape. *J. Aerosol Sci.* 12 (5):405–415. doi:10.1016/0021-8502(81)90036-7.

Dahneke, B.E. (1973). Slip correction factors for nonspherical bodies-III the form of the general law. *J. Aerosol Sci.* 4 (2):163–170. doi:10.1016/0021-8502(73)90067-0.

De Gouw, J. and Jimenez, J.L. (2009). Organic aerosols in the earth's atmosphere. *Environ. Sci. Technol.* 43 (20):7614–7618. doi:10.1021/es9006004.

Donahue, N.M., Robinson, A.L., Stanier, C.O., and Pandis, S.N. (2006). Coupled partitioning, dilution, and chemical aging of semivolatile organics. *Environ. Sci. Technol.* 40 (8):2635–2643. doi:10.1021/es052297c.

Franchin, A., Ehrhart, S., Leppä, J., Nieminen, T., Gagné, S., Schobesberger, S., Wimmer, D., Duplissy, J., Riccobono, F., Dunne, E.M., Rondo, L., Downard, A., Bianchi, F., Kupc, A., Tsagkogeorgas, G., Lehtipalo, K., Manninen, H.E., Almeida, J., Amorim, A., Wagner, P.E., Hansel, A., Kirkby, J., Kürten, A., Donahue, N.M., Makhmutov, V., Mathot, S., Metzger, A., Petäjä, T., Schnitzhofer, R., Sipilä, M., Stozhkov, Y., Tomé, A., Kerminen, V.M., Carslaw, K., Curtius, J., Baltensperger, U., and Kulmala, M. (2015). Experimental investigation of ion-ion recombination under atmospheric conditions. *Atmos. Chem. Phys.* 15 (13):7203–7216. doi:10.5194/acp-15-7203-2015.

Fuchs, N.A. (1963). On the stationary charge distribution on aerosol particles in a bipolar ionic atmosphere. *Geofis. Pura e Appl.* 56 (1):185–193. doi:10.1007/BF01993343.

Fuchs, N. A. (1964). The mechanics of aerosols. *Pergamon Press Oxford.*

Ghadimi S., Li H., Le C., Porter W. C. and Cocker D. R.: Influence of Continuous NOx Injection on SOA Yield from Biogenic Precursors: A Comprehensive Branching Ratio Study (in preparation, expected to be published in 2023)

Hallquist, M., Wenger, J.C., Baltensperger, U., Rudich, Y., Simpson, D., Claeys, M., Dommen, J., Donahue, N.M., George, C., Goldstein, A.H., Hamilton, J.F., Herrmann, H., Hoffmann, T., Iinuma, Y., Jang, M., Jenkin, M.E., Jimenez, J.L., Kiendler-Scharr, A., Maenhaut, W., McFiggans,

G., Mentel, T.F., Monod, A., Prévôt, A.S.H.H., Seinfeld, J.H., Surratt, J.D., Szmigielski, R., and Wildt, J. (2009). The formation, properties and impact of secondary organic aerosol: Current and emerging issues. *Atmos. Chem. Phys.* 9 (14):5155–5236. doi:10.5194/acp-9-5155-2009.

Haywood, J. and Boucher, O. (2000). Estimates of the direct and indirect radiative forcing due to tropospheric aerosols: A review. *Rev. Geophys.* 38 (4):513–543. doi:10.1029/1999RG000078.

He, M. and Dhaniyala, S. (2014). Experimental characterization of flowrate-dependent bipolar diffusion charging efficiencies of sub-50nm particles. *J. Aerosol Sci.* 76:175–187. doi:10.1016/j.jaerosci.2014.06.009.

Hildebrandt, L., Donahue, N.M., and Pandis, S.N. (2009). High formation of secondary organic aerosol from the photo-oxidation of toluene. *Atmos. Chem. Phys.* 9 (9):2973–2986. doi:10.5194/acp-9-2973-2009.

Hinds, W. C. (1999). Aerosol Technology: Properties, Behavior and Measurement of Airborne Particles (2nd ed.). *John Wiley & Sons*, New York, pp. 52.

Hoppel, W.A. and Frick, G.M. (1986). Ion—aerosol attachment coefficients and the steady-state charge distribution on aerosols in a bipolar ion environment. *Aerosol Sci. Technol.* 5 (1):1–21. doi:10.1080/02786828608959073.

Jimenez, J.L., Canagaratna, M.R., Donahue, N.M., Prevot, A.S.H., Zhang, Q., Kroll, J.H., DeCarlo, P.F., Allan, J.D., Coe, H., Ng, N.L., Aiken, A.C., Docherty, K.S., Ulbrich, I.M., Grieshop, A.P., Robinson, A.L., Duplissy, J., Smith, J.D., Wilson, K.R., Lanz, V.A., Hueglin, C., Sun, Y.L., Tian, J., Laaksonen, A., Raatikainen, T., Rautiainen, J., Vaattovaara, P., Ehn, M., Kulmala, M., Tomlinson, J.M., Collins, D.R., Cubison, M.J., Dunlea, E.J., Huffman, J.A., Onasch, T.B., Alfarra, M.R., Williams, P.I., Bower, K., Kondo, Y., Schneider, J., Drewnick, F., Borrmann, S., Weimer, S., Demerjian, K., Salcedo, D., Cottrell, L., Griffin, R., Takami, A., Miyoshi, T., Hatakeyama, S., Shimono, A., Sun, J.Y., Zhang, Y.M., Dzepina, K., Kimmel, J.R., Sueper, D., Jayne, J.T., Herndon, S.C., Trimborn, A.M., Williams, L.R., Wood, E.C., Middlebrook, A.M., Kolb, C.E., Baltensperger, U., and Worsnop, D.R. (2009). Evolution of organic aerosols in the atmosphere. *Science (80-.).* 326 (5959):1525–1529. doi:10.1126/science.1180353.

Kasper, G. (1982). Dynamics and measurement of smokes. I: Size characterization of nonspherical particles. *Aerosol Sci. Technol.* 1 (2):187–199. doi:10.1080/02786828208958587.

Kirkby, J., Duplissy, J., Sengupta, K., Frege, C., Gordon, H., Williamson, C., Heinritzi, M., Simon, M., Yan, C., Almeida, J., Trostl, J., Nieminen, T., Ortega, I.K., Wagner, R., Adamov, A., Amorim, A., Bernhammer, A.K., Bianchi, F., Breitenlechner, M., Brilke, S., Chen, X., Craven, J., Dias, A., Ehrhart, S., Flagan, R.C., Franchin, A., Fuchs, C., Guida, R., Hakala, J., Hoyle, C.R., Jokinen, T., Junninen, H., Kangasluoma, J., Kim, J., Krapf, M., Kurten, A., Laaksonen, A., Lehtipalo, K., Makhmutov, V., Mathot, S., Molteni, U., Onnela, A., Perakyla, O., Piel, F., Petaja, T., Praplan, A.P., Pringle, K., Rap, A., Richards, N.A.D., Riipinen, I., Rissanen, M.P., Rondo, L., Sarnela, N., Schobesberger, S., Scott, C.E., Seinfeld, J.H., Sipila, M., Steiner, G., Stozhkov, Y., Stratmann, F., Tomé, A., Virtanen, A., Vogel, A.L., Wagner, A.C., Wagner, P.E., Weingartner, E., Wimmer, D., Winkler, P.M., Ye, P., Zhang, X., Hansel, A., Dommen, J., Donahue, N.M., Worsnop, D.R., Baltensperger, U., Kulmala, M., Carslaw, K.S., and Curtius, J. (2016). Ion-induced nucleation of pure biogenic particles. *Nature* 533 (7604):521–526. doi:10.1038/nature17953.

Kuwata, M. and Kondo, Y. (2011). Measurements of particle masses of inorganic salt particles for calibration of cloud condensation nuclei counters. *Inorg. Chem. React. Struct. Mech.* 240–262. doi:10.1201/b12873-13.

Le C., Xu N., Li Q., Collins D. R. and Cocker D. R.: Experimental Characterization of Particle Wall-loss Behaviors in UCR Dual-90m3 Teflon Chambers (Ready to submit, expected to be published in 2023)

Leskinen, A., Yli-Pirilä, P., Kuuspalo, K., Sippula, O., Jalava, P., Hirvonen, M.R., Jokiniemi, J., Virtanen, A., Komppula, M., and Lehtinen, K.E.J. (2015). Characterization and testing of a new environmental chamber. *Atmos. Meas. Tech.* 8 (6):2267–2278. doi:10.5194/amt-8-2267-2015.

Li Q. (2022). Modifying Environmental Chambers for Varying Applications: From Evaluating Secondary Organic Aerosol Formation to Health Effects Investigation with Animal Exposure (Doctoral dissertation). University of California, Riverside, Riverside.

Liu, B.Y., and Lee, K.W. (1975). An aerosol generator of high stability. *American Industrial Hygiene Association journal, 36 12,* 861-5. doi: 10.1080/0002889758507357.

Loza, C.L., Chhabra, P.S., Yee, L.D., Craven, J.S., Flagan, R.C., and Seinfeld, J.H. (2012). Chemical aging of m-xylene secondary organic aerosol: Laboratory chamber study. *Atmos. Chem. Phys.* 12 (1):151–167. doi:10.5194/acp-12-151-2012.

Mahfouz, N.G.A. and Donahue, N.M. (2020). Primary ion diffusion charging and particle wall loss in smog chamber experiments. *Aerosol Sci. Technol.* 54 (9):1058–1069. doi:10.1080/02786826.2020.1757032.

Malloy, Q.G.J., Nakao, S., Qi, L., Austin, R., Stothers, C., Hagino, H., and Cocker, D.R. (2009). Real-Time aerosol density determination utilizing a modified scanning mobility particle sizer aerosol particle mass analyzer system. *Aerosol Sci. Technol.* 43 (7):673–678. doi:10.1080/02786820902832960.

Marlow, W.H. and Brock, J.R. (1975). Calculations of bipolar charging of aerosols. *J. Colloid Interface Sci.* 51 (1):23–31. doi:10.1016/0021-9797(75)90078-8.

McMurry, P.H. and Grosjean, D. (1985). Gas and Aerosol Wall Losses in Teflon Film Smog Chambers. *Environ. Sci. Technol.* 19 (12):1176–1182. doi:10.1021/es00142a006.

McMurry, P.H. and Rader, D.J. (1985). Aerosol wall losses in electrically charged chambers. *Aerosol Sci. Technol.* 4 (3):249–268. doi:10.1080/02786828508959054.

Nah, T., McVay, R.C., Pierce, J.R., Seinfeld, J.H., and Ng, N.L. (2017). Constraining uncertainties in particle-wall deposition correction during SOA formation in chamber experiments. *Atmos. Chem. Phys.* 17 (3):2297–2310. doi:10.5194/acp-17-2297-2017.

Nakao, S., Shrivastava, M., Nguyen, A., Jung, H., and Cocker, D. (2011). Interpretation of secondary organic aerosol formation from diesel exhaust photooxidation in an environmental chamber. *Aerosol Sci. Technol.* 45 (8):964–972. doi:10.1080/02786826.2011.573510.

Nguyen T. B., Bates K. H., Buenconsejo R., Charan S., Cavanna E. E., Cocker D. R., Day D., DeVault M., Donahue N. H., Finewax Z., Habib L., Handschy A., Hildebrandt Ruiz L., Hou C., Jimenez J., Joo T., Klodt A., Kong W., Le C., Masoud G. G., Mayernik M., Ng N. L., Nienhouse E., Nizkorodov S. A., Orlando J. J., Post J. J., Sturm, O., Thrasher B., Tyndall G. S., Seinfeld J.

H., Worley S., Zhang X. and Ziemann P.: Overview of ICARUS – A Curated, Open Access, Online Repository for Atmospheric Simulation Chamber Data (In review process with ACS Earth and Space Chemistry, expected to be published in 2023)

Odum, J.R., Hoffmann, T., Bowman, F., Collins, D., Flagan, R.C., and Seinfeld, J.H. (1996). Gas/particle partitioning and secondary organic aerosol yields. *Environ. Sci. Technol.* doi:10.1021/es950943+.

Odum, J.R., Jungkamp, T.P.W., Griffin, R.J., Forstner, H.J.L., Flagan, R.C., and Seinfeld, J.H. (1997). Aromatics, reformulated gasoline, and atmospheric organic aerosol formation. *Environ. Sci. Technol.* 31 (7):1890–1897. doi:10.1021/es960535l.

Pickering and Owen (1997). An Introduction to Global Environmental Issues. doi:10.43249780203974001.

Pierce, J.R., Engelhart, G.J., Hildebrandt, L., Weitkamp, E.A., Pathak, R.K., Donahue, N.M., Robinson, A.L., Adams, P.J., and Pandis, S.N. (2008). Constraining particle evolution from wall losses, coagulation, and condensation-evaporation in smog-chamber experiments: Optimal estimation based on size distribution measurements. *Aerosol Sci. Technol.* 42 (12):1001–1015. doi:10.1080/02786820802389251.

Rothfuss, N.E. and Petters, M.D. (2016). Coalescence-based assessment of aerosol phase state using dimers prepared through a dual-differential mobility analyzer technique. *Aerosol Sci. Technol.* 50 (12):1294–1305. doi:10.1080/02786826.2016.1221050.

Saucy, D.A., Kamens, R.M., and Linton, R.W. (1983). AN AEROSOL INJECTION AND OUTDOOR CHAMBER GAS- PARTICLE REACTIONS. 17 (12):2617–2624.

Seinfeld, J. H., Pandis, S. N. (2016). Atmospheric chemistry and physics: from air pollution to climate change, 3rd ed.; *John Wiley & Sons:* Hoboken.

Shao, Y., Wang, Y., Du, M., Voliotis, A., Alfarra, M.R., Omeara, S.P., Turner, S.F., and McFiggans, G. (2022). Characterisation of the Manchester Aerosol Chamber facility. *Atmos. Meas. Tech.* 15 (2):539–559. doi:10.5194/amt-15-539-2022.

Simones, M.P., Gutti, V.R., Meyer, R.M., and Loyalka, S.K. (2011). Measurements of aerosol charge and size distribution for graphite, gold, palladium,and silver nanoparticles. *Nucl. Technol.* 176 (2):211–226. doi:10.13182/NT10-10.

Stolzenburg, D., Wang, M., Schervish, M., and Donahue, N.M. (2022). Tutorial: Dynamic organic growth modeling with a volatility basis set. *J. Aerosol Sci.* 166 (August):106063. doi:10.1016/j.jaerosci.2022.106063.

Sunol, A.M., Charan, S.M., and Seinfeld, J.H. (2018). Computational simulation of the dynamics of secondary organic aerosol formation in an environmental chamber. *Aerosol Sci. Technol.* 52 (4):470–482. doi:10.1080/02786826.2018.1427209.

Trump, E.R., Epstein, S.A., Riipinen, I., and Donahue, N.M. (2016). Wall effects in smog chamber experiments: A model study. *Aerosol Sci. Technol.* 50 (11):1180–1200. doi:10.1080/02786826.2016.1232858.

Van Dingenen, R., Raes, F., and Vanmarcke, H. (1989). Molecule and aerosol particle wall losses in SMOG chambers made of glass. *J. Aerosol Sci.* 20 (1):113–122. doi:10.1016/0021-8502(89)90035-9.

Vansevenant, B., Louis, C., Ferronato, C., Fine, L., Tassel, P., Perret, P., Kostenidou, E., Temime-Roussel, B., D'Anna, B., Sartelet, K., Cerezo, V., and Liu, Y. (2021). Evolution under dark conditions of particles from old and modern diesel vehicles in a new environmental chamber characterized with fresh exhaust emissions. *Atmos. Meas. Tech.* 14 (12):7627–7655. doi:10.5194/amt-14-7627-2021.

Volkamer, R., Jimenez, J.L., San Martini, F., Dzepina, K., Zhang, Q., Salcedo, D., Molina, L.T., Worsnop, D.R., and Molina, M.J. (2006). Secondary organic aerosol formation from anthropogenic air pollution: Rapid and higher than expected. *Geophys. Res. Lett.* 33 (17):3–6. doi:10.1029/2006GL026899.

Wagner, R., Yan, C., Lehtipalo, K., Duplissy, J., Nieminen, T., Kangasluoma, J., Bauer, P.S., Bergen, A., Bernhammer, A., Bianchi, F., and Brilke, S. (2017). The role of ions in new particle formation in the CLOUD chamber. (December):15181–15197.

Wang, N., Jorga, S.D., Pierce, J.R., Donahue, N.M., and Pandis, S.N. (2018). Particle wall-loss correction methods in smog chamber experiments. *Atmos. Meas. Tech.* 11 (12):6577–6588. doi:10.5194/amt-11-6577-2018.

Wiedensohler, A. (1988). An approximation of the bipolar charge distribution for particles in the submicron size range. *J. Aerosol Sci.* 19 (1):387–389. doi:10.1016/0021-8502(88)90278-9.Xu, N. and Collins, D.R. (2021). Design and characterization of a new oxidation flow reactor for laboratory and long-term ambient studies. *Atmos. Meas. Tech.* 14 (4):2891–2906. doi:10.5194/amt-14-2891-2021.

Xu, N., Le, C., Cocker, D.R., and Collins, D.R. (2022). An oxidation flow reactor for simulating and accelerating secondary aerosol formation in aerosol liquid water and cloud droplets. (November):1–41.

Yu, J., Cocker III, D.R., Griffin, R.J., Flagan, R.C., and Seinfeld, J.H. (1999). Journal of Atmospheric Chemistry, Volume 34, Number 2 - SpringerLink. *J. Atmos. Chem.* 34 (2):207–258.

Zelenyuk, A., Cai, Y., and Imre, D. (2006). From Agglomerates of Spheres to Irregularly Shaped Particles: Determination of Dynamic Shape Factors from Measurements of Mobility and Vacuum Aerodynamic Diameters. *Aerosol Sci. Technol.* 40 (3):197–217. doi:10.1080/02786820500529406.

Zhang, Q., Jimenez, J.L., Canagaratna, M.R., Allan, J.D., Coe, H., Ulbrich, I., Alfarra, M.R., Takami, A., Middlebrook, A.M., Sun, Y.L., Dzepina, K., Dunlea, E., Docherty, K., DeCarlo, P.F., Salcedo, D., Onasch, T., Jayne, J.T., Miyoshi, T., Shimono, A., Hatakeyama, S., Takegawa, N., Kondo, Y., Schneider, J., Drewnick, F., Borrmann, S., Weimer, S., Demerjian, K., Williams, P., Bower, K., Bahreini, R., Cottrell, L., Griffin, R.J., Rautiainen, J., Sun, J.Y., Zhang, Y.M., and Worsnop, D.R. (2007). Ubiquity and dominance of oxygenated species in organic aerosols in anthropogenically-influenced Northern Hemisphere midlatitudes. *Geophys. Res. Lett.* 34 (13):1–6. doi:10.1029/2007GL029979.

Zhao, Z., Le, C., Xu, Q., Peng, W., Jiang, H., Lin, Y.H., Cocker, D.R., and Zhang, H. (2019). Compositional Evolution of Secondary Organic Aerosol as Temperature and Relative Humidity Cycle in Atmospherically Relevant Ranges. *ACS Earth Sp. Chem.* 3 (11):2549–2558. doi:10.1021/acsearthspacechem.9b00232.

Appendix

I led the major update of the central control, data acquisition and instrument control programs based on Windows 10, LabVIEW 19 or later versions for the major environmental chamber facility.

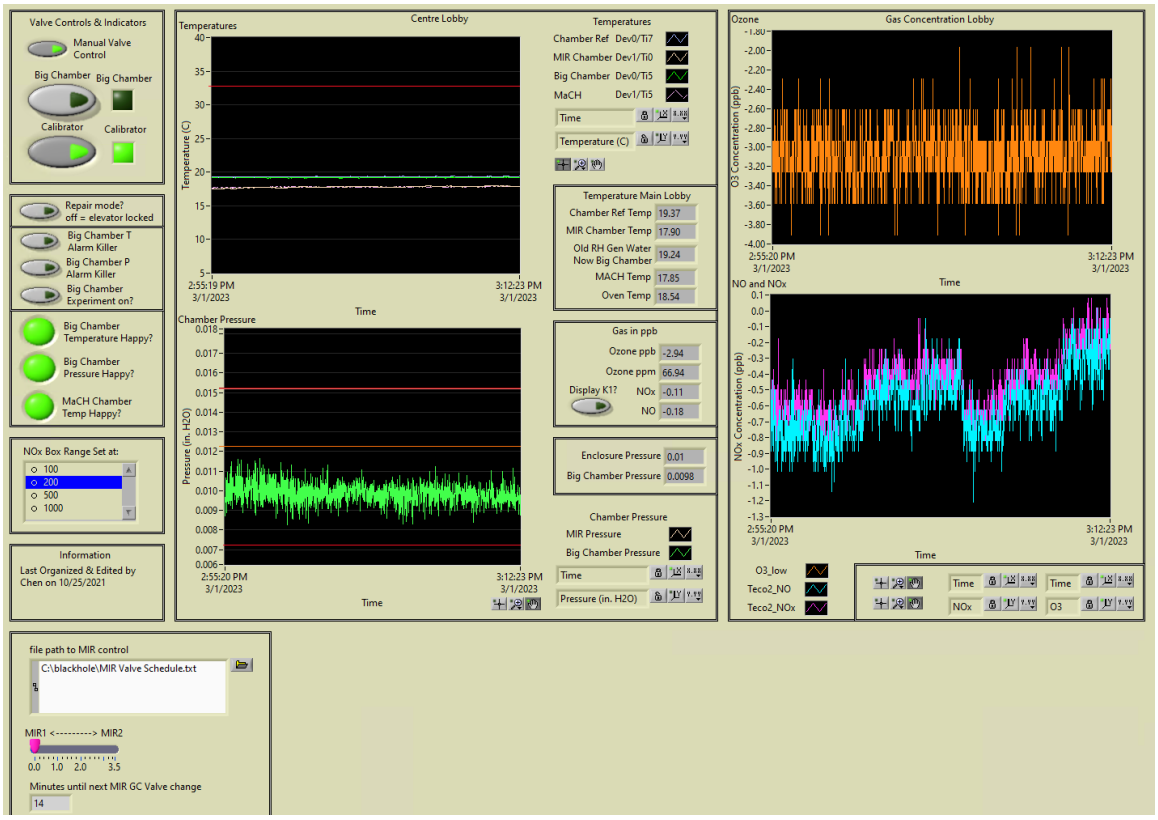

Figure 7-1. Updated layout of the central chamber enclosure control and data acquisition program (the "Blackhole" program) for the major chamber facility with LabVIEW 19.

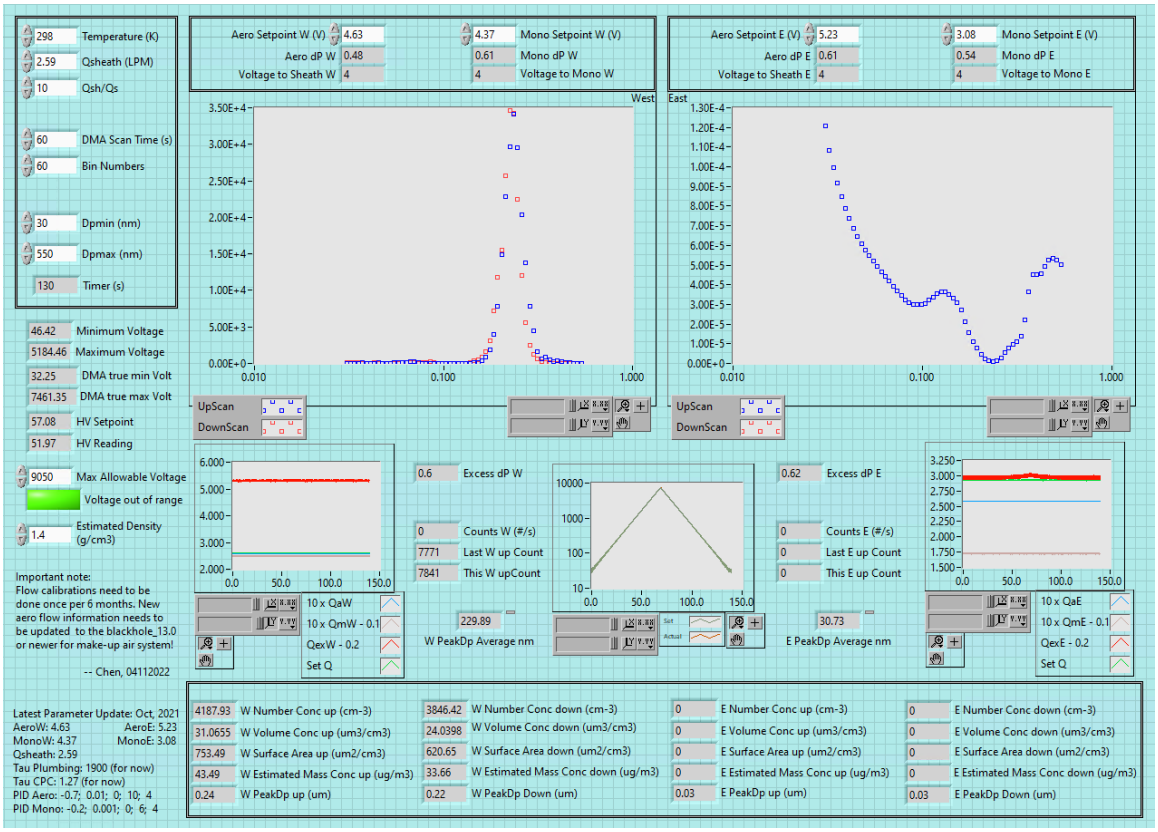

Figure 7-2. Updated layout of the dual scanning mobility particle sizer (Dual-SMPS) instrument control and data acquisition program for the major chamber facility with LabVIEW 19.

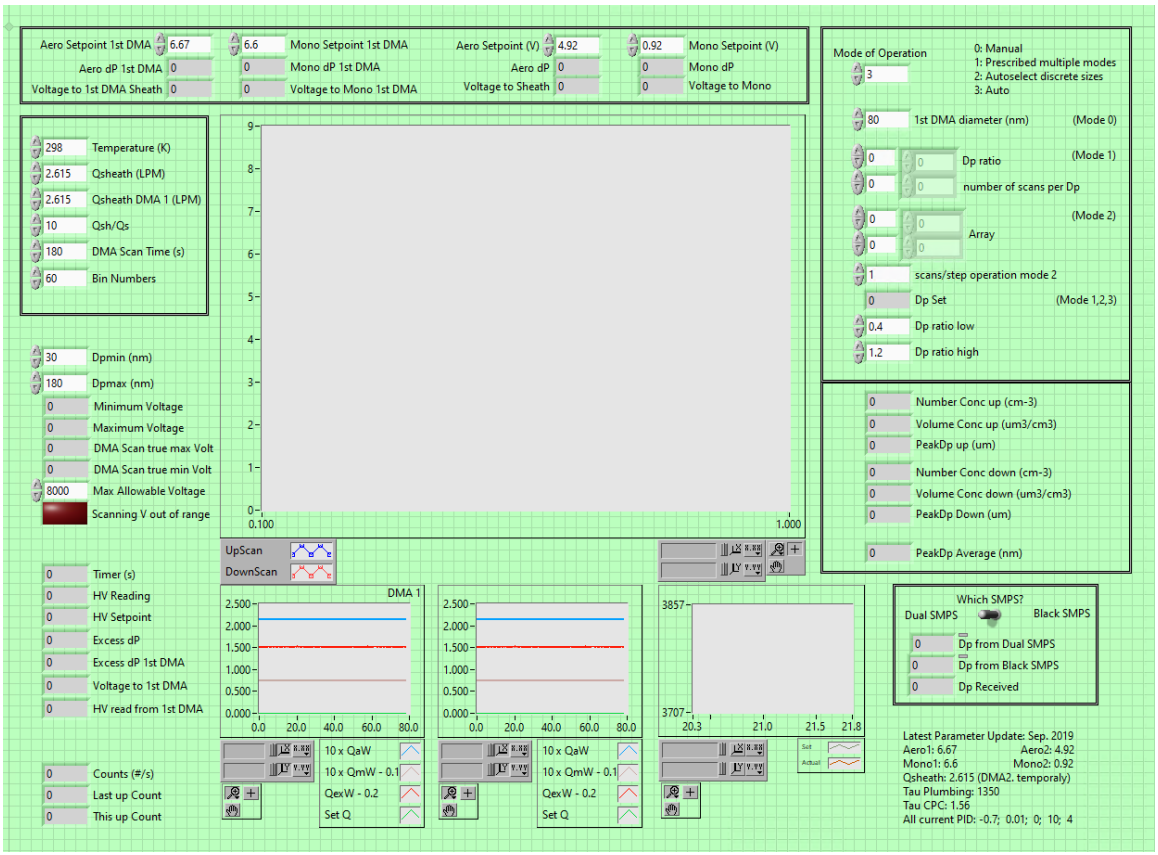

Figure 7-3. Updated layout of the volatility tandem differential mobility analyzer (VTDMA) instrument control and data acquisition program for the major chamber facility with LabVIEW 19.

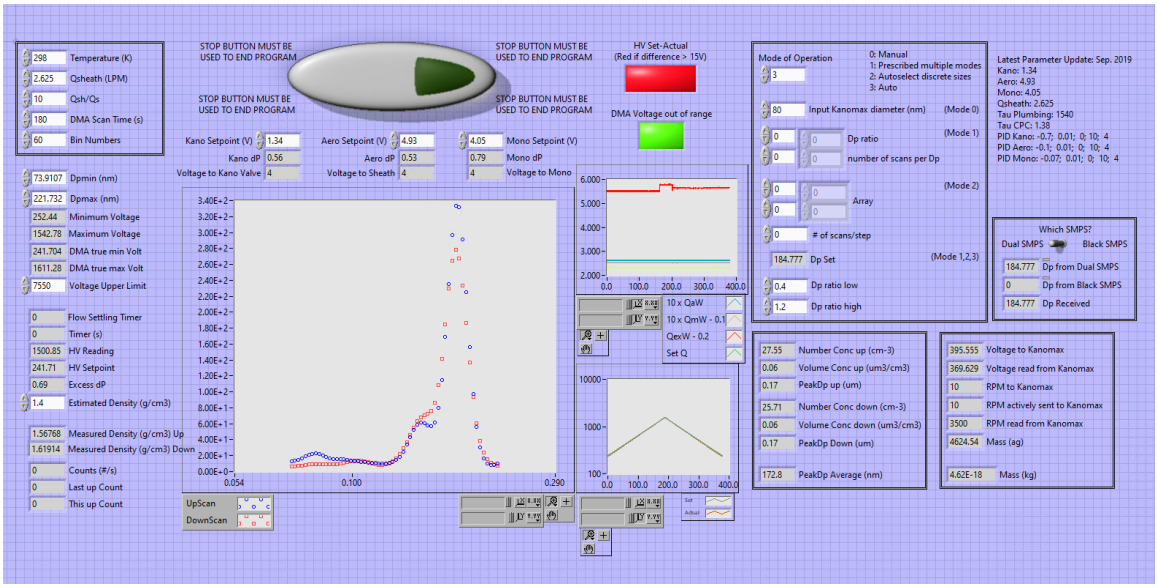

Figure 7-4. Updated layout of the Kanomax aerosol particle mass analyzer (APM-SMPS) instrument control and data acquisition program for the major chamber facility with LabVIEW 19.

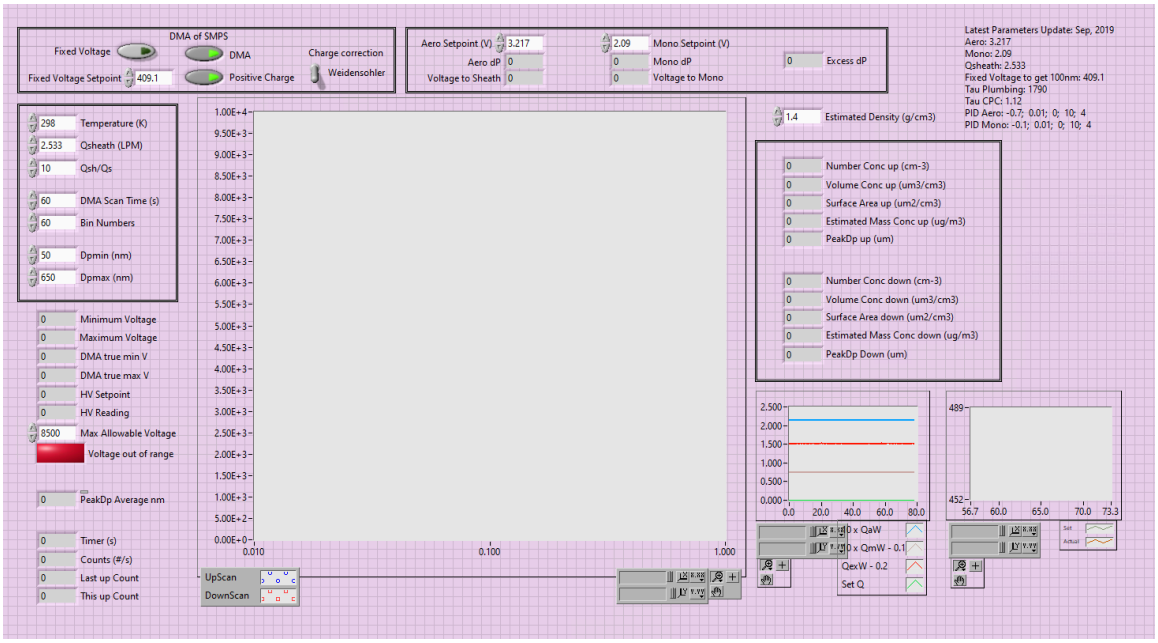

Figure 7-5. Updated layout of the alternative scanning mobility particle sizer (Black SMPS) instrument control and data acquisition program for the major chamber facility with LabVIEW 19.

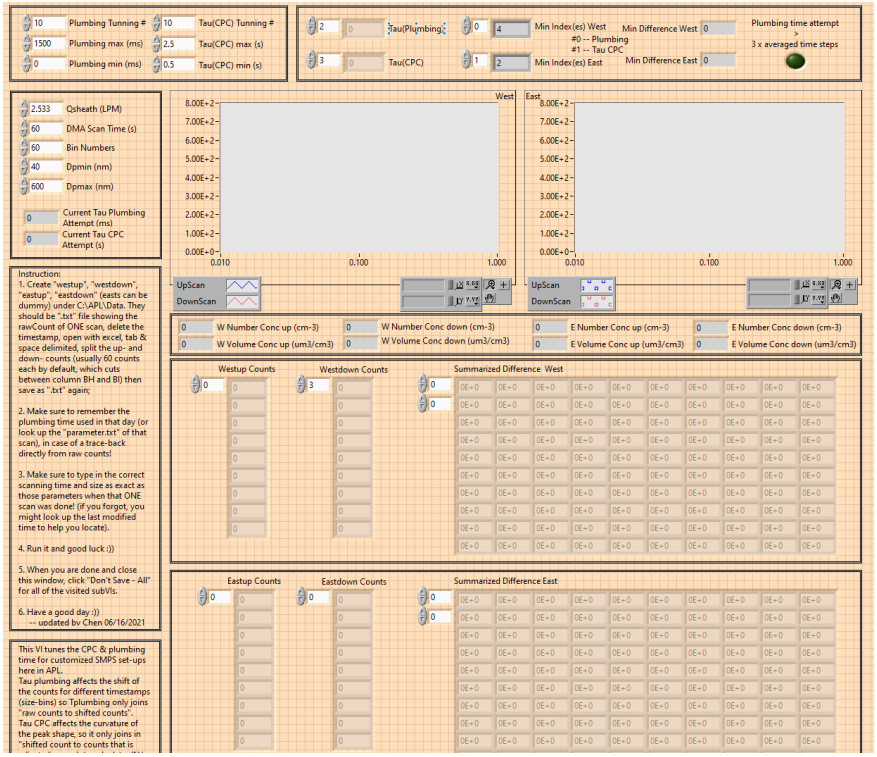

Figure 7-6. Layout of the SMPS up- / down-scan parameter tuning program for custom SMPS programs with LabVIEW 20.